High-throughput exploration of multinary perovskite compositions for solar cell applications

by

Shahram Moradi

B.Sc., Islamic Azad University, Urmia branch, IRAN, 2005

M.Sc., Middle East Technical University, Ankara, TURKEY, 2017

A Dissertation Submitted in Partial Fulfillment of the

Requirements for the Degree of

DOCTOR OF PHILOSOPHY

In the Department of Electrical and Computer Engineering

University of Victoria

Supervisory Committee

Dr. Makhsud I. Saidaminov, Supervisor

(Department of Electrical and Computer Engineering)

Dr. Jens Bornemann, Departmental Member

(Department of Electrical and Computer Engineering)

Dr. Alexandre Brolo, Outside Member

(Department of Chemistry)

Abstract

A photovoltaic (PV) device or a solar cell converts sunlight directly to electricity. Mechanistically, a solar cell is a sandwich of multiple material layers. The interaction of photons with the absorber layer in the middle of the sandwich leads to the creation of excited electrons; a neighboring layer then extracts these electrons, and this unidirectional transport of electrons is by definition an electrical current.

Silicon is the most commonly used material in commercial solar cells. But thin film solar cells generally cost less and are easier to manufacture than silicon. Thin film solar cells are made by coating a thin layer of a highly light-absorptive semiconductor material on a substrate. Typically, the appearance of thin film layer semiconductor is dark which enables absorption of most of the visible spectrum. Recent advancements in PV technologies have greatly improved their light-to-electricity conversion efficiency and led to new solar materials that can be competitive alternatives to commercialized silicon technologies.

One such promising material is halide perovskite. Perovskite solar cells (PSCs) can be printed, coated, or vacuum-deposited on a substrate. They are typically easy to fabricate and reach power conversion efficiencies (PCE) of higher than 20%. In the short period, PSCs have demonstrated a fast growth of PCE from 3% in 2009 to over 25% in 2019. However, to be commercially feasible, PSCs have to become stable and durable enough to operate for at least 20 years under outdoor conditions (ISOS protocol)[1–6]. Therefore, the research community is focusing on the stability, as well as scalability of PSCs.

Strategies for the fabrication of thin films are constantly developed and have significantly benefited from the advent of high-throughput synthesis (HTS) and exploration methods. HTS methods allow systematic preparation of combinatorial composition libraries to discover targeted properties and functional materials. The HTS strategy provides a platform to combine various ratios of materials by preparing a massive number of samples and screening optoelectronic properties of the prepared library to find the optimized combinatorial ratios of multinary compositions. The goal of this dissertation is to develop HTS methods for optimizing multinary compositions for PSCs.

The dissertation introduces two high-throughput methods on how to optimize perovskite materials for perovskite solar cell applications with a compositionally-graded film (CGF) platform.

The first method elaborates on the synthesis and characterization of binary halides $MAPb(I_xBr_{1-x})_3$ on a CGF with over 200 compositions getting synthesized in less than one minute and characterized with a robotized spectrometer. The second method develops for the optimization of triple cations on ternary CGF we call it t-CGF for investigating the most stable perovskite $Cs_xMA_yFA_zPbI_3$. We utilized the reported results for fabricating PSCs with high durability and capable of being scaled up for commercialized.

The dissertation consists of 6 chapters:

Chapter 1 will introduce the fundamentals (structure and optoelectronic properties) of the perovskite material. In addition, the objectives of the dissertation will be discussed at the end of this chapter.

Chapter 2 will review the strategies for synthesizing and depositing thin films that are essential for PSCs. We elaborate on most existing HTS methods for different applications including solar cells, light-emitting diodes, batteries, thermoelectrics, and superconductors.

Chapter 3 will focus on experimental methods of preparation and characterization of perovskite thin films used in this dissertation.

Chapter 4 will discuss our HTS of binary alloys. It is based on compositionally-graded films (CGF) for optimizing binary compositions. As a showcase example, we focus on binary perovskite HTS. We will also show how a spectrometer and a robotic arm could facilitate the high-throughput characterization of synthesized materials.

Chapter 5 will discuss our HTS of ternary alloys. It is based on triple compositionally-gradient films (t-CGFs) for optimizing ternary compositions. We apply our t-CGF strategy to discover a range of stable ternary perovskites. We then use them to make PSCs and reveal three degradation mechanisms in devices under operation as a function of composition.

Chapter 6 provides outlook for the use of these methods toward the improvement of the functional materials for applications beyond solar. We also discuss how PSCs can be shaped by the HTS methods toward commercialization.

Contents

List of abbreviations

HTS	high-throughput synthesis
HTE	high-throughput experimentation
CGF	compositionally-graded film
t-CGF	ternary compositionally-graded film
MA	Methylammonium
FA	Formamidinium
Cs	Cesium
DMF	dimethylformamide
DMSO	dimethyl sulfoxide
V_{OC}	open-circuit voltage
J_{SC}	short-circuit current
FF	fill factor
PCE	power conversion efficiency
EQE	External Quantum Efficiency
ITO	indium-doped tin oxide
PCS	perovskite solar cell
pXRD	powder X-ray diffraction
SEM	scanning electron microscopy
NMR	nuclear magnetic resonance
EDX	energy dispersive X-ray
RH	relative humidity
eV	electron volt
1D	one dimensional
2D	two dimensional

List of symbols

a	lattice constant
r	ionic radius of atoms
$S(\lambda)$	maximum variance of absorbance as a function of wavelength
σ	standard deviation
Δ	delta
°C	degree Celsius
t	tolerance factor
t_{eff}	effective tolerance factor
A	absorbance
T	temperature
K	Boltzmann constant
V	voltage
E_g	bandgap energy
E_u	Urbach energy
η	efficiency
$\hbar$	Plank's constant
c	speed of light
λ	wavelength
M	molar
μ	micro or 10^{-6}
nm	nanometer (10^{-9} m)
$\dot{A}$	angstrom

List of Figures

Main Figures

Supplementary Figures

List of tables

Acknowledgment

I acknowledge my academic advisor Dr. Makhsud I. Saidaminov for his great supervision in guiding and supporting me throughout this research, as well as Dr. Jens Bornemann, and Dr. Alexandre Brolo for their mentorship and academic support.

My appreciation also goes to my lab mates Dr. Soumya Kundu, Dr. Yuki Haruta, Muhammad Awais Malik, and other team members in Dr. Saidaminov's lab whose efforts contributed so thoroughly through their further comments, and CAMTEC members Stanislav Konorov, Alex Wlasenko, Mike Pfleger, and Andrew Macdonald for training on the instruments. I also thank the members of Solaires Inc. for all their support and feedback in our biweekly meetings.

I also thank and Dr. Alexander R. UhI for participating in my defense as an external examiner.

Finally, my special thanks go to my family members whose support allowed my studies to go the extra mile.

Chapter 1. Introduction

1-1. Abstract

Among various semiconductors for solar cell applications, perovskites as a new class of semiconductors have demonstrated unique optoelectronic properties. Low cost-fabrication, direct bandgap nature, broad bandgap tunability, high mobility of both electrons and holes, and long diffusion lengths make perovskite materials highly competitive with other semiconductors that either lack the given critical properties all at once or not comparable quantitatively with the perovskites' characteristics. Perovskite solar cells are not commercialized yet since durability and scalability are two main concerns that need compositional optimization. This dissertation aims to introduce methods for accelerating optimization to address issues with the durability and stability of perovskite materials. In this chapter, we aim to familiarize the reader with the fundamentals of perovskites.

1-2. Introduction

Efficient solar cell devices offer one of the promising solutions to reduce carbon dioxide emissions. However, harnessing sunlight to generate electricity requires a cost-efficient technology. Figure 1-1 demonstrates a chart of the best certified solar cell efficiencies since 1976[7]. Among all emerging photovoltaic architectures, perovskite solar cells (PSCs) surpass many other solar cell technologies including CdTe and CIGS, and now compete with broadly-commercialized Si technology. PSCs have first demonstrated an efficiency of 3.8% in 2009, and this value has now reached 25.7%. The main reason for receiving wide attention in this research field is the low-cost and environmentally friendly alternative compared to other solar cell technologies. Furthermore, their tunable optoelectronic properties provide a promising future for the integration of PSCs with other ones to create tandem solar cells, the most famous being in tandem with silicon technology that reached a reported efficiency of over 30%[8].

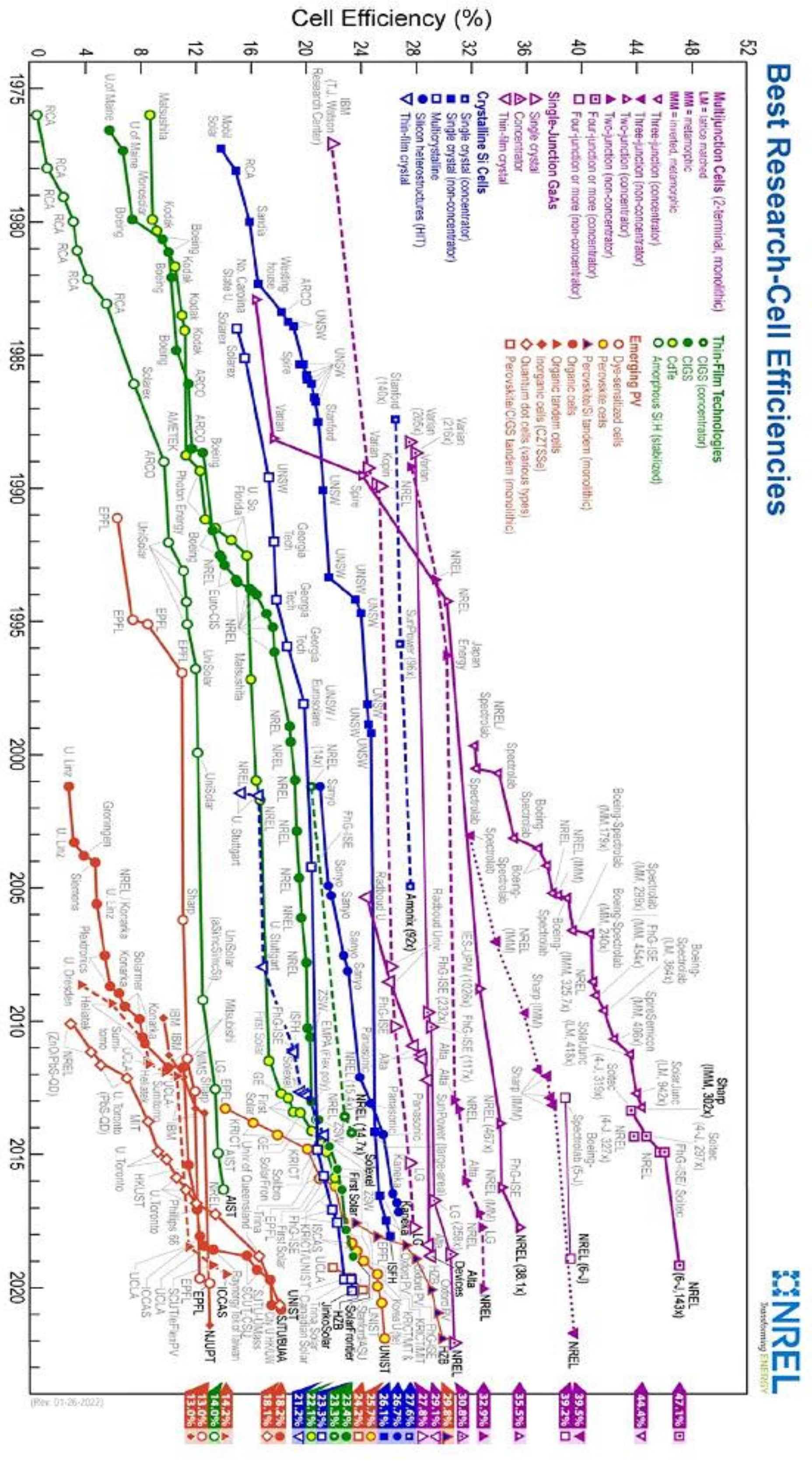

Figure 1- 1 The best research solar cell efficiencies from 1976 to 2022[7].

Figure 1-2a shows the architecture of a typical PSC made of 5 layers on a glass substrate that is stacked with electron-transport-layer (ETL), perovskite layer as an absorber, hole-transport-layer (HTL), and gold contacts. By choosing materials with different band alignments, one can extract photogenerated electrons through one side and holes through the opposite side (Figure 1-2b); this leads to an electrical current, and the difference in the energy of electrons and holes generates an electrical voltage (i.e., electrical energy).

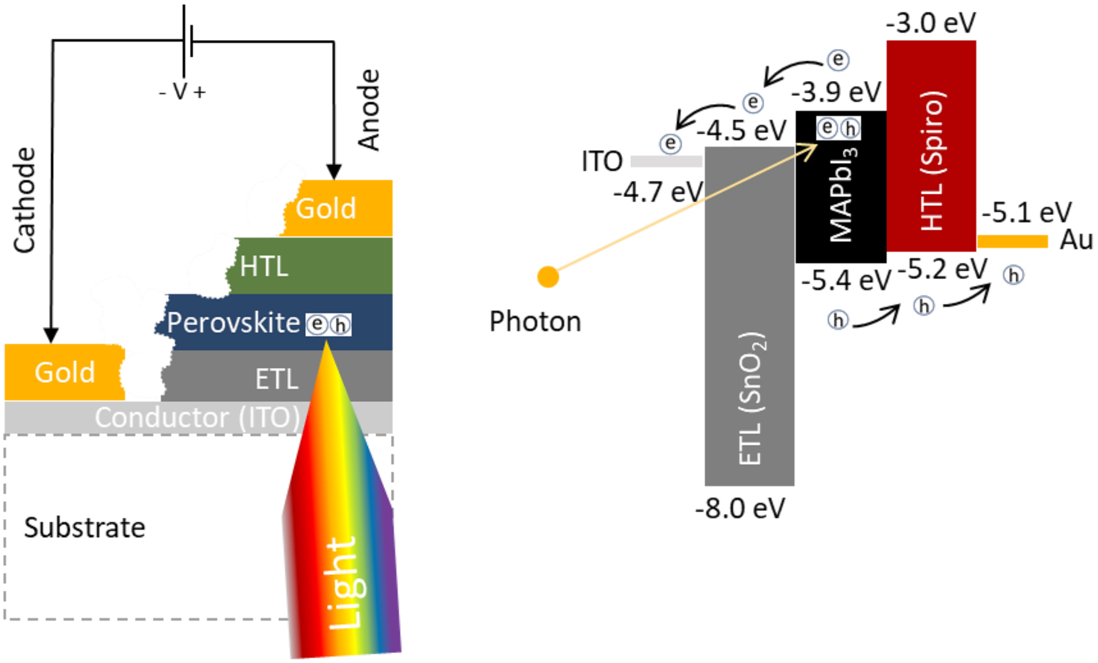

Figure 1- 2. A PSC is made of **a,** five layers on top of the substrate including ETL, perovskite layer as an absorber, HTL, and contacts to exploit generated electron-hole pairs after separation. **b,** Energy levels utilized five layers that direct separated electrons and holes toward the gold contacts by bending the top or bottom of energy band levels.

1-3. Perovskite structure

Now we will introduce the crystal structure of perovskites. A perovskite is any material with a crystal structure shown in Figure 1-3 following the formula ABX_3, which was first discovered as the mineral called perovskite consisting of calcium titanium oxide ($CaTiO_3$). The letters in the given perovskite formula represent different ions: A and B are both cations, while X is an anion. In particular, a halide perovskite contains a monovalent organic and/or inorganic cation, B is a divalent metal cation, and X is a halogen. The overall oxidation state of perovskite is neutral and the geometric constraints limit the choices of suitable cations to form a stable composition with a cubic crystal structure. The methylammonium (MA) lead iodide with the formulation of $MAPbI_3$ is stable at room temperature but there are an enormous number of adopted perovskite compositions[9] that facilitate various optoelectronic properties. For example, methylammonium (MA) and formamidinium (FA) as organic cations and cesium (Cs) as an inorganic cation can be mixed in the A site, or metals (Pb, Sn, etc) in the B site, with an unlimited combinatorial ratio of halogens (I, Br, or Cl) in X site.

Figure 1-3b shows a cubic perovskite structure of ABX_3 composition, the lattice parameter can be extracted from two Miller planes: from the (200) plane in which case the unit cell (a_1) is comprised of two radii of B and X; and from the (100) plane in which case the unit cell (a_2) is comprised of cathetus of the right-angle triangle whose hypotenuse is comprised of two radii of A and X. The ratio of one to another, called Goldschmidt tolerance factor (t), ($t = a_2/a_1 = \frac{r_A+r_X}{\sqrt{2}(r_B+r_X)}$) has to be between 0.8 to 1 to form a stable perovskite. The tolerance factor defines if the different ions fit in the overall cubic crystal structure of the perovskite.

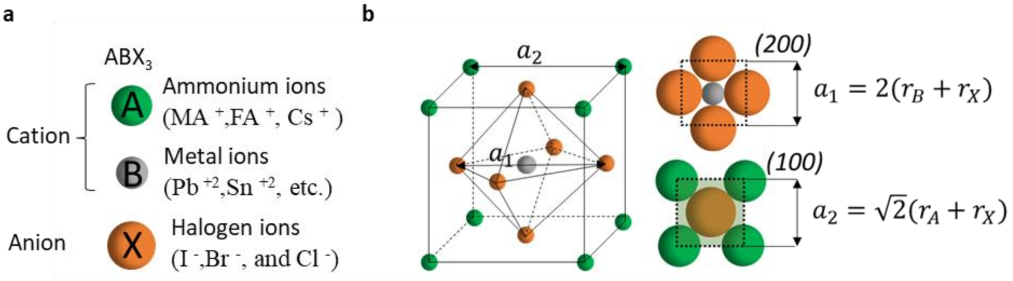

Figure 1- 3. Halide perovskite composition and its structure.

1-4. Optoelectronic properties of perovskite

Halide perovskite materials are a new class of semiconductors with a unique blend of properties such as:

1. Low cost and capability of fabricating with simple methods at low temperatures.
2. They possess direct bandgap and broad absorption spectra with an absorption coefficient of up to 10^5 cm^{-1} that makes perovskite materials an efficient solar material. The advantage of direct bandgap vs. indirect semiconductors such as silicon is that the perovskite material can absorb sufficient photons while being 400 times thinner than silicon[10].
3. The tunability of bandgap energy can be achieved by modifying the metal or halide sites in the perovskite composition. The combination of several compositions in one site also tunes the bandgap that is in huge demand for constructing efficient perovskite-perovskite tandem PSCs[11].

4. Perovskite as an intrinsic semiconductor exhibit high mobility for both holes (~585 $cm^2V^{-1}s^{-1}$ hole mobility of $CsSnI_3$ [12]) and electrons (e.g., electron mobility is even higher than hole due to the low effective mass of electrons).
5. The diffusion length of generated charge carriers is considerably long[13] (>175μm[14]).

All the above-mentioned optoelectronic properties distinguish perovskite materials from many of other materials that possess only some of the properties that are essential in boosting the efficiency and performance of solar cell devices.

1-5. Objectives

The power conversion efficiency of halide perovskites show a promising potential to be considered as an alternative to other existing solar technologies. However, a significant technological challenge must be addressed first. PSCs suffer from compositional instability that reduces the lifetime, and challengesscaling-up cells. This dissertation first reviews reported strategies on multinary compositional optimization for different applications. It then offers two novel strategies for the rapid optimization of binary and ternary compositions, using perovskite as a study case material. We will identify a range of stable perovskites that we will then use to make stable and efficient solar cells.

Chapter 2. A perspective on high-throughput synthesis of thin films for the discovery of energy materials

Note: This chapter is published and I as the first author contributed to research on relative literature reviews and writing the perspective.

2-1. Abstract

Thin films are an integral part of many electronic and optoelectronic devices. They also provide an excellent platform for material characterization. Therefore, strategies for making thin films are constantly developed and have significantly benefited from the advent of high-throughput synthesis (HTS) techniques. This chapter provides a summary of recent advances in HTS of thin films from an experimentalist’s point of view. The work analyzes strategies of HTS and then in detail discusses their use in applications that rely on thin films, such as solar cells, batteries, superconductors, and thermoelectrics. This chapteralso summarizes some key challenges and opportunities in the HTS of thin films.

2-2. Introduction

The pace of development of new technologies is often dependent on the advent of new functional materials. To accelerate the exploration of new materials, high-throughput synthesis (HTS) techniques are being developed to discover new compositions or to optimize known ones[15–20]. Figure 2-1a depicts the main stages of high-throughput material discovery in a closed-loop manner: high-throughput synthesis[21], high-throughput data-mining (i.e., characterization[22]), and data analysis[18,23–29].

High-throughput synthesis, a key focus of this chapter, is arguably the most important step[21,22,30–32] and is essential for creating a high-quality dataset. Variations of HTS have been used for a long time in the solid-state peptide synthesis [33], co-deposition[34–36] of ternary-alloys such as Fe-Cr-Ni [37], as well as drug discovery[38–40] and pharmaceutics[41].

Among HTS techniques, microfluidics, split & pool, and micro-pipetting have been dominant platforms (Figure 2-1b). The other common HTS platform is based on thin films created by various deposition methods such as sputtering, evaporating, and spraying. Though less explored (Figure

2-1b), the HTS of thin films offers some unique opportunities. First, material characterization techniques are usually well-suited to apply for thin films. Second, many devices rely on the development of thin films. For example, typical thin-film solar cells are made of at least five thin films, including two electrodes, a light-absorber semiconductor, and two charge-carrier-selective materials [42].

This chapter discusses recent advances in the HTS of thin films. We first briefly summarize major HTS techniques and then focus in detail on the HTS of thin films. We will then discuss the HTS of thin films used to explore materials for energy-related applications, such as solar cells, batteries, thermoelectric, and superconductors. To the best of our knowledge, there are only a few review and perspective papers on HTS of thin films with a focus on the physical vapor deposition of metals[43] or organic solar cell materials[15]. This chapter instead emphasizes HTS of thin films by solution-processed techniques for a broader family of energy-related materials. It is worth noting that this chapter does not intend to cover all known thin-film HTS methods, but it rather focuses on recent and illustrative approaches and emphasizes the importance of thin-film platforms in the discovery of new materials.

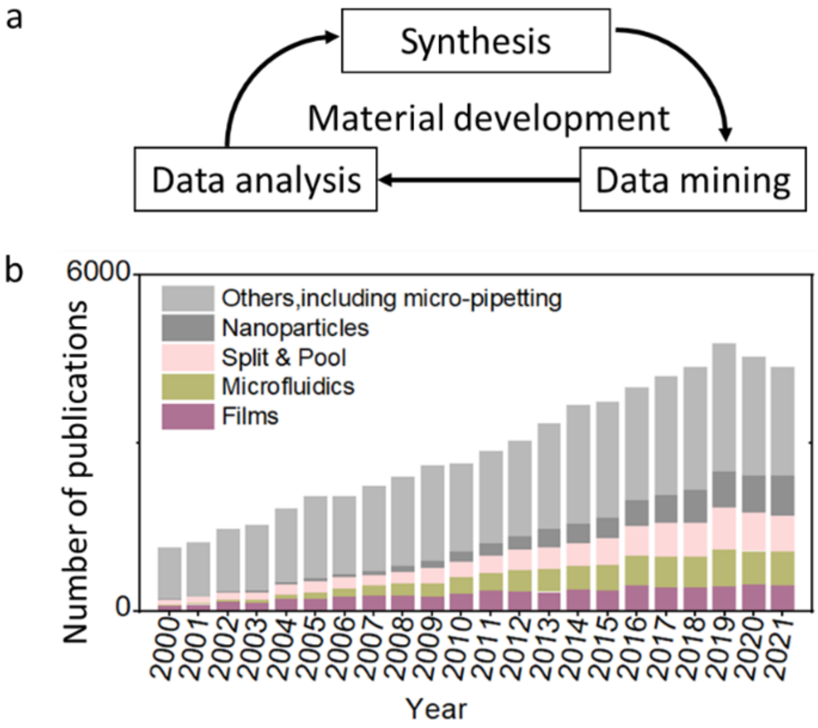

Figure 2- 1. High-throughput discovery of materials. **a,** Three-step closed-loop optimization and discovery of materials. **b,** Number of publications on HTS platforms extracted from the Web of Science using the keywords of “throughput or combinatorial “, and synthetic techniques, such as “fluidic or microfluidic”, “split or pool”, nanoparticles”, and “films”. A decrease in the number of publications in 2020 and 2021 is likely due COVID-19 pandemic.

2-3. High-throughput synthesis

Figure 2-2 illustrates common platforms of HTS of materials. We will now briefly discuss each of these methods and then focus on the HTS of thin films.

Figure 2-2a shows the micro-pipetting platform that allows dispensing of liquids in a high-throughput manner. The platform is widely used in the crystallization of proteins[44–48]. This method was recently used to synthesize halide perovskites, a promising emerging family of materials for optoelectronic applications. The outcomes were characterized by convolutional neural network-based image recognition, which led to the first synthesis of $(3\text{-PLA})_2PbCl_4$ with strong blue photoluminescence[48].

Figure 2-2b displays the split and pool synthesis, in which two or more compounds are first mixed to prepare a pool and then divided into several segments. Each of these segments is then mixed again with new building blocks. The stepwise iteration in the split and pool approach allows making a large number of samples, in geometrical progression [49–51]. The split and pool HTS is widely used in the high-throughput synthesis and analysis of proteins and RNAs[52].

Figure 2-2c demonstrates a microfluidic platform[53–56] that allows containing and controlling of fluids in micrometer dimensions in a spatiotemporal manner[57]. The controlled co-flowing through the microfluidic channels leads to interfaces or mixed solutions where chemical reactions may occur[58,59]. Microfluidic-based HTS is widely used in the synthesis of nanoparticles and drug discovery and development.[60] A microfluidic platform was recently used to study the nucleation mechanism of cesium lead halide perovskite nanocrystals, suggesting similarities with multinary metal chalcogenide systems, but with much faster reaction kinetics[57]. The microfluidic platform can be also applied to build asymmetric bilayers using naturally derived lipids that mimic mammalian cells, which then were used to quantify the effect that lipid asymmetry has on the permeability of doxorubicin, an anthracycline class of chemotherapy drugs.[61]

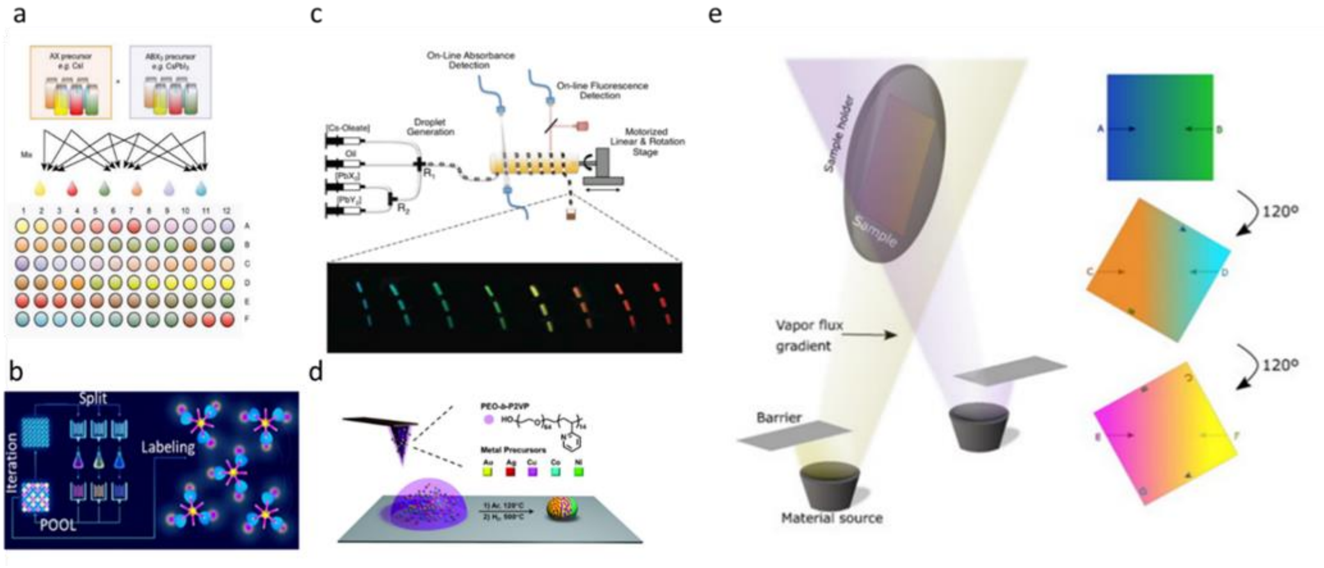

Figure 2- 2. Schematic of various HTS platforms. **a,** Micro-pipetting platform (Reprinted with permission from ref. [62]). **b,** Split & pool (Reprinted with permission from ref. [63]). **c,** Microfluidic platform (Reprinted with permission from ref. [57]). **d,** Scanning probe block copolymer lithography (Reprinted with permission from ref. [64]) **e,** Co-evaporation (Reprinted with permission from ref. [65]).

Figure 2-2d shows a dip-pen lithography approach to synthesize nanoparticles in a high-throughput manner[64]. This approach can deliver attoliter-scale volumes to the desired location where a reaction can occur. The method has been widely used for making bimetallic nanoparticles[66], and even a single trimetallic alloy nanoparticle[67]. It was also used for combinatorial synthesis of nanoparticles consisting of five different elements (Au, Ag, Cu, Co, and Ni): a polymer preloaded with the appropriate metal salts was deposited onto a substrate and then thermally annealed to create nanoparticles (Figure 2-2d).

Figure 2-2e shows one of the most common methods of creating a thin film library by physical-vapor deposition[68–70]. This technique combines multi-target material deposition with mask positioning to make compositionally-graded thin films[43]. The moving mask at different angles leads to the formation of gradient films on a substrate[65]. Rotation of substrate by 120° in each co-deposition process and controlling the speed of the mask for gradient formation of the layer lead to the formation of multinary thin-film alloys (Figure 2-2e). Thus, gradient thin films allow for exploring full composition and process parameter spaces (Figure 2-3, right panel)[71] and material interfaces and thicknesses[72].

Solution-processable methods are also used to make a library of materials based on thin-film platforms, among which spin-coating is the most common. Spin-coating implies depositing films from many solutions pre-made by discrete mixing of precursors, also termed fragmentary (or discontinuous) composition optimization (Figure 2-3, left panel). Since the fragmentary approach is discontinuous and hence misses intermediate compositions, computational tools are usually used to simulate the entire parameter space[73].

In contrast, continuous composition optimization can cover the entire parameter space (Figure 2-3, right panel). This can be realized in compositionally-graded films made by physical vapor deposition (Figure 2-2e) or solution-processed techniques such as slot-die coating (Figure 2-3, right panel). In the latter, two precursor inks are supplied into a slot-die reservoir, where the inks are mixed and deposited on a substrate as a thin film. Because the supply rate of one ink is increased over time, while the second one is decreased, this approach leads to the in-situ change of composition (Figure 2-3, right panel) and eventually compositionally-graded films. The use of this method in the optimization of organic and perovskite solar cell materials is discussed below[74],[73].

Although an objective comparison of all discussed HTS platforms is challenging, the following can be said (Table 3-1). Microfluidic and thin-film HTS platforms enable continuous composition optimization, but they are limited to multiple components. For optimizing multi-component compositions, nanoparticle and split and pool HTS platforms are best suited. Thin-film platform's ultimate products are thin films that lend themselves for device integration.

Table 3- 1. Characteristics of HTS platforms.

HTS platforms	**Composition continuity**	**Synthesizing methods**		**Number of components to be optimized**	**Solid-state device compatibility**
		Solution	Physical-vapor deposition		
Micro-pipetting	Fragmentary	Yes	---	High	No
Nanoparticles	Fragmentary	Yes	---	High	No
Split & pool	Fragmentary	Yes	---	High	No
Microfluidic	Fragmentary/ Continuous	Yes	---	Limited	No
Thin Films	Fragmentary/ Continuous	Yes	Yes	Limited	Yes

2-4. Applications of thin-film made by HTS

In this section, we will discuss the use of HTS of thin films in the development of novel materials for applications in energy capture (solar cells, thermoelectric), energy storage (batteries), and energy transport (superconductors).

2-4-1. Solar cells

Emerging solar cells suffer from either low performance or stability[75]. Since they are made of multiple layers of thin films and each film is usually made of complex multinary components, their composition and fabrication strategies are constantly explored to address the mentioned challenges.

The common approach for the high-throughput exploration of solar cell materials is fragmentary (or discontinuous) optimization of composition. Figure 2-3, left panel, and Figure 2-4a illustrate examples of fragmentary optimization in which different precursor ratios are used to make a library of organic and perovskite films, respectively,[76],[73] which then were used to study their performance and stability. In another work[77], a machine-learning algorithm was used to optimize over 100 processing variations in fabricating organic photovoltaic devices. The fragmentary approach was also adopted for inkjet printing of homogeneous compositions of $CsPb(Br_xI_{1-x})_3$[78]. Since the fragmentary approach is discontinuous and hence misses intermediate compositions, computational tools are usually used to simulate the entire parameter space [73].

In contrast, continuous composition optimization can cover all possible intermediate phases. This can be realized in compositionally-graded films in which the concentration of components gradually changes along with the film. For instance, a pulsed infrared semiconductor laser was adopted for thermal evaporation of perovskite precursor CH_3NH_3I/PbI_2 bilayer films where the thickness of each layer was controlled to achieve gradient composition (Figure 2-4b). A movable mask system was used to deposit combinatorial thin-film libraries[79]. The synthesized films were used to fabricate solar cells and study the dependence of photovoltaic efficiency on precursor stoichiometry and thickness. Similarly, other works used compositionally-graded thin films for the optimization of organic or hybrid photovoltaic materials[80],[46],[81],[82],[83].

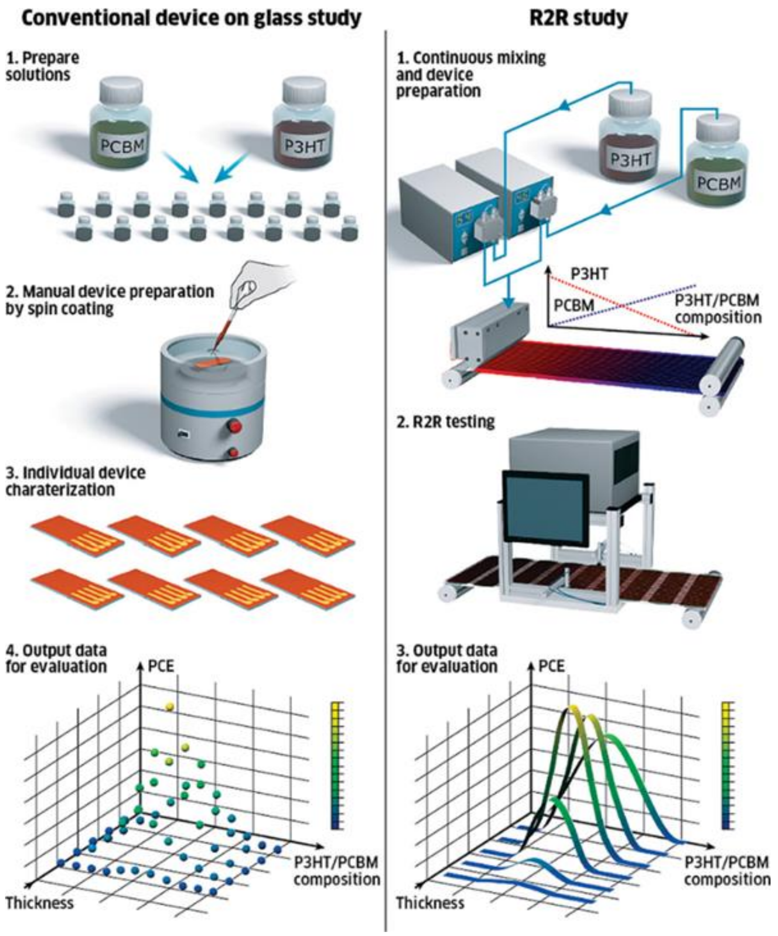

Figure 2- 3. Fragmentary vs. continuous-composition high-throughput synthesis of organic thin films (Reprinted with permission from ref. [76]). The left panel depicts the preparation of thin film libraries by fragmentary approach in which distinct thin film compositions are made and studied. The right panel depicts the preparation of thin film libraries by a continuous optimization approach in which thin film composition is graded across the film. PCBM stands for Phenyl-C61-butyric acid methyl ester, P3HT stands for Poly(3-hexylthiophene-2,5-dial), PCE stands for power conversion efficiency of solar cells, and R2R stands for roll-to-roll processing.

We recently developed a solution-processed approach for fabricating compositionally-graded films[74]. Our approach uses slot-die coating with two pumps, each programmed to supply different solutions at a gradient rate in order to *in-situ* change the output composition. Figure 2-4c illustrates an example of our compositionally-graded film prepared from $MAPbI_3$ and $MAPbBr_3$ perovskites. The transition of color from pure $MAPbI_3$ (black) into the pure $MAPbBr_3$ (orange) indicates the linear gradient composition of $MAPb(I_xBr_{1-x})_3$. The film was characterized by measuring absorption and photoluminescence spectra in >200 locations, indicating a gradual shift of bandgap across the film (Figure 2-4c). Access to the compositionally-graded films has also enabled the observation of three distinct degradation mechanisms of perovskite alloys, depending on halide content: iodide-rich perovskites degraded through desorption of organic component, bromide-rich perovskite through hydration, while all intermediate alloys through phase segregation.[74] Stabilization of perovskite materials and solar cells is a subject of intense investigation.

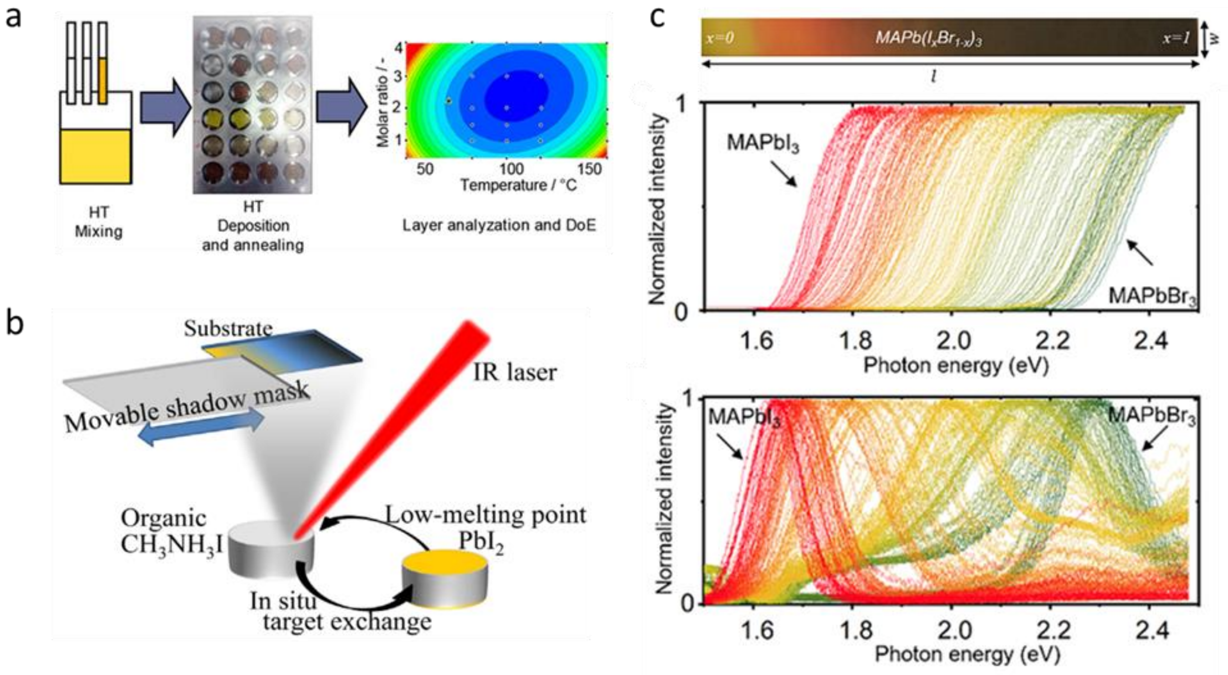

Figure 2- 4. Fragmentary vs. continuous high-throughput synthesis of perovskite thin films. **a**, Fragmentary HTS of thin films made by spin-coating (Reprinted with permission from ref. [73]). **b**, Continuous compositionally-graded films synthesized by co-evaporation of two precursor materials (Reprinted with permission from ref. [79]). **c**, Top view of perovskite compositionally-graded film (top panel) made by a slot-die coating of two precursor inks and characterized by absorption (middle panel) and photoluminescence (bottom panel) spectroscopy (Reprinted with permission from ref. [74])

2-4-2. Light-emitting diodes

Replacing inefficient conventional light sources, which utilize one-third of electricity globally,[84] with power-saving LEDs could play a major role in the conservation of energy. LEDs based on perovskites offer high external quantum efficiency, pure colors, and tunable emission spectra[85]. However, most-wanted blue perovskite LEDs suffer from low performance compared to red and green ones[86]. HTS platforms are currently used to discover stable and efficient blue LEDs.

Figures 2-5 a-b shows a fragmentary approach for optimizing blue-emitting perovskite thin films[87]. Through composition engineering by incorporating Cl into the $CsPbBr_3$ lattice, the work first finds that the perovskite of $CsPbCl_{0.9}Br_{2.1}$ composition offers a blue emission centered at 484 nm. Phenylethyl ammonium bromide is subsequently introduced into the $CsPbCl_{0.9}Br_{2.1}$ perovskite to passivate the traps and improve photoluminescence quantum yield from 0.15% to a maximum of 27%.

Figures2-5 c-d show a continuous approach toward the optimization of perovskite composition for LEDs[88]. The work uses dual-source physical vapor deposition of CsBr and $PbBr_2$ to prepare continuous gradient films. The Cs/Pb ratio in the perovskite film gradually changes from one part to another part of the film. The observed trend of device efficiency is explained as a trade-off between photoluminescence quantum yield and injection efficiency (resistivity): samples with high injection efficiency (low resistivity) and low photoluminescence quantum yield (and vice-versa) lead to low LED efficiency. The LED performs best when these two figures are balanced, achieved in samples with a Cs/Pb ratio of 1.17/1.

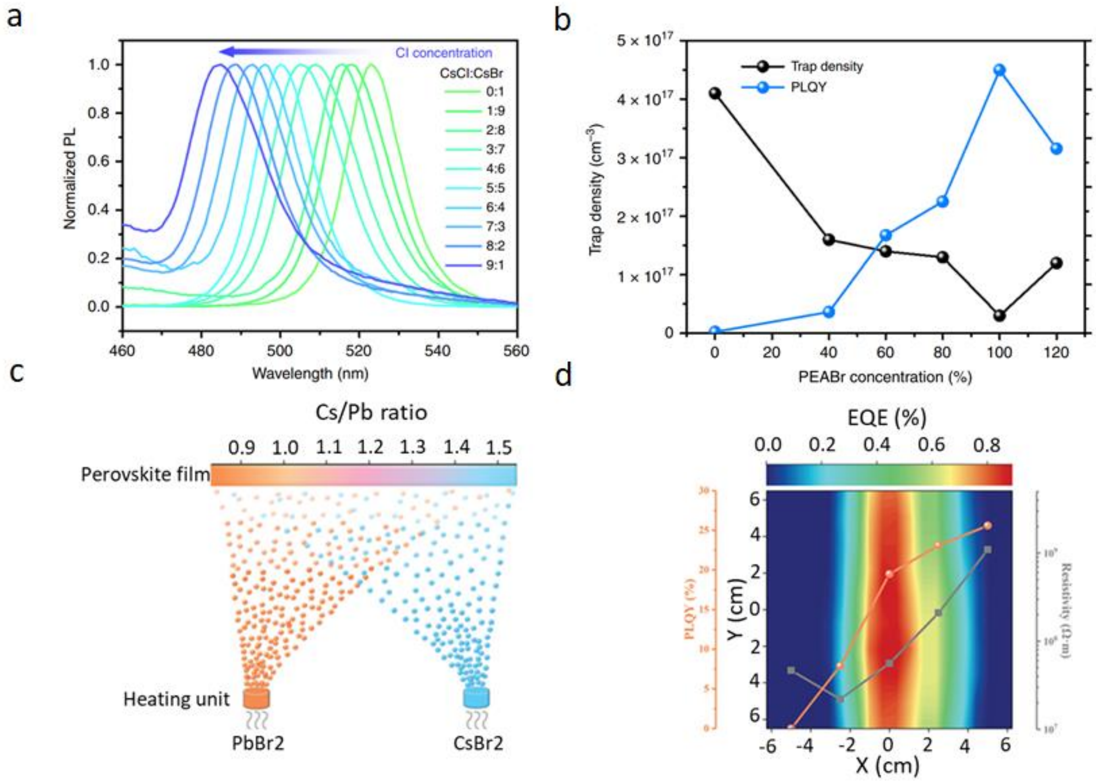

Figure 2- 5 Fragmentary vs. continuous high-throughput synthesis of perovskite thin films for LEDs. **a,** Photoluminescence (PL) spectra of $CsPbCl_xBr_{3-x}$ thin films with different molar ratios of CsCl to CsBr. Reprinted with permission under a Creative Commons CC BY License from ref 74. Copyright 2019 Springer Nature. **b,** Trap densities and photoluminescence quantum yields (PLQYs) of $CsPbCl_{0.9}Br_{2.1}$ thin films with different ratios of phenyl-ethyl ammonium bromide (PEABr). Reprinted with permission under a Creative Commons CC BY License from ref 74. Copyright 2019 Springer Nature. **c,** Schematic of dual-source co-evaporation deposition for perovskite film. Reprinted with permission from ref 75. Copyright 2019 John Wiley and Sons. **d**, Spatially resolved external quantum efficiency (EQE mapping of assembled devices;

photoluminescence quantum yield and (PLQY) and resistivity of perovskite films. Reprinted with permission from ref 75. Copyright 2019 John Wiley and Sons.

2-4-3. Batteries

There is an urgent need for high-capacity, low-cost, and stable energy storage devices. Thin films can offer a critical platform for screening the desired properties of battery materials such as ionic diffusivity, capacity, phase stability, and volume expansion[89]. HTS of thin films is widely used in the development of anodes[90], cathodes[91], solid electrolytes[92] [93], as well as organic electrode materials[94] [95]. The fragmentary HTS approach is common in synthesizing multinary battery material compositions. High-throughput sol-gel synthesis was earlier used to optimize magnesium doping concentration for lithium ferrophosphate ($LiFePO_4$), a material of great interest as a safe, environmentally friendly cathode for lithium-ion batteries (Figure 2-6a) [96]. The work has shown that magnesium substituted for iron in a precursor mixture ($LiFe_{(1-y)}Mg_yPO_4$) showed better battery performance than when magnesium substituted for lithium in a precursor mixture ($Li_{(1-x)}Mg_{x/2}FePO_4$). A similar approach has been utilized for optimizing sodium-ion battery cathodes, particularly the Na-Fe-Mn-O pseudo ternary system of high immediate interest[36] (Figure 2-6b).

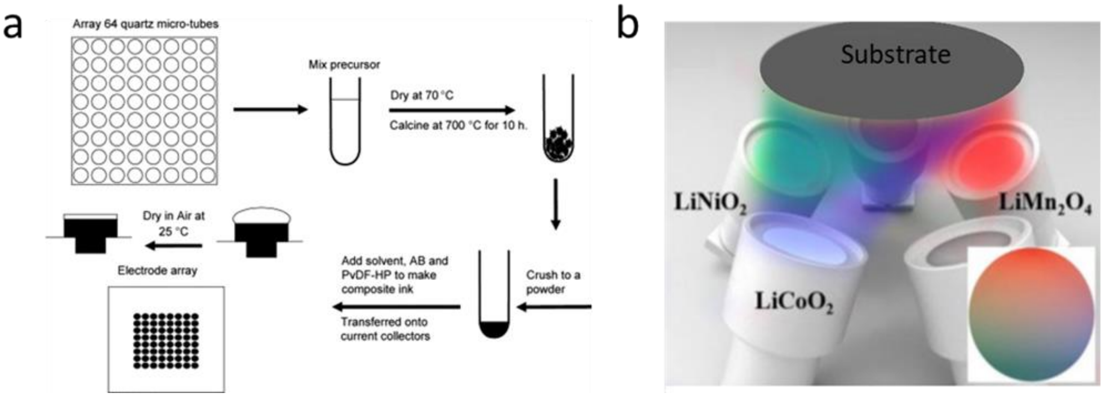

Figure 2- 6. Fragmentary vs. continuous high-throughput synthesis of thin films for battery applications. **a,** Fragmentary HTS of $LiFe_{(1-y)}Mg_yPO_4$ and $Li_{(1-x)}Mg_{x/2}FePO_4$ (Reprinted with permission from ref. [96]); **b,** Continuous compositionally-graded films synthesized by co-deposition of five precursors (Reprinted with permission from ref. [36]).

2-4-4. Superconductors

The lack of an extensive material library of superconductors makes it challenging to investigate the mechanism of much-needed high-temperature superconductivity. HTS platforms could provide access to a more comprehensive library of superconductive materials[97].

Figure 2-7a illustrates an example of the preparation of a superconductor material library. $Fe_{70}Co_{30}$ and V alloys using a shadow mask were deposited on a film grid[98]. Then hysteresis loops across the material library were measured. The co-sputtering technique with a gradient deposition was also used in studying Fe-B binary systems on a Si wafer[99],[100].

Figure 2-7b depicts the schematic of a continuous composition-gradient film made of high-temperature superconducting compound $YBa_2Cu_3O_{\nabla x}$, wherein the oxygen content (x) spatially varies across the length of the sample[101]. The $YBa_2Cu_3O_x$ films were grown on a <001> $SrTiO_3$ substrate using the pulsed laser ablation method[102]. The continuity nature of oxygen pressure and thermal effects along the film enables the fabrication of this graded film.

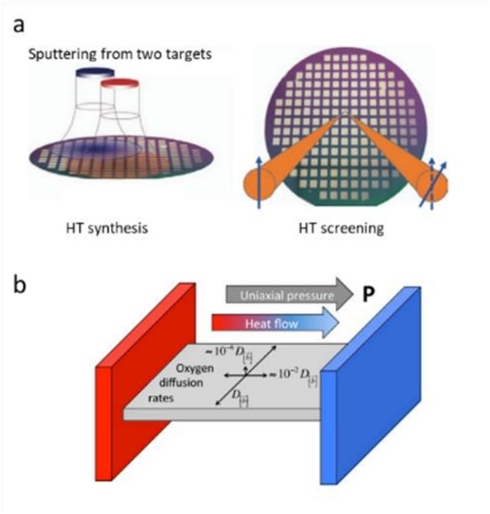

Figure 2- 7. Fragmentary vs. continuous HTS of thin films for superconducting materials. **a,** Fragmentary co-sputtering $Fe_{70}Co_{30}$ and V synthesis (Reprinted with permission from ref. [98]), **b,** Continuous compositionally-graded $YBa_2Cu_3O_x$ (Reprinted with permission from ref. [101]).

2-4-5. Thermoelectrics

Thermoelectric materials are generally used in bulk form, but thin films can offer a platform for optimizing thermoelectric properties such as thermal diffusivity, carrier mobility, Seebeck coefficient, and other figures-of-merit as a function of chemical composition[103]. The limited number of known thermoelectric materials and their low-efficiency demand for HTS techniques to discover and develop novel thermoelectric materials.

Synthesis of gradient film from a ternary system ($CoSb_3$-$LaFe_4Sb_{12}$-$CeFe_4Sb_{12}$) made by pulsed laser deposition was earlier reported [104]. A thermoelectric screening tool (Figure 2-8a) capable of performing a temperature-dependent study spatially measuring the continuous gradient film's Seebeck coefficient and electrical resistivity (Figure 2-8b)[104] HTS of thin films were also applied to study several other thermoelectric materials such as $(Ca_{1-x-y}Sr_xLa_y)_3Co4O_9$[105], Ti-Ni-Sn[106], and Al-Fe-Ti[107].

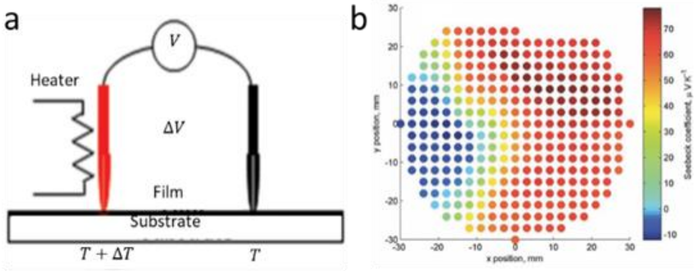

Figure 2- 8. **a,** High-throughput temperature-dependent Seeback coefficient screening tool. (Reprinted with permission from ref.[104]). **b,** Seebeck coefficient contour plots for a ternary $CoSb_3$-$LaFe_4Sb_{12}$-$CeFe_4Sb_{12}$ combinatorial film deposited on a quartz wafer (Reprinted with permission from ref. [104]).

2-5. Conclusion and outlook

Developing HTS of thin films is important to accelerate the exploration and investigation of much-needed new materials to address some global challenges such as accessible and renewable energy capture, storage, and transport. Thin films offer a unique platform for HTS of multi-component compositions. Thin films are also compatible with many commercial devices. As discussed above, fragmentary (discontinuous) alloy optimization is the most widespread, but it misses intermediate compositions. In contrast, compositionally-graded films cover all-possible alloys and hence offer access to the entire parameter space. The following challenges and opportunities exist in the HTS of thin films.

Synthesis of multinary compositions (containing three or more components) on a substrate is a challenge. In this regard, evaporation techniques with controllable parameters such as deposition speed, movable masks, and substrate rotation enable printing up to senary (6 components) phases. The gradient films with a higher number of components are harder to make, but microfluidic platforms that store all-compositional spaces may allow the printing of multinary compositions.

Another challenge is the improper mixing of precursors, leading to inhomogeneous thin films due to local phase segregation. Proper mixing can be achieved by co-evaporation (for physical-vapor deposition) and turbulent flow of inks (for solution-processed deposition). This is particularly a challenge for physical vapor deposition techniques in which a slow process may lead to local phase segregation. In contrast, solution-processed techniques such as slot-die coating provide a reservoir to ensure proper mixing of inks before being deposited on a substrate.

Finally, high-throughput characterization techniques are yet to be developed to study the local properties of thin films. It is already possible to measure optical properties (absorption and photoluminescence) in a high-throughput manner. However, measuring local composition (e.g., by X-ray fluorescence), structure (e.g., by X-ray diffraction), or electrical properties (e.g., by the four-point probe) remains time-consuming.

Chapter 3: Experimental methods

3-1. Abstract

As we discussed earlier in Chapter 2, the synthesizing methods for optimizing multinary compositions are fragmentary and continuous. In this dissertation, we will discuss continuous synthesis for binary and ternary compositions with which we will be able to optimize the most stable combinatorial compositions for perovskite materials. In this chapter, we present the ingredients and materials required for the synthesis of thin films. In addition, the methods of fabrication and characterization instruments for PSCs, binary, and ternary optimization methods will be elaborated.

3-2. Materials and preparation

3-2-1. Materials

Cesium iodide (CsI, > 99.99%) was purchased from Millipore Sigma. Formamidinium iodide (FAI, >99.99%), methylammonium iodide (MAI, >99.99%), and methylammonium bromide (MABr, >99.99%) were purchased from Greatcell Solar Materials, lead(II) iodide (PbI_2, 99.99%) from TCI Chemicals, as perovskite precursors. N, N-dimethyl formamide (DMF, 99.5%), dimethylsulfoxide (DMSO, 99.5%), chlorobenzene (99.5%), and acetonitrile (ACN, ≥99.9%) solvents were purchased from MiliporeSigma. Tin (IV) oxide (SnO_2) 15% in H_2O colloidal dispersion solution was purchased from the Alfa Aesar. Sprio-OMeTAD was purchased from Xi'an Polymer Light Technology Co., Ltd. Bis (trifluoromethane) sulfonimide lithium salt (Li-TFSI 99.95%) and cobalt salt (FK 209 Co(III) TFSI) were purchased from MiliporeSigma.

3-2-2. Material preparation

All chemicals and solvents were used without any further modification. For CGF fabrication, we prepare perovskite inks by dissolving methylammonium halides CH_3NH_3X (X = Br or I) and PbX_2 in dimethylformamide (DMF) to prepare 1 M solutions. For t-CGF we used different perovskite inks with different concentrations by dissolving MAI (CH_3NH_3I), FAI (CH_5IN_2), CsI, and PbI_2 in DMF and dimethyl sulfoxide (DMSO) with the ratio of (4:1) to prepare 1.4 M, 0.7 M, and 0.28 M solutions of $FAPbI_3$, $MAPbI_3$, and $CsPbI_3$, respectively

3-3. Fabrication

We fabricated binary compositionally-graded film (CGF), ternary compositionally-graded film (t-CGF), and both small and large-size PSCs. We used a slot-die coating technique with two pump Research Laboratory Coater (RLC) of infinityPV to fabricate CGF and t-CGF. For small-sized PSCs, we used a spin-coater, but for large-sized PSCs, we utilized a blade coater. Figure 3-1 a-c shows the slot-die coater, spin-coater, and blade coater, respectively. We used a thermal evaporator to deposit gold contacts on PSCs (Figure 3-1d).

Slot-die coating is a solution-based deposition of thin films onto typically a substrate with a flat surface. A solution is made of dissolving precursor, also called ink, is delivered to the surface of the substrate through a slot-die coater's head. The head has a high aspect ratio outlet that controls the interaction of ink with the substrate. The aspect ratio and thickness of the thin film can be adjusted by controlling the gap size, height, and speed of the head during the deposition process.

Spin coating is a common technique for applying thin films to substrates. By spinning a drop of solution on substrates, the material and a solvent is spun at a determined high speed. The applied centripetal force and surface tension of the ink together cause an even covering of the wet film that can be annealed after the process. The thickness of the thin films can be controlled by the speed and concentration of the ink.

Blade coating is a method of depositing a smooth thin film on a substrate. The blade has a sharp adjustable distance from the surface of the substrate that is needed to be covered. After placing the solution in front of the blade, the blade moves across in line with the surface creating a wet film. The nitrogen blowing can aid to crystallize the solution and passivate the surface of the thin film at the same time.

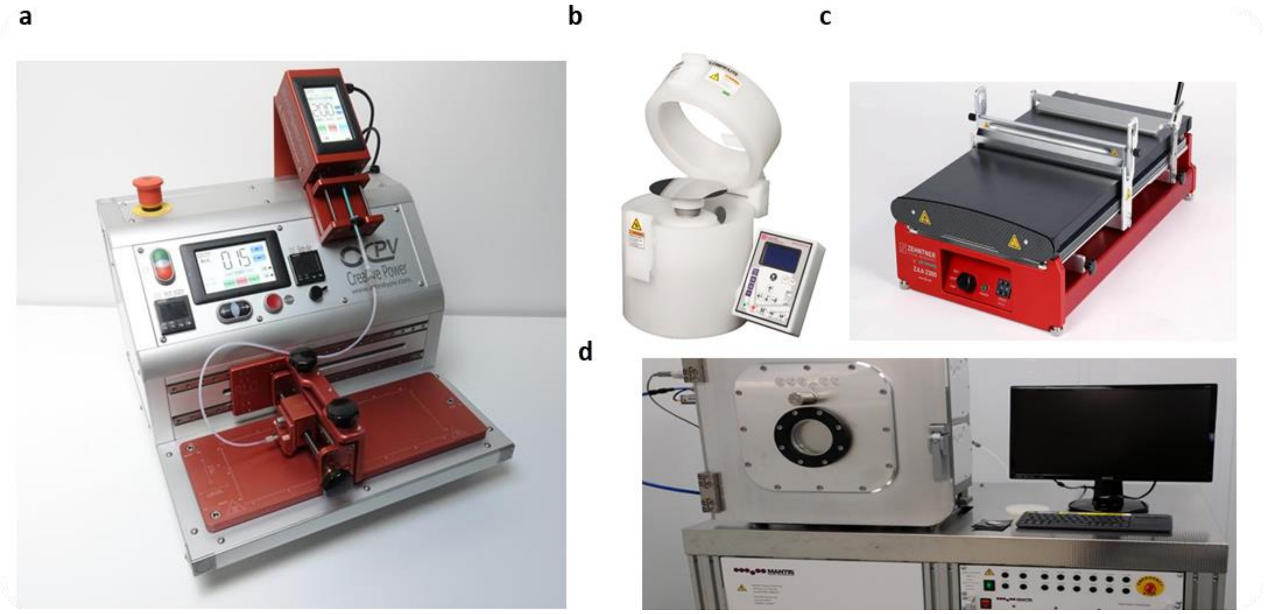

Figure 3- 1. Instruments for fabrication: **a.** Research Laboratory Coater (RLC) for slot-die coating. **b.** Spin-coater. **c.** Blade-coater. **d.** Thermal evaporator.

3-3-1. CGF fabrication

Slot-die coating profile of CGFs is shown in Supplementary Figure 4-1. Two solutions were placed in two Research Laboratory Coater (RLC) of infinityPV ApS slot-die coater pumps. First, the dead volumes (from syringes to the end of the Y junction) were filled with inks at a speed of 0.05 ml/min, and then the Y junction was attached to the slot-die head. Second, the slot-die head was filled with one ink until the ink appeared at the tip of the head at a speed of 0.24 ml/min. Third, the first ink supply is stopped, but the second ink is pumped at 0.3 ml/min speed simultaneously depositing the solution on the substrate. The mixed solution was deposited on a glass substrate placed on a hot plate with a fixed temperature of 140 ºC. The supplementary Movie [74] shows the appearance of fabricated CFG.

3-3-2. t-CGF fabrication.

Perovskite inks were made by dissolving MAI, FAI, CsI, and PbI_2 in DMF and DMSO with the ratio of (4:1) to prepare 1.4 M, 0.7 M, and 0.28 M solutions of $FAPbI_3$, $MAPbI_3$, and $CsPbI_3$, respectively.

Slot-die coating was performed on InfinityPV Research Laboratory Coater (RLC) following profiles shown in supplementary figure 4-1 (Appendix A). $CsPbI_3$ was deposited using one pump with a tilted head: first, the dead volume and the reservoir were filled, and then the film was deposited at a small speed. $MAPbI_3$ and $FAPbI_3$ were deposited in gradient thickness using two pumps. The dead volumes (from syringes to the end of the T junction) were filled with inks at a speed of 0.01 ml/min, and then the T junction was attached to the slot-die head. The time required to fill the slot-die head until the appearance of ink at the tip of the head at a speed of 0.3 ml/min was measured to be 56 s. Then the first ink supply was paused, but the second string containing DMF and DMSO with a 4:1 ratio was pumped at the same speed of 0.3 ml/min. The speed of the moving head along the 260 mm was installed to be 260 mm/56 s = 4.64 mm/s to be able to linearly dilute the stored ink in the reservoir. $MAPbI_3$ and $FAPbI_3$ were deposited in opposite directions. The first and second layers were fabricated at 70°C; the final layer was deposited at 140°C.

3-3-3. PSC fabrication

The UV-Ozone treated glass/ITO substrates were coated with SnO_2 by dropping 60 µl of mixed SnO_2:H_2O (1:6). We used 6 ml deionized (DI) water and 1 ml of SnO_2 15% in H_2O colloidal dispersion nanoparticles and then sonicated for 30 minutes and filtered with 0.45 µm polyvinylidene difluoride (PVDF) syringe filter before deposition. 60 µl of the prepared tin oxide solution is dropped and spin-coated for 1 minute with 3000 r.p.m., and repeating the process twice. Then the substrate was annealed at 140 °C for 20 minutes and treated with UV-Ozone for 15 minutes. Perovskite solution was prepared by dissolving 1 molar mass of combinatorial ratios of CsI, MAI, FAI, and PbI_2 on 0.666 ml of DMF : DMSO with the ratio of 1:10. Then 90 µl of mixed-cation, single-halide perovskite (1.5 M) in the ambient air was deposited by a spinner at 500 r.p.m. for 5s, 1000 r.p.m. for 5s, and 4500 r.p.m. for 30s. During the last step, 500 µl of chlorobenzene was dropped on the film at 30 s, followed by annealing at 140 °C for 10 min. Spiro-OMeTAD solution was prepared by dissolving 0.1 mg of spiro-OMeTAD powder in 1.1 ml of chlorobenzene, 0.039 ml of tBP, 0.023 ml of Li-TFSI (dissolved in acetonitrile, 540 mg/mL), and 0.01 ml of Co-complex (dissolved in acetonitrile, 376 mg/mL) solution. Then 60 µl Spiro-OMeTAD was dynamically spin-coated for 30 s. Finally, 70 nm gold was thermally evaporated (Angstrom Engineering). All the solutions, i.e. perovskite and spiro-OMeTAD, were filtered with a 0.22 µm polytetrafluoroethylene (PTEE) syringe filter.

3-4. Characterization

We used different tools for measuring our fabricated samples. For measuring the current-voltage characteristics of our PSCs, we used a solar simulator (Figure 3-2a). To measure the durability of the devices with different compositions, we used a Maximum-Power-Point box (Figure 3-2b) with which the temperature of the environment can be elevated for accelerating the degradation mechanism. Figure 3-2c shows the spectrometer that is applied to measure photoluminescence and absorption spectra in both CGF and t-CGF. In addition, we used a robot arm (Figure 3-2d) to increase the accuracy of measurements which is very essential for high-throughput screening purposes.

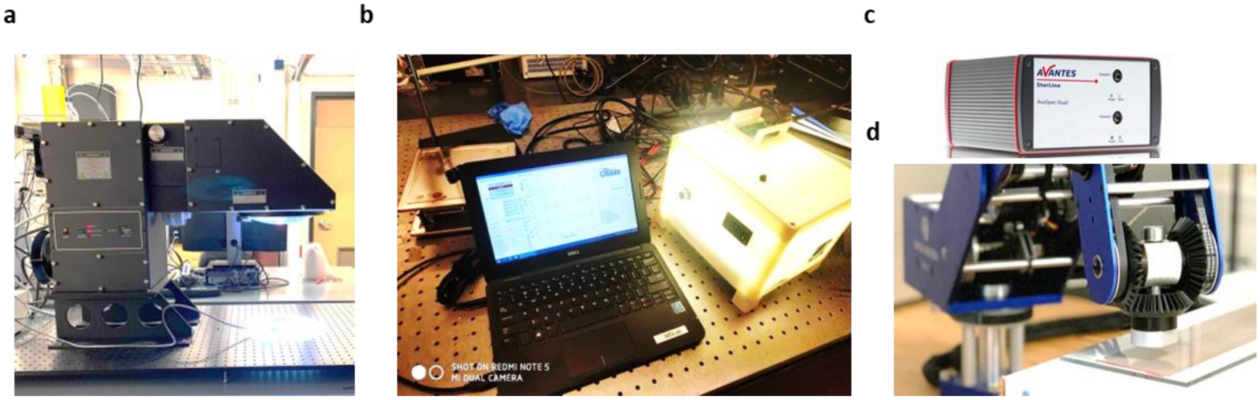

Figure 3- 2. Characterization tools: **a.** Solar simulator, **b.** Maximum-power-point (MPP) box, **c**. Spectrometer with Xenon lamp, **d.** Robot arm.

The solar simulator produces illumination approximating natural sunlight in order to provide an indoor test tool for laboratory applications. The provided spectrum illuminated by the solar simulator should resemble the AM1.5 spectrum. The instrument simulates sunlight, and we use an Ossila source meter to record the measuring parameters of the PSCs. The main parameters that we need to quantify the performance of PSCs are peak power (P_{max}), the short-circuit current density (J_{SC}), the open circuit voltage (V_{OC}), and the fill factor (FF). The reliable J-V measurement requires standard test conditions in which the total irradiance on the solar cell should be equal to 1,000 watts per meter squared.

We measure current-voltage (J-V) characteristics after placing the PSCs under direct exposure to the solar simulator's light. The contacts (e.g., cathodes and anodes) of the PSC are attached to the circuitry board that is considered a probe of the Ossila source meter. The experiment of result aims to measure the power conversion efficiency (η) of PSCs through the measured J-V characteristics. The J_{SC} is the current that flows through the external circuit while the solar cell is shorted. The J_{SC} depends on the photon flux that is interacting with the PSC. The current density also has direct proportionality on the area of the cell that is interacting with the solar simulator. The V_{OC} is the voltage at which no current flows through the PSC. It is considered the maximum voltage that a PSC can deliver.

The fill factor (FF) is the ratio between the maximum power point ($P_{max}=J_{mpp}.V_{mpp}$) and an ideal maximum power point ($P_{ideal}= J_{SC}.V_{OC}$): $FF=(J_{mpp}.V_{mpp} / J_{SC}.V_{OC})$. The power conversion efficiency is calculated as the ratio between the maximal generated power and the incident power coming from the solar simulator with an irradiance of I_{in}=1000 W/m^2. The η is a fraction or percentage of generated power over input which is calculated from $\eta = P_{max}/I_{in} = (J_{SC}.V_{OC}.FF)/I_{in}$.

For the durability test, we have the MPP test box that is connected to the probe of the Ossila source meter (Figure 3-2b). The maximum power point operation is also considered as a stability evaluation of the PSCs. The MPP box provides some stressed conditions such as room temperature in relative humidity (RH) of 40%, with an elevated temperature (e.g., 60 ^{O}C). Since an Xe lamp that provides a closer spectrum to AM1.5 has a short lifetime, we use a white LED instead as a light source that has a limited visible spectrum to those of Xenon lamps. However, the generated carrier concentration for both lamps is similar and the replacement with theLED is negligibly impacting the performance of PSCs.

The gradient film measurements of all compositions were carried out via a UV-Vis AVENTES spectrometer (AvaSpec-ULS2048CL-EVO-RS) in the reflection mode. The absorption spectra of the gradient film were recorded in the wavelength range of 500-780 nm at the ambient temperature with an auto-saving option every 200 ms while moving the reflection probe through the gradient film. Using the same spectrometer in the reflection mode ranging from 500-780 nm, we measured the photoluminescence (PL) peaks in a dark room every 2 s. A Dorna 2 robotic arm (Dorna robotics) was used to automate the process of acquisition of CGF's optical properties.

We also used other shared facilities that are available within the Centre for Advanced Materials and Related Technology (CAMTEC) for characterization that is applied for validation of our current experiments such as accomplishing powder X-ray diffraction (pXRD), nuclear magnetic resonator (NMR) and scanning electron microscopy (SEM).

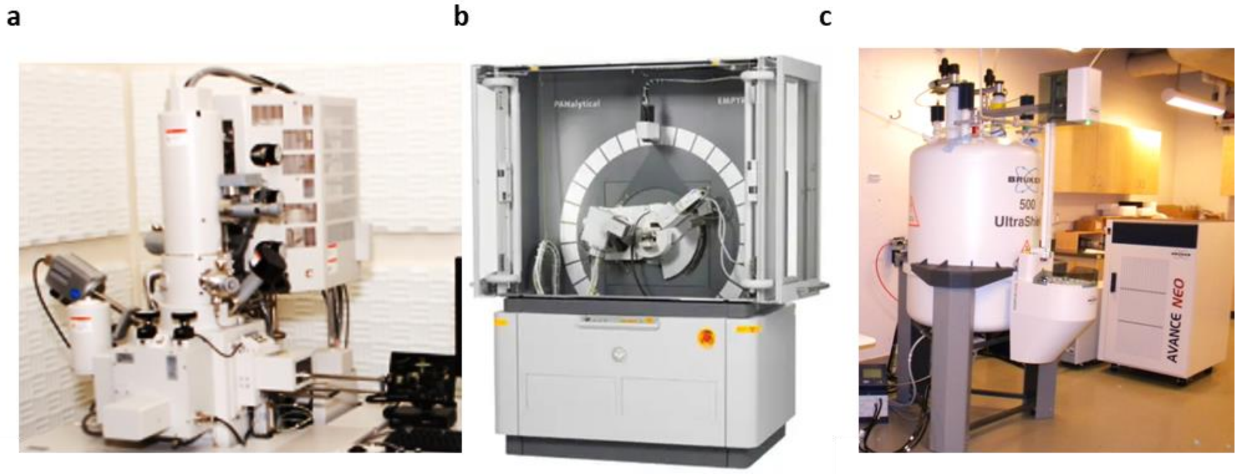

Figure 3- 3. Characterization facilities: **a,** Scanning electron microscopy. **b,** PANalytical Empyrean small angle X-ray scattering (SAXS) for powder X-ray diffraction measurement. **c,** Nuclear magnetic resonance.

SEM images were captured with a Hitachi S-4800 FESEM. EDX was taken on a Bruker Wuantax EDS system from Hitachi S-4800 FESEM (Figure 3-3a). For XRD measurements, a PANalytical Empyrean system using a Cu source (K_α 1.5406 Å) was used. The data were collected in high throughput manner using a SAXS stage and PIXce12D detector (Figure 3-3b). NMR spectra were acquired with a Bruker AVANCE-III 300 MHz spectrometer (Figure 3-3c).

Chapter 4: High-throughput exploration of halide perovskite Compositionally-Graded Films and degradation mechanisms

Note: This chapter has multi-author contributors, I have contributed to developing the binary optimization, synthesis of CGF via a slot-die coating, robotizing the characterization, measuring the absorption and photoluminescence spectra, writing the MATLAB codes, analyzing the data and plotting the figures.

4-1. Abstract

Functional materials are always looked after to address shortcomings of state-of-art devices. The conventional approach to search for new material compositions is to synthesize and study a limited number of alloys; however, this fragmented approach misses a significant fraction of material alloys, which delays or disables the discovery of potential ‘magic’ compositions. Here we report a strategy for fabricating compositional gradient films to synthesize all possible alloys from binary systems in a single shot in less than 1 min. We use our approach to study an applied challenge – the stability of halide perovskites, a promising and fast-growing class of semiconductors for various optoelectronic applications. We synthesize all possible phases from a binary system of $MAPbI_3$ and $MAPbBr_3$, and then study their optical, structural, and stability properties in a high-throughput manner. We find that perovskite alloys experience three different degradation mechanisms depending on halogen content: Br-rich perovskites degrade through hydration, while I-rich perovskites do so the loss of organic component; all other intermediate alloys degrade through segregation to Br-rich perovskite and lead iodide. The proposed method of fabricating compositional gradient films paves avenues for discovering new materials and processing parameters for a broad range of applications that rely on compositional engineering.

4-2. Introduction

Novel material compositions are always sought after to achieve new benchmarks in photovoltaics[18],[108], thermoelectrics[109], piezoelectrics[110], catalysis[111], batteries[112], superconductors[113], magnetism[114], pharmaceuticals[115], lasers, LEDs[116], and other fields.

Materials science has hitherto mainly relied on a “trial-and-error” approach that led to many important – but primarily serendipitous – discoveries of new materials or processing parameters[117]. For instance, NiTi shape memory alloy is one example of serendipitous discovery[118]. A more recent example is the discovery of a noble metal-free nanoparticulate electrocatalyst, CrMnFeCoNi, with catalytic activity for the oxygen reduction reaction[119]. Given that the number of potential compounds rises exponentially in multi-atom mixtures, there is a need for a more efficient and systematic search for new materials[120–127].

High-throughput methods[128],[129] are developed to accelerate the discovery of materials by searching through ever-increasing vast space of multi-atom compositions[130]. In addition, high-throughput approaches provide access to big data that is now being used to train machine learning algorithms[131], which predict and sometimes make new materials[19]. In both high-throughput and machine learning-assisted search, the output heavily relies on the number of available data sets[132],[133]. Figure. 4-1a depicts a common strategy in conventional high throughput methods for compositional engineering[42], when several compositions are combinatorially prepared and studied. However, this ‘fragmented approach’ provides discrete data sets[134], which, unfortunately, misses most of the compositions in between to form a complete experimental data set. Therefore, there is a significant need for a comprehensive method of fabrication of multinary phases to search for new compositions in a systematic manner[20,65,135].

Here we show an approach for a synthesis of all possible phases in binary systems in one shot. We achieve this by developing a strategy for the fabrication of compositional gradient films (CGFs), where the film starts with one composition and gradually transitions to another through alloying. We apply our strategy to study a binary system of $MAPbI_3$ and $MAPbBr_3$ perovskites, a promising and fast-growing class of semiconductors for optoelectronics. In particular, perovskite solar cells recently achieved 25.5% power conversion efficiency[7], which is large is due to compositional engineering. Using our method, we prepare hundreds of perovskite alloys in less than 1 min, then study their optical and structural stability in a high throughput manner and report compositionally stable alloy regions.

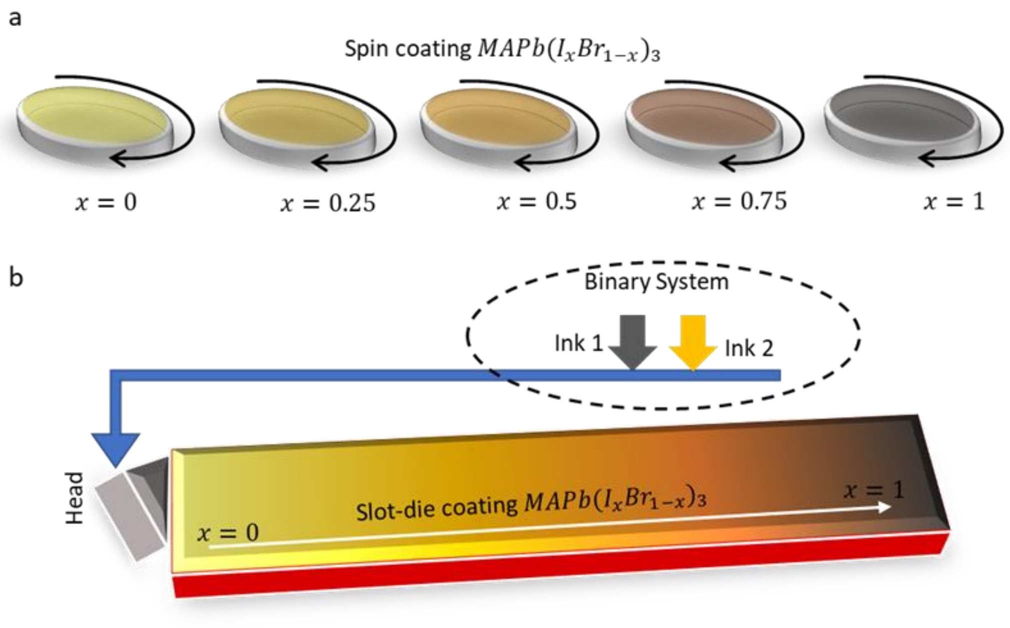

Figure 4- 1 Schematic of approaches for material composition optimization. **a,** Conventional approach to fabricate a limited number of compositions; **b,** Fabrication of compositional gradient films (CGFs) that include all possible phases from binary systems in one shot.

4-3. Results and discussion

We chose a slot-die coating method to fabricate CGFs. This method is promising for roll-to-roll fabrication and commercialization of solution-processed materials, including polymer and perovskite solar cells and light-emitting diodes[136],[137]. Therefore, using slot-die coating will allow simultaneous optimization of processing parameters to develop device-integrable thin films.

The slot-die coating method uses a pump to supply a solution to a slot-die head that prints material on a substrate. We added a second pump and connected the outputs of the two solution supplies (Figure. 4-1b) using a unidirectional Y junction. The liquid mixture then flows into a slot-die head reservoir where it experiences a sudden change in cross-section area and shape (from circular to truncated cylinder), leading to proper mixing[138].

We first programmed one pump to decrease its solution supply gradually while the other pump increased it. However, this approach led to nonlinear and discontinuous gradient films due to the delayed arrival of the second ink as it starts at a low speed. We then alternated the ink supply using the slot-die coating profile depicted in Supplementary Figure 4-1. After filling the slot-die head with one ink, we stopped its supply and started supplying the second ink at high speed, simultaneously moving the slot-die along the substrate. This alternated ink supply approach allowed for the *in-situ* mixing of two solutions and *in-situ* gradient change of the final solution composition and enabled the fabrication of CGFs, as we show below.

Figure 4-2a,b show top- and side-views of CGF prepared from $MAPbBr_3$ and $MAPbI_3$ solutions on a 28 cm long substrate fabricated within less than 1 min. The visual appearance of the film, i.e., continuous yellow-to-black transition through the film, indicates that the film is made of $MAPbBr_3$ and $MAPbI_3$ at $l = 0$ and $l = 28$ cm, respectively, and all possible $MAPb(I_xBr_{1-x})_3$ alloys while moving through the length of the film from one side to another.

To validate the gradient nature of the CGF, we measured the absorption bandgap along the center of the film. We used a robotic arm to slide a spectrometer's reflection probe to measure CGF's optical properties in equally-spaced 215 locations along the center of the film (Supplementary Figure 4-2). We then processed the data using a MATLAB code to compute the Tauc plot and the bandgaps (Figure. 4-2d,e). The bandgaps of the CGF indeed gradually decrease from 2.23 to 1.62 eV while moving from $l = 0$ to $l = 28$ (cm), validating the successful formation of all alloys on a single film. Raw absorption figures are shown in Supplementary Figure 4-3.

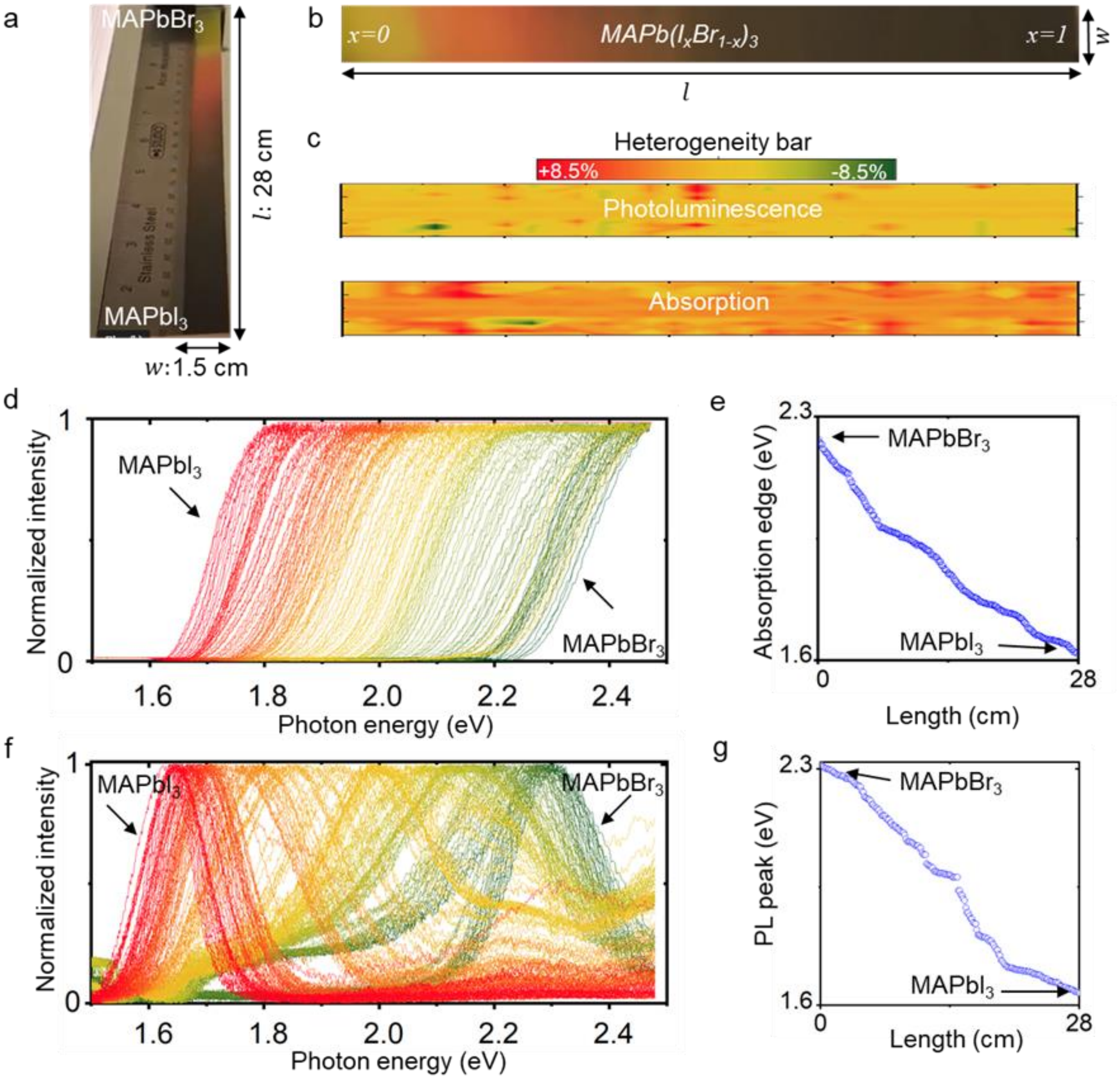

Figure 4- 2 Characterization of CGF. **a,** side-view and **b,** top-view of CGF; **c,** Quantification of heterogeneity across the width of the CGF by normalizing absorption and PL bandgaps to the center of the CGF; **d,** Normalized absorption Tauc plots of fresh CGF and **e,** extracted absorption bandgaps for 215 locations; **f,** Normalized PL spectra of fresh CGF and g) extracted PL bandgaps for 215 locations.

Next, we measured the photoluminescence (PL) of the CGF using the same optical probe (raw figures are shown in Supplementary Figure 4-4). We then processed the data using MATLAB code (MATLAB File 2) to normalize the PL spectra (Figure. 4-2f) and calculate the PL bandgaps (Figure. 4-2g). As expected, the PL bandgaps of the CGF follow the absorption bandgap trend (Figure. 4-2g, f).

Supplementary Figure 4 shows ras PL data and extracted PL intensity and the full-width at half-maximum (FWHM) of the CGF. The bromide ($x < 0.15$) and iodide-dominant ($x > 0.7$) regions show excellent PL color purity with FWHM of less than 40 nm, while $MAPb(I_xBr_{1-x})_3$ alloys demonstrate significantly broad FWHM exceeding 50 nm, likely due to phase segregation[139],[140],[141]. The bromine-dominant perovskite region along the film shows strong PL peaks, in line with the recent findings of impressive green-emitting Br-rich perovskites[142].

We also performed micro-X-ray diffraction (mXRD) (Figures 4-3b) to gain insights into the structural evolution of the CGF along the film. The first-order reflection of (001) planes has gradually shifted to lower diffraction angles (larger unit cell parameters), with the increase of l indicating of successful formation of solid $MAPb(I_xBr_{1-x})_3$ alloys along the film[143].

To quantify film heterogeneity across the width of the CGF, we measured the absorption, and PL bandgaps along 11 parallel lines distanced 1 mm from one another using the robotic arm. We then normalized the bandgaps to the center of the CGF and show thus-obtained color maps in Figure 4-2c. The figures demonstrate excellent homogeneity of the CGFs across the film (width); heterogeneity does not exceed ±8.5% and is mainly located at the edges of the film likely due to delayed exit of the ink from the sides of the slot-die head (positive heterogeneity values) or advanced release of ink due to roughness of the substrate (negative heterogeneity values).

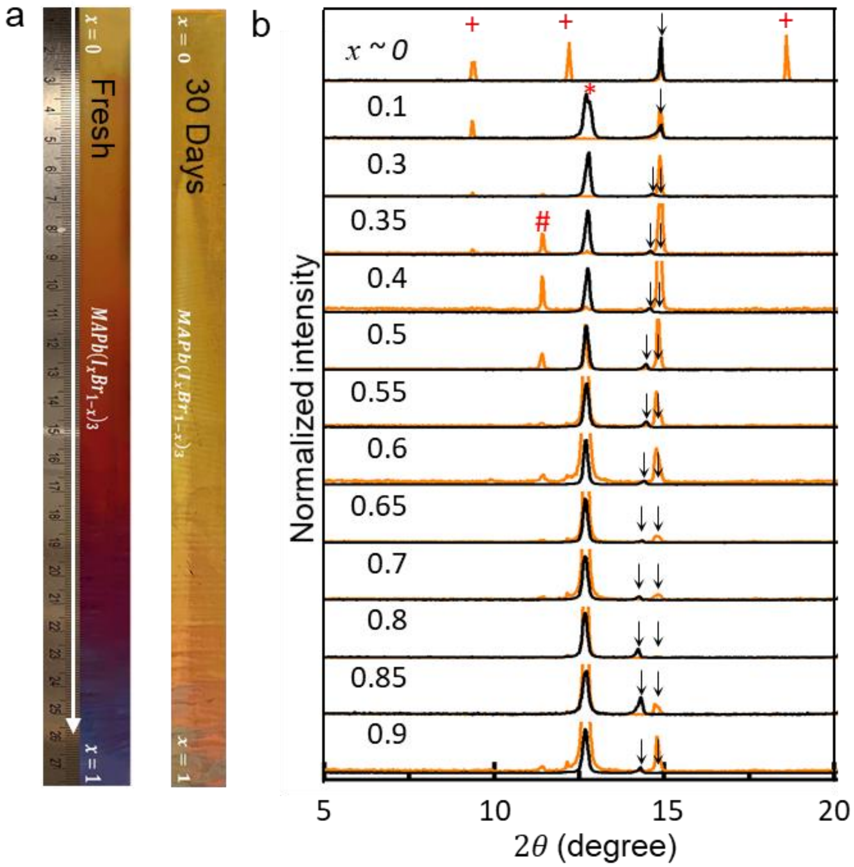

Figure 4- 3 Stability of $MAPb(I_xBr_{1-x})_3$ CGFs. **a,** Photographs of fresh and aged CGF film; **b,** mXRD spectra of fresh (black) and aged (orange) CGFs. The Bragg peaks assigned to perovskite (↓), PbI_2 (*), $MA_4PbI_6{*}2H_2O$ (#), and $MAPbBr_3$ and $PbBr_2$ hydrates (+) are labeled.

The stability of halide perovskites is the subject of ongoing investigations. Compositional engineering, including I-Br alloying, has been an efficient method of addressing this issue. Taking advantage of all possible alloys on our CGF, we used it to study the stability of perovskite alloys. We aged the perovskite CGF at 30-40% relative humidity at room temperature and regularly measured absorption, PL, and mXRD. To quantify the change by aging, we normalized the extracted values such as bandgap and lattice parameters of the aged film to those of fresh film (Supplementary Figure 4-6. a-c) in the same location. In this representation, any inclination from unity in the figures would indicate degradation. Figure. 4-3a compares fresh CGF with the aged one, demonstrating a significant visual color change in most parts of the film, except in the Br-rich region at $x < 0.2$; this agrees with optical and structural characterization results that show Br-rich regions experience the lowest degree of degradation (Supplementary Figure 4-6. a-c).

Global inspection of mXRD spectra (Figure. 4-3b) indicates three degradation regimes in $MAPb(I_xBr_{1-x})_3$ alloys as a function of composition. In the Br-rich region with $x \leq 0.1$, degradation is mainly due to hydration and formation of hydrated $PbBr_2$ and $MAPbBr_3$ (corresponding changes are shown in Figure. 4-3b)[144],[145]. In the iodide-rich region with $x \geq 0.9$, decomposition is mainly due to the loss of the MAI and significant release of PbI_2 (a sharp increase of PbI_2 peak). In $MAPb(I_xBr_{1-x})_3$ alloys with $0.1 < x < 0.9$, degradation mostly occurs through segregation to Br-rich perovskite (shift of perovskite peak to higher diffraction angles in Figure. 4-3b) and $MA_4PbI_6{*}2H_2O$ and PbI_2.[146] This, to the best of our knowledge, is the first observation of multiple degradation modes in I-Br halide perovskite alloys[147],[148].

In summary, we demonstrated a strategy for the fabrication of compositionally gradient film, a method that allows synthesizing all possible phases from binary systems in one shot. To exemplify the use of this method, we applied it to find stable regions in $MAPb(I_xBr_{1-x})_3$ compositions. This method can be used to search processing conditions and novel materials for batteries, catalysis, superconductors, and other fields, where compositional engineering plays a pivotal role. In Supplementary Figure 4-7, we show $CuBr_xCl_{1-x}$ CGF, which can be used to optimize the Cu catalyst for CO_2 electroreduction. We have future works aimed at expanding the fabrication of ternary CGFs. The approach detailed in this work provides access to the gap-free database of multinary materials enabling efficient and accurate machine-learning guided discovery of materials.

Chapter 5 High-throughput exploration of triple-cation perovskites via all-in-one compositionally-graded films

Note: This chapter has multi-author contributors, I have contributed to purposing the theory of ternary optimization, synthesizing with slot-die coating, designing the acceleration chamber for the degradation process, robotizing the characterization, measuring the samples with a spectrometer, collecting other characterization data, plotting and analyzing the graphs, fabricating perovskite solar cells, measuring the solar cell devices, collecting the MPP test results.

5-1. Abstract

Energy devices, among many others, heavily rely on combinatorial material optimization. However, new material alloys are classically developed by studying only a fraction of giant chemical space, while many intermediate compositions remain unmade in light of the lack of methods to synthesize gapless material libraries. Here we report a high-throughput experimentation strategy to synthesize ternary structures from solution with no gap in composition. We apply this strategy to make all $Cs_xMA_yFA_zPbI_3$ perovskite alloys (MA and FA stand for methylammonium and formamidinium, respectively), in less than 10 min, on a single film, on which we then study 520 unique alloys. By aging all these alloys in air supersaturated with moisture, we find a range of stable perovskites which we then use to make efficient and stable solar cells in relaxed fabrication conditions, in ambient air. This platform provides access to an unprecedented library of compositional space with no unmade alloys, and hence aids in a comprehensive accelerated discovery of materials.

5-2. Introduction

Many important technologies such as solar cells, light-emitting diodes, batteries, superconductors, and thermoelectrics rely on how fast materials are discovered or developed. Because the best materials are often a blend of multiple components, high-throughput experimentations (HTEs), [15,26,28,34,45,62,69,74,77,78,93,115,121,134,149–168] both for making and studying mixtures/alloys, have recently gained major attention[150]. However, state-of-art HTEs are unfortunately able to make only a fraction of possible compositions and then employ machine learning algorithms to extrapolate to unmade compositional space[164,166,169]. Being able to make all possible alloys would provide access to unprecedentedly large material libraries, but this remains a challenge.

One field which would benefit from HTE is halide perovskites, a family of semiconductors that offers an unusually long charge-carrier diffusion length for solution-processed materials[170–174]. Halide perovskites hence were widely researched for a range of optoelectronics. Particularly, perovskite solar cells (PSCs)[125,175–177] showed unprecedented rapid progress, in large part due to perovskite compositional engineering. For instance, the formamidinium plumboiodide ($FAPbI_3$) perovskite is an important photovoltaic absorber as it has an optimal bandgap of ~1.5 eV; but it unfortunately easily transforms to a different polymorph with an undesired large bandgap of 2.5 eV. Stabilizing $FAPbI_3$ by alloying with different cations and/or halogens led to record-breaking PSCs[178]. However, this process has hitherto relied on a fragmentary approach, when only a fraction of enormous compositional space was made and studied. It is therefore essential to develop platforms that allow making all multinary alloys, particularly due to further needs for commercially-relevant stable perovskites[151,152,167,179–185].

Here we report an approach to synthesize and characterize all possible ternary alloys from a solution in less than 10 min. We apply our approach to make $Cs_xMA_yFA_zPbI_3$ perovskite alloys on a single film, on which we then study 520 unique material compositions via a high-throughput optical characterization tool. We also study the stability of all these alloys in a high-humidity environment and find a range of ternary perovskites which remain intact under these harsh conditions. We observe the unique role of each component – organic cations aid in stabilizing perovskite structure, while an inorganic cation (cesium) – in the crystallization of pin-hole free films. We then make solar cells using perovskites from the defined humidity-stable range and test the unencapsulated devices at elevated temperatures. We further reveal three distinct degradation pathways in operational devices as a function of composition: (1) mixed-halide mixed-cation PSCs degrade by losing photocurrent and photovoltage; (2) single-halide organic-rich PSCs lose either photocurrent or photovoltage; and (3) single-halide inorganic-rich PSCs show the longest operational stability.

5-3. Results and discussion

In a cubic perovskite structure of ABX_3 composition, the lattice parameter can be extracted from two Miller planes (Figure 5-1a): from the (200) plane in which case the unit cell (a_1) is comprised of two radii of B and X; and from the (100) plane in which case the unit cell (a_2) is comprised of cathetus of the right-angle triangle whose hypotenuse is comprised of two radii of A and X. The ratio of a_2/a_1, known as Goldschmidt tolerance factor (t), should be close to unity to form a stable perovskite with no/little structural distortion.[186]

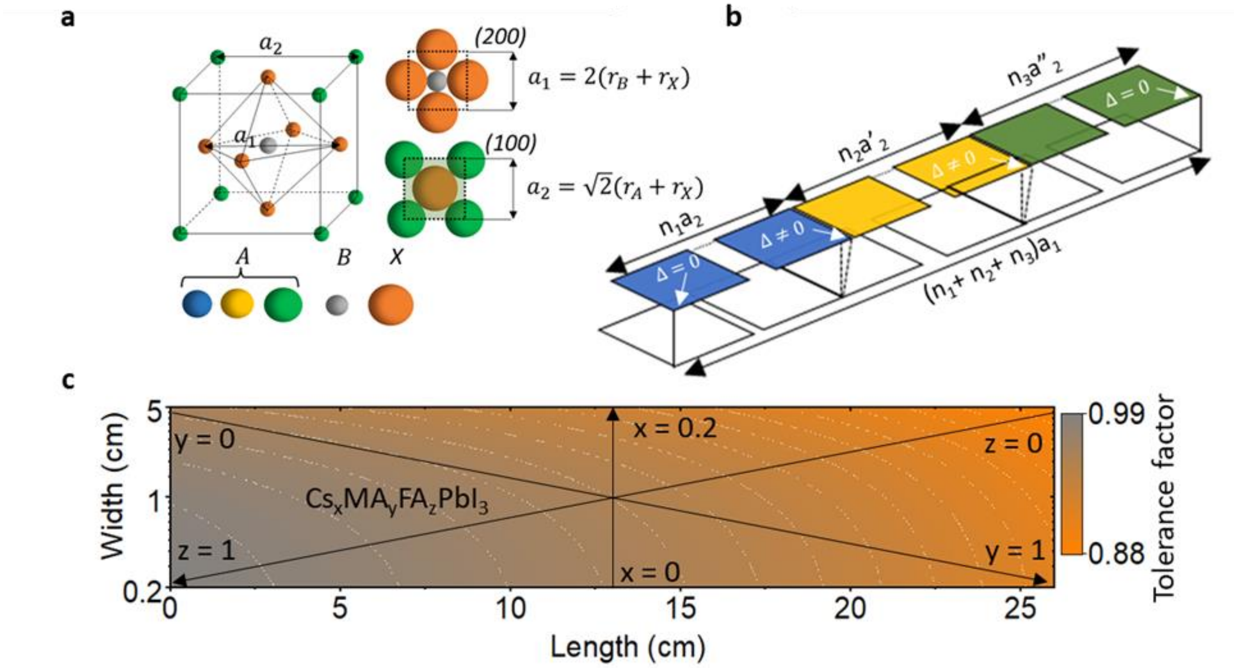

Figure 5- 1. Computing effective tolerance factor of triple cation perovskites**.** **a**, Schematic of perovskite cubic unit cell with ABX_3 composition; **b**, 1D superlattice of ABX_3 with triple A-cations showcasing accumulated offset ($\Delta = |a_2 - a_1|$); **c**, Computed effective Goldschmidt tolerance factor for triple cation perovskites for $0.88 < t_{eff} < 1$.

We applied Goldschmidt's theory to assess the structural stability of iodide triple-A-cation perovskites, $Cs_xMA_yFA_zPbI_3$, where $x+y+z=1$. Note that we did not consider mixed halides, as they are known[74], also shown below, to be prone to phase segregation. If the ternary perovskite is represented as a 1D superlattice of $N = n_1 + n_2 + n_3$ unit cells (Figure 5-1b), where n_1, n_2, and n_3 define the ratio of A-site cations ($x = n_1/N, y = n_2/N, z = n_3/N$), then the effective tolerance factor is $t_{eff} = (n_1a_2 + n_2a_2' + n_3a_2'')/Na_1$, where a_2, a_2', a_2'' are (100) lattice constants with Cs, MA, and FA, respectively (Supplementary Note 1 in appendix B). Taking $t_{eff} > 0.88$ as a criterion to form a stable cubic perovskite structure,[187] we defined the compositional range of $Cs_xMA_yFA_zPbI_3$ to be $0 < x < 0.2$, $0 < y < 1$, and $0 < z < 1$ (Figure 5-1c).

We then sought to synthesize the ternary alloys of the defined compositional range. Making them by a traditional 'fragmentary' approach would not only be time-consuming (e.g., 10^3 compositions only for 10% increments), but would also miss many intermediate compositions. We recently demonstrated a high-throughput approach to synthesize all possible binary alloys on a single thin film, which we termed compositionally-graded film (CGF)[74], *via* in-situ compositional change of deposition ink. However, our original CGF approach was limited to only binary systems.

We hence upgraded our approach to be able to achieve ternary CGF (t-CGF) by coating gradient films of three ingredients sequentially, but with varying gradient directions (Figure 5-2a). We fabricated individual graded films by slot-die coating (Supplementary Note 3 in appendix B). To achieve t-CGFs, we deposited three layers sequentially, on top of each other, with varying thicknesses to cover the entire compositional space with asymmetric combinatorial ratios (Supplementary Note 2, and Supplementary Figure 5-1 in Appendix B).

We fabricated the t-CGF on a substrate of 130 cm^2 area (5 cm width and 26 cm length). Figure 5-2b provides the detailed three-step fabrication conditions of $Cs_xMA_yFA_zPbI_3$ t-CGFs. First, $CsPbI_3$ film was deposited by a tilted slot-die head to achieve a thickness gradient across the width of the substrate (Supplementary Figures 5-2a,b). $MAPbI_3$ was then deposited on top of $CsPbI_3$ film by an *in-situ* decrease of ink concentration to achieve a thickness gradient across the length of the substrate (Supplementary Figures 5-2c,d). Finally, $FAPbI_3$ film was deposited on top of $CsPbI_3$/$MAPbI_3$ sandwich film, but its thickness gradient was opposite to $MAPbI_3$.

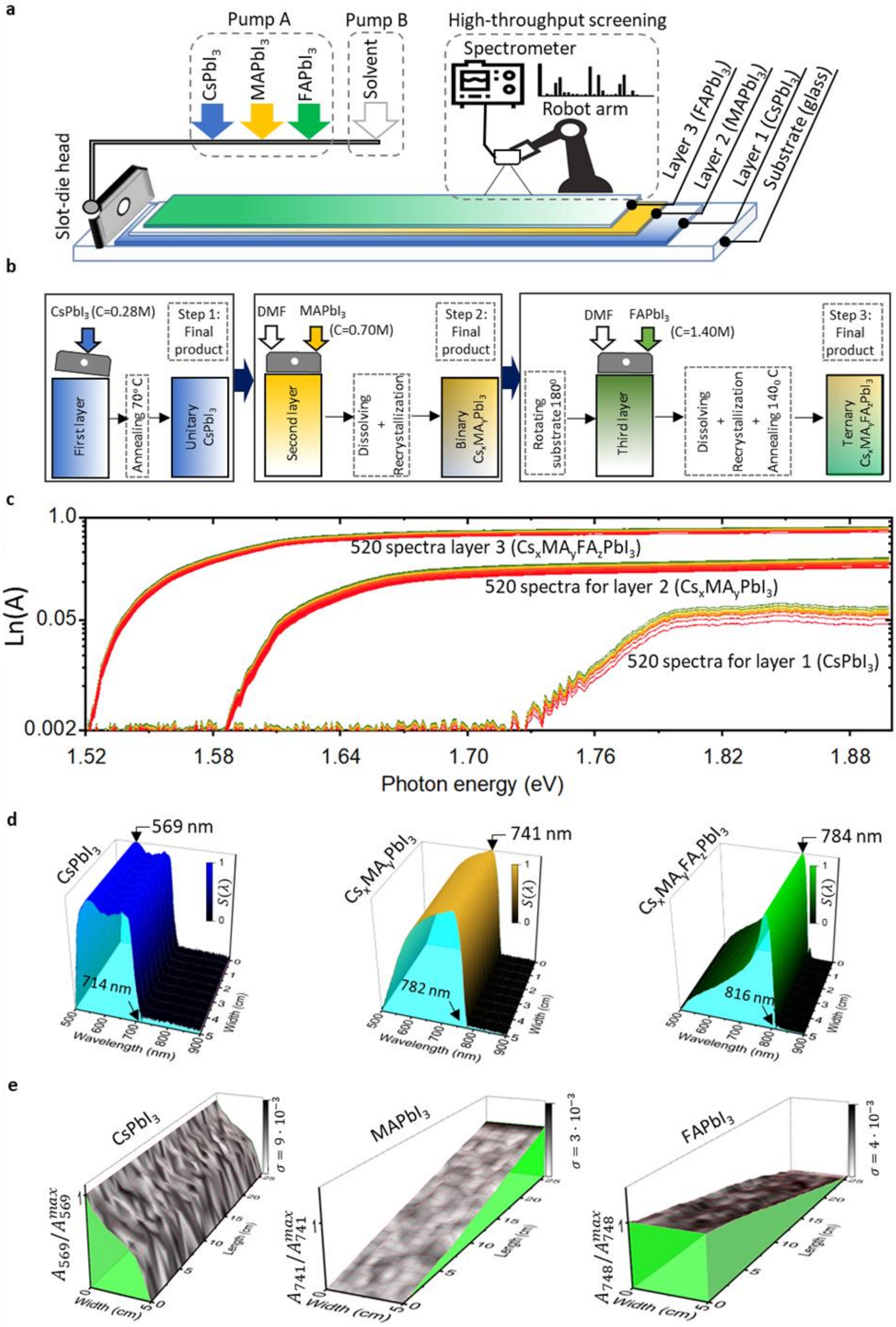
a
Pump A
Pump B
High-throughput screening
$CsPbI_3$
$MAPbI_3$
$FAPbI_3$
Solvent
Spectrometer
Robot arm
Slot-die head
Layer 3 ($FAPbI_3$)
Layer 2 ($MAPbI_3$)
Layer 1 ($CsPbI_3$)
Substrate (glass)
b
$CsPbI_3$ (C=0.28M)
Step 1: Final product
First layer
Annealing 70° C
Unitary $CsPbI_3$
DMF
$MAPbI_3$ (C=0.70M)
Step 2: Final product
Second layer
Dissolving + Recrystallization
Binary $Cs_xMA_yPbI_3$
Rotating substrate 180°
DMF
$FAPbI_3$ (C=1.40M)
Step 3: Final product
Third layer
Dissolving + Recrystallization + Annealing 140₀ C
Ternary $Cs_xMA_yFA_zPbI_3$
c
Ln(A)
1.0
0.05
0.002
520 spectra layer 3 ($Cs_xMA_yFA_zPbI_3$)
520 spectra for layer 2 ($Cs_xMA_yPbI_3$)
520 spectra for layer 1 ($CsPbI_3$)
1.52
1.58
1.64
1.70
1.76
1.82
1.88
Photon energy (eV)
d
$CsPbI_3$
569 nm
714 nm
$Cs_xMA_yPbI_3$
741 nm
782 nm
$Cs_xMA_yFA_zPbI_3$
784 nm
816 nm
$S(\lambda)$
1
0
Wavelength (nm)
500
600
700
800
900
Width (cm)
0
1
2
3
4
5
e
$CsPbI_3$
$\sigma = 9 \cdot 10^{-3}$
A_{569}/A_{569}^{max}
$MAPbI_3$
$\sigma = 3 \cdot 10^{-3}$
A_{741}/A_{741}^{max}
$FAPbI_3$
$\sigma = 4 \cdot 10^{-3}$
A_{748}/A_{748}^{max}
1
0
Width (cm)
5
Length (cm)
5
10
15
20
25

Figure 5- 2. Fabrication of $Cs_xMA_yFA_zPbI_3$ t-CGFs. **a**, Schematic of sequential deposition of three layers by slot-die coating, and robotized high-throughput screening by an optical spectrometer. **b**, Three steps of synthesizing t-CGFs; the first layer is made by a tilted slot-die head with one pump profile to form a gradient of $CsPbI_3$ across the width of the substrate; the second and third layers are deposited by the straight slot-die head with two pump profiles to deposit gradient films of $MAPbI_3$ and $FAPbI_3$, respectively, across the length of the substrate; coating of subsequent layers dissolve previous one(s) and recrystallize into new perovskite compositions. **c**, Absorption spectra after each step of fabrication. **d**, Variation of normalized absorbance as a function of wavelength across the film for three sequential layers. **e**, Normalized absorbance to global maximum showcasing gradient thickness; the gray color of the surface shows standard deviation across the film.

To assess the capability of our approach in the fabrication of thickness-graded films, we measured absorption spectra for every 0.25 cm^2 segment of the substrate, which sums up to 520 locations (130 cm^2/0.25 cm^2, i.e., 52 in length × 10 in width). We used a robotic arm and a reflection probe of a spectrometer to collect all spectra in 10 min (Supplementary Figure 5-3,). Since absorbance directly depends on the absorber's thickness (Beer-Lambert law), we used absorbance value (A) to estimate the spatial thickness of films for each deposited layer. Figure 5-2c shows the spectra for each layer at 520 locations. From the maximum variance of absorbance as a function of wavelength, $S(\lambda)$, along the t-CGF (Supplementary Note 4 in appendix B), we found the photon wavelength that exhibits the highest sensitivity to the absorber's thickness (Figure 5-2d). The $S(\lambda)$ shows a clear red-shift by adding each layer indicating successful alloying of compositions in each deposition step. We used the maximum $S(\lambda)$ value to map thickness gradience along and across the fabricated t-CGF in each step (Figure 5-2e). We indeed found that all three layers ($CsPbI_3$, $MAPbI_3$, and $FAPbI_3$) were deposited in a gradient with a low standard deviation of $\sigma < 10^{-2}$ of relative absorbance (Figure 5-2e) that guarantees alloying of all designed combinatorial ratios.

The exact composition of $Cs_xMA_yFA_zPbI_3$ in a specific location of t-CGF can be determined from its spatial coordinates (just like the coordinates can be calculated from the given composition, as discussed in Supplementary Note 1). But we sought to validate the compositional distribution of the $Cs_xMA_yFA_zPbI_3$ t-CGF by conventional analytical methods (Supplementary Note 5 in appendix B). The ratios of organic and inorganic ions, identified by NMR and EDX, from multiple locations, were in good agreement with the expected compositions (Supplementary Figures 5-4 in appendix B and figure 5). Powder XRD shows single peaks corresponding to the perovskite phase indicating the successful formation of alloys (Supplementary Figures 5-6a-c), rather than multi-layered structures in which case one would expect to observe multiple perovskite diffraction peaks. We thus conclude that each subsequent slot-die-coating dissolved the previous layers and crystallized as a new alloy:

$$CsPbI_{3(l)} \xrightarrow{1} CsPbI_{3(s)} \xrightarrow{2:\, MAPbI_{3(l)}} Cs_xMA_yPbI_{3(s)} \xrightarrow{3:\, FAPbI_{3(l)}} Cs_xMA_yFA_zPbI_{3(s)},$$

where l and s stand for the solution and solid, respectively

Powder XRD spectra show shrinkage of the crystal lattice parameters from FA-rich perovskite to Cs and MA-rich perovskites, again indicating the successful formation of ternary gradient film (Supplementary Figure 5-6e). In addition, the full-width at half maxima of XRD peaks indicate that the Cs-rich films are made of larger crystallites (Supplementary Figure 5-6d); this observation is further supported by surface SEM-images of Cs-less and Cs-containing perovskite films (Supplementary Figure 5-9).

The t-CGFs provide an unprecedented dense library to study the properties and stability of alloys, unlike conventional approaches which study only a fragment of possible compositions. We measured the bandgap and Urbach energy of $Cs_xMA_yFA_zPbI_3$ alloys at 520 locations. The bandgap, as expected, increased from ~1.50 (eV) for FA-rich perovskite to ~1.61 (eV) for MA- and Cs-rich perovskite (Supplementary Figure 5-7a). All studied $Cs_xMA_yFA_zPbI_3$ alloys, when fresh, show a relatively small Urbach energy of 20±3 meV demonstrating low energy disorder and hence can be used to make performing cells[8,188].

Figure 5-3a and 3b show the fresh t-CGF of $Cs_xMA_yFA_zPbI_3$, and the same after it was aged at 99% relative humidity for 92 days, respectively. The humidity stress discolored a major portion of the t-CGF, while only its small area remained black (Figure 5-3b). To quantify the stability of ternary alloys, we measured absorbance (Figure 5-3e) of the fresh and aged t-CGF, and then looked at the ratio of absorbance values at 784 nm: in this analysis, more deviation of this ratio from the unity means more change, or instability, of the composition. The stable range shown in Figure 5-3b, when decoded to composition (Supplementary Note 1), is made of $Cs_xMA_yFA_zPbI_3$ with $x < 0.1$; $0.1 < y < 0.25$; $0.75 < z < 0.9$ (Figure 5-3f). Supplementary Figure 5-7 shows the optoelectronic properties of the t-CGF in real space. We re-synthesized this stable range again and indeed confirmed that this combinational range remained black when exposed to identical humidity stress (Supplementary Figure 5-8).

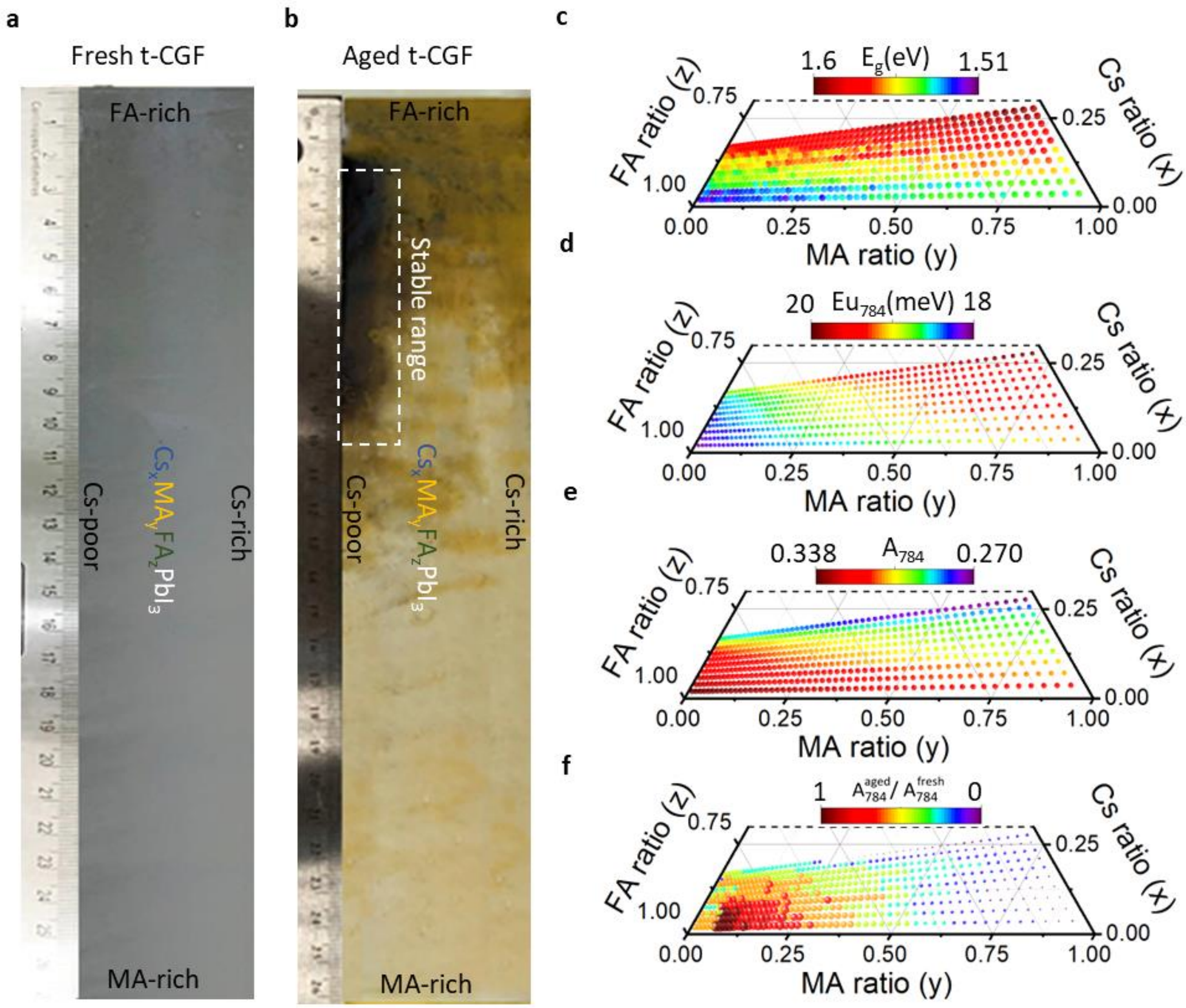

Figure 5- 3. Stability test of $Cs_xMA_yFA_zPbI_3$ t-CGF. **a**, Image of fresh t-CGF of $Cs_xMA_yFA_zPbI_3$. **b**, Image of the same t-CGF aged for 92 days under 99% relative humidity; the dashed rectangle shows perovskite compositions that experienced no/little color change. **c**, Bandgaps, **d,** Urbach energies, **e,** Absorbance values, **f,** Ratio of absorbance values of the aged to fresh at the wavelength of 784 nm for 520 locations (compositions).

Inspired by this finding of a range of stable ternary perovskites, we fabricated solar cells in a conventional architecture (Glass/ITO/SnO_2/Perovskite/Spiro-OMeTAD/Au) in ambient air. We chose three types of mono-halide perovskites from the defined stable range, which we name FA-, MA-, and Cs-rich regions (exact compositions are shown in Figure 5-4 and Supplementary Figure 5-11). Our champion device showed ~22% power conversion efficiency (Supplementary Figure 5-10a); further optimizations (e.g, device architecture, selective carrier transport materials, interface engineering), not the subject of this study, may lead to higher efficiencies. We also fabricated mixed-halide perovskite solar cells ($Cs_{0.05}MA_{0.15}FA_{0.8}PbI_{2.55}Br_{0.45}$) which, we showed recently[178], demonstrates over 500 hours of maximum power point operational stability at room temperature when encapsulated.

To study the stability of PSCs, we measured their current-voltage characteristics in ambient air at ~57% RH at 60 °C without encapsulation. These conditions represent accelerated tests by a factor of ~10^4 compared to encapsulated devices tested with no heating stress (Supplementary Figure 5-12). Mixed halide perovskites demonstrate rapid degradation of all photovoltaic figures-of-merit when tested in these conditions due to phase segregation at high temperatures (Figure 5-4a). This agrees with their rapid loss of efficiency when tested under maximum power point operation unencapsulated at 60 °C (Supplementary Figure 5-10). MA-rich perovskites experience rapid loss of J_{SC} due to the loss of MA (Figure 5-4a), while FA-rich perovskites experience a rapid loss of V_{OC} due to polymorphism of FA-rich perovskites (Figure 5-4a). Cs-containing perovskites, among all, show the least loss in all photovoltaic parameters likely due to the improved morphology of perovskites (Figure 5-4a). We further fabricated PSCs from 8 locations of the defined stable region of ternary perovskites (Supplementary Figure 5-11). Figure 5-4c, 4d, and Supplementary Figure 5-12 show the trends as a function of composition, based on which we conclude that J_{SC} loss can be minimized with the increase of FA and Cs components, while the presence of the optimum amount of MA is needed to minimize the V_{OC} loss.

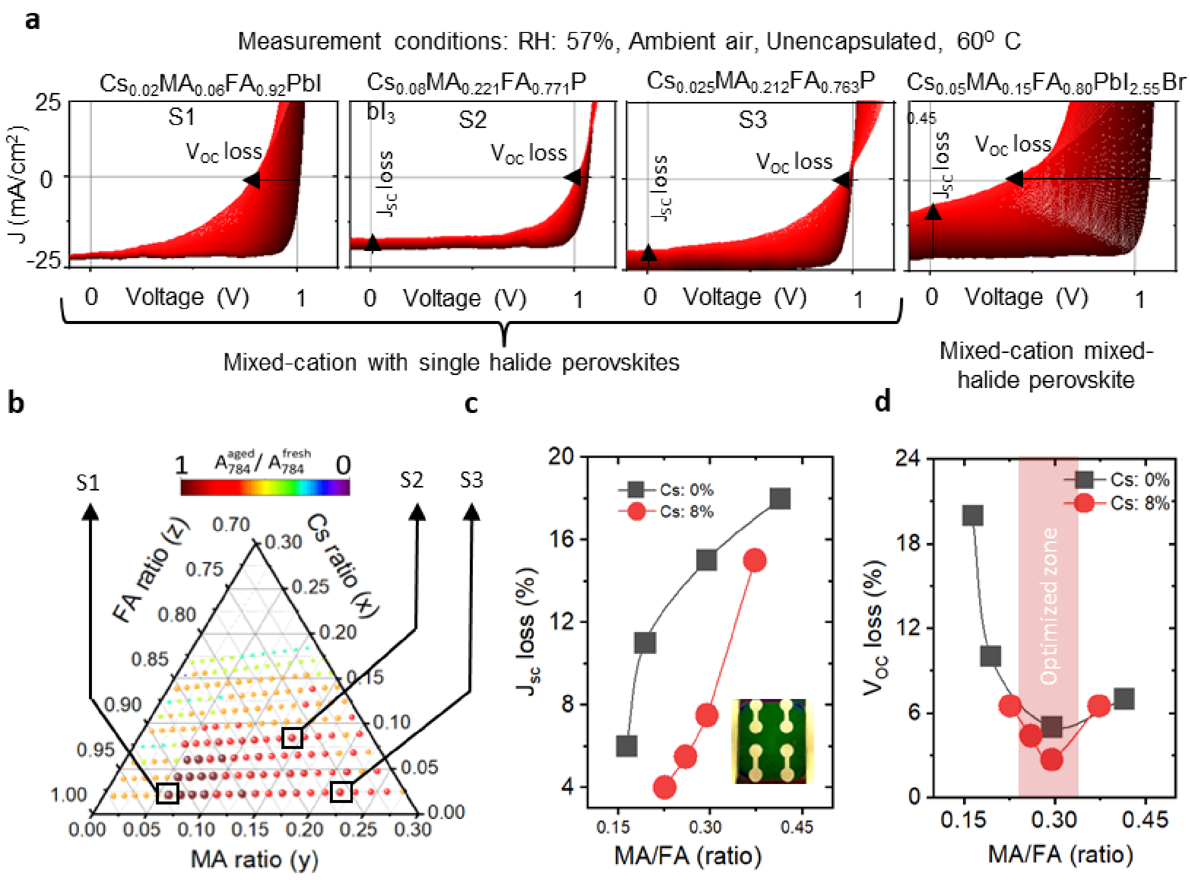

Figure 5- 4. Operational stability of ternary perovskite solar cells. **a,** Evolution of current-voltage characteristics of perovskite solar cells in ambient air at ~57% RH at 60 °C without encapsulation.

b, Selected compositions from the stable region in the ternary diagram. **c,** Loss of short circuit current density (J_{SC}), and **d,** open circuit voltage (V_{OC}) as a function of perovskite composition within ¼ h of test in ambient air at ~57% RH at 60 °C without encapsulation.

5-4. Conclusion

Compositional engineering is arguably a key knob in developing new materials. We reported a strategy for the synthesis of all possible ternary compositions. Applying our platform to halide perovskites, we reported a range of perovskite compositions that remained stable in moisture-supersaturated air and demonstrated their use in fabricating perovskite solar cells in ambient conditions. These compositions can be promising candidates for the commercialization of PSCs because they can be fabricated in relaxed conditions, and can be easily upscaled as they were made by a commercially-relevant slot-die coating method (Supplementary Figure 5-13). While we demonstrated the use of t-CGFs for a comprehensive exploration of ternary perovskites, this approach can be adopted for any other mixtures that can be solution-processed.

Chapter 6: Conclusions and outlook

6-1. Conclusions

Significant research activity enabled perovskite solar cells reach high efficiencies compared with other existing technologies. Given the fact that the maximum record efficiency of PSCs is just 1% below that of the highest efficiency silicon solar cells, the potential for commercialization of perovskite material is a likely opportunity. But challenges faced by perovskite technology make it uncertain as to if and when it can achieve gigawatt-scale deployment. In the meantime, many different applications can support higher dollar-per-watt costs and durability issues including transportation, building integrated PV, aerospace, and the Internet of Things. Sustainable growth of the perovskite industry depends on the progress in compositional optimization that is needed to adopt new perovskite composition with competitive efficiency and lifetime compared with the existing technology.

One of the key drivers pushing thin film solar cells closer to the spotlight is the possibility of easily scalable solution processing. Solar cells made from perovskite, organic, and dye-sensitized materials can be fabricated within minutes, with each layer deposited as a solution using standard methods such as slot-die coating. Printing and coating methods are well suited to roll-to-roll manufacturing and economical solar cell fabrication. The simplicity allows manufacturers a high degree of independence and the ability to carry out every step of the solar cell fabrication in-house.

Solution-based processing is an important strategy that differentiates PSCs from other PV technology that consumes intensive energy with complication in fabrication. Solution-processable devices utilize the *in-situ* synthesis of all layers at a low temperature and without vacuum equipment.

High-throughput methods are systematic and powerful platforms for conducting chemistry experiments for solving the complex problems of functional materials. Combining several compositions with various ratios results in different material properties. The synthesis of unlimited combinatorial ratios and characterizing the library is a key step in the high-throughput experiment. To achieve targeted properties required by the industry, a high-throughput platform has to be a solution-based process and close to a roll-to-roll manufacturing frame. The slot-die coating technique is a suitable platform to apply a high-throughput strategy. The current dissertation provides two unique HTS methods to optimize both binary and ternary compositions that can be considered as a robust approach toward solving the PSCs commercialization issues.

Overall, the introduced methods optimized the durability of perovskite composition and demonstrated the potential of fabricating homogeneous thin films that is essential for scaling up. Perovskite solar cells have the potential to develop into a high-efficiency, low-cost module technology for commercial power sector deployment, with throughput rates and energy payback times superior to state-of-art PV technologies. Major efforts of the research in the perovskite community are directed to increase device size, demonstrating relevant outdoor durability, and making processes robust to knock the potential of perovskite in the solar energy sector.

6-2. Future opportunities

In the continuation of the reported research, we define the following potential directions:

- Optimizing wide-bandgap for perovskite materials is one of the projects that can be conducted by utilizing the CGF approach with using $FAPbBr_3$ and $CsPbI_3$. The stabilized wide-bandgap perovskite is one of the demands for the integration of tandem solar cells with high efficiency.

- Additive and dopants with a small percentage of contribution in perovskite compositions bring new optoelectronic properties or improved morphology. The optimization of additives and dopants is in the scope of the research community, and the CGF approach can accelerate the process and provide a clear image of the material effect on the perovskite compositions.

- Quaternary and multinary compositionally-graded film that is beyond triple composition optimizations can be a complete step in the future for increasing the chemical space under exploration. The asymmetric mapping and quasi multinary in the high-throughput synthesis is an opportunity to prepare enormous combinatorial combinations in several steps to cover all chemical spaces which is a unique strategy in the history of material discovery.

The provided methods in this dissertation are not limited to the perovskite materials and can be applied to different material fields with slight changes in the setups for high-throughput experimentation. For instance, optimization of battery materials that we discussed in the fourth chapter, was used to make a family of catalysts for CO_2 reduction from binary of $CuCl_2$ and $CuBr_2$.

Appendix A:

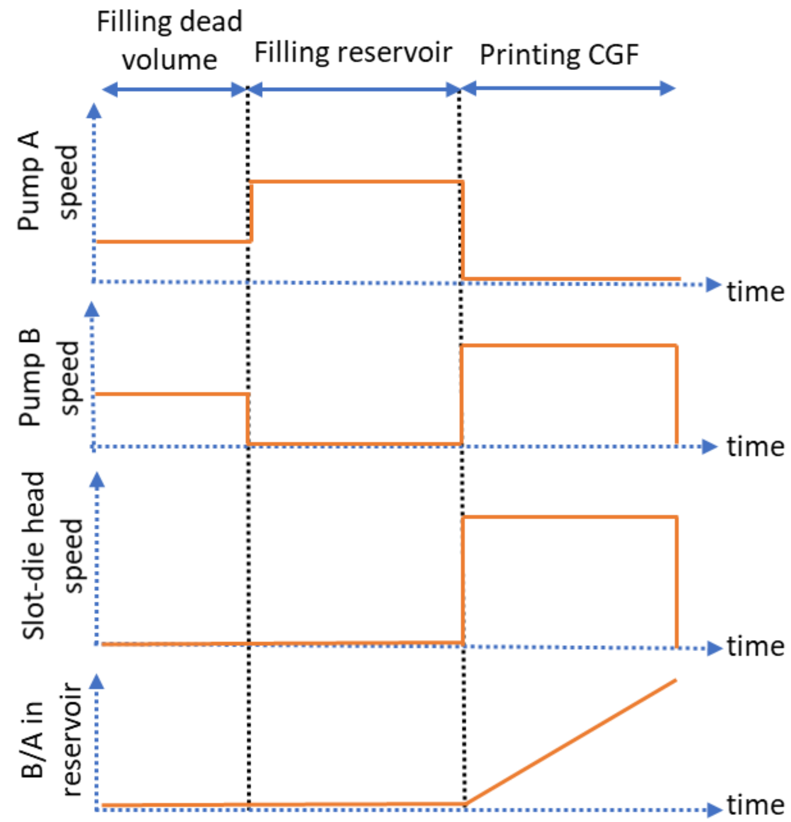

Supplementary figure 4- 1. Slot-die coating profile with alternated ink supply approach.

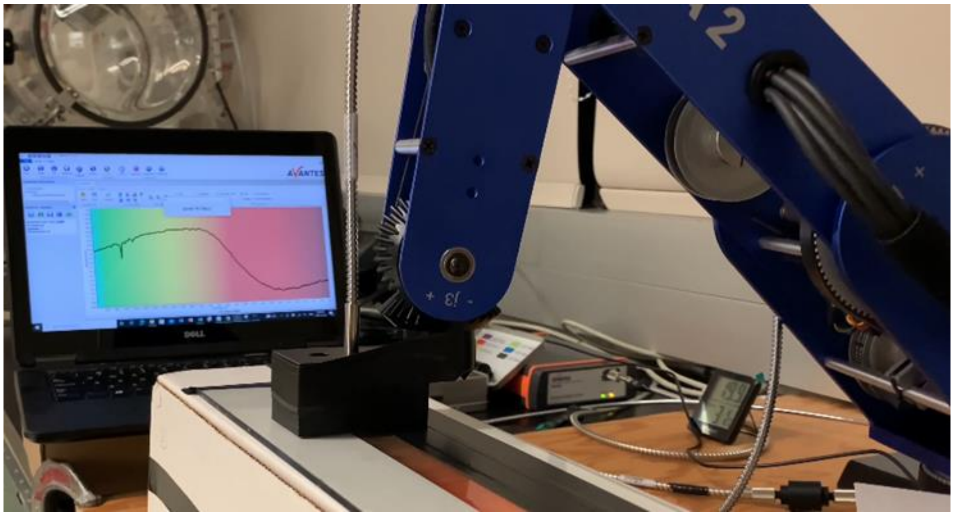

Supplementary figure 4- 2 Robotic arm for high-throughput optical characterization of compositional gradient films.

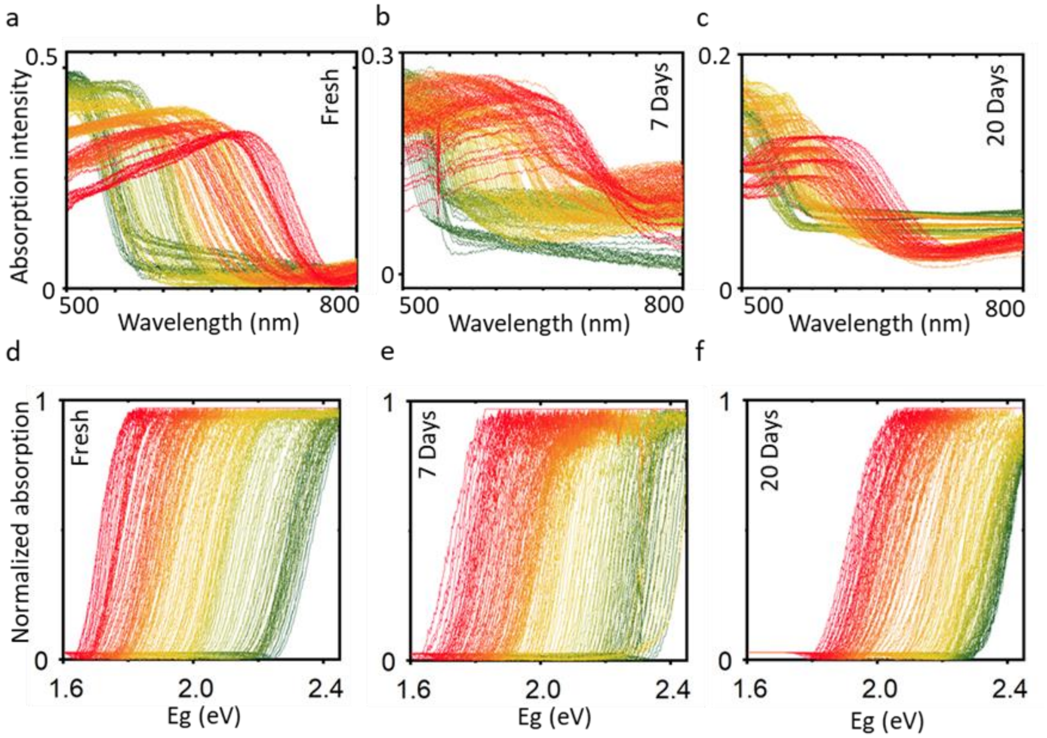

Supplementary figure 4- 3 The absorption spectra for **a,** fresh, **b,** 7-days, and **c,** 20-days aged CGFs. (**d-f**) Normalized Tauc plots for the absorption spectra of **d,** fresh, **e,** 7-days, and **f,** 20-days aged CGFs. The figure's maple color indicates the measurement data by position ranging from l=0 cm shown in green ending at l=28 cm shown in red.

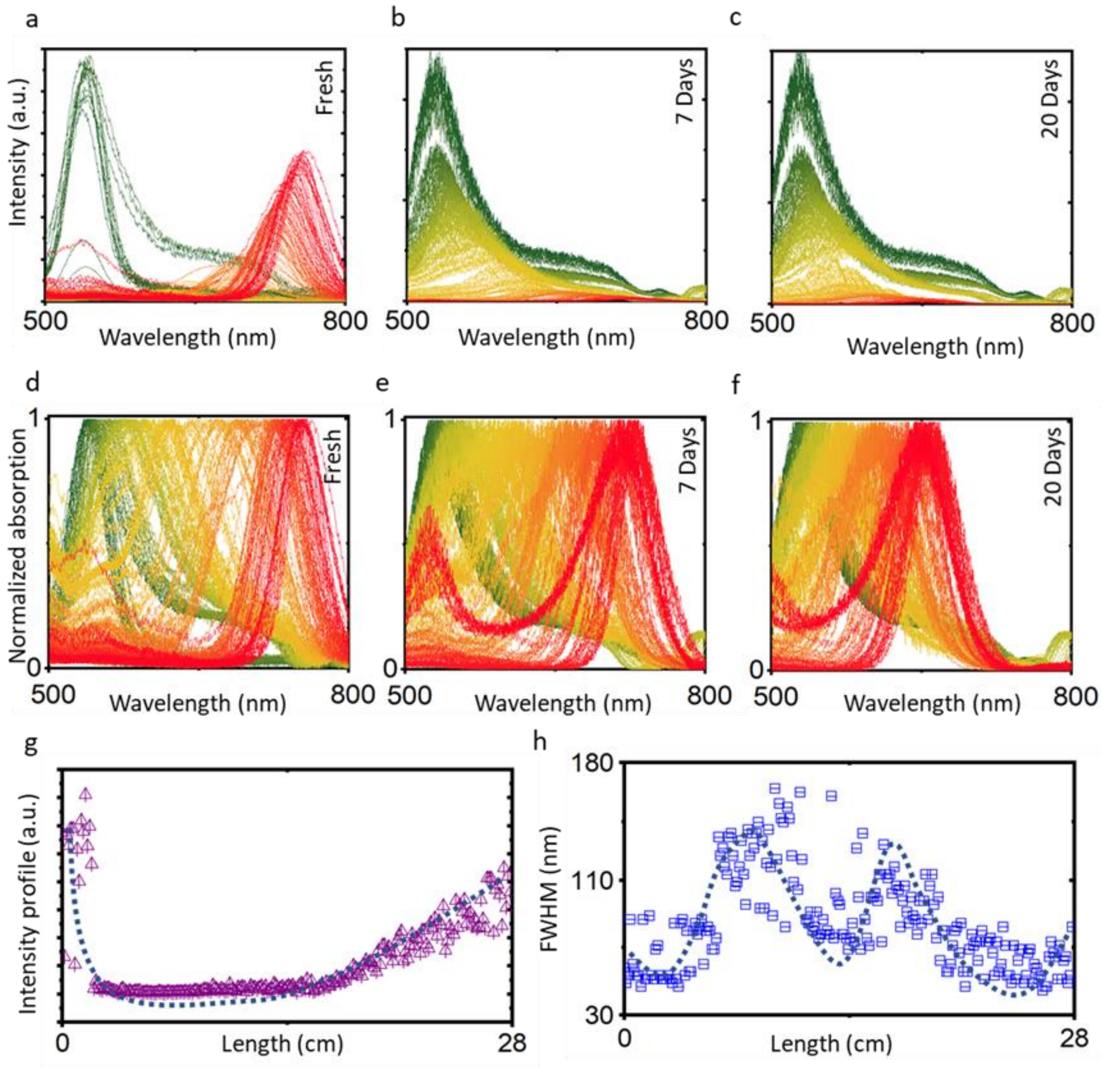

Supplementary figure 4- 4 The PL spectra for **a,** fresh, and aged after **b,** 7 days and **c,** 20 days exposing the CGF to the ambient condition. The normalized PL spectra for **d,** fresh, and aged after **e,** 7 days, and **f,** 20 days. **g,** the intensity profile of the fresh CGF with the dash-dots showing the average deviation along the CGF; h) the full-width-half-maximum (FWHM) of the peaks for fresh CGF with the dash-dots showing the average deviation along the CGF.

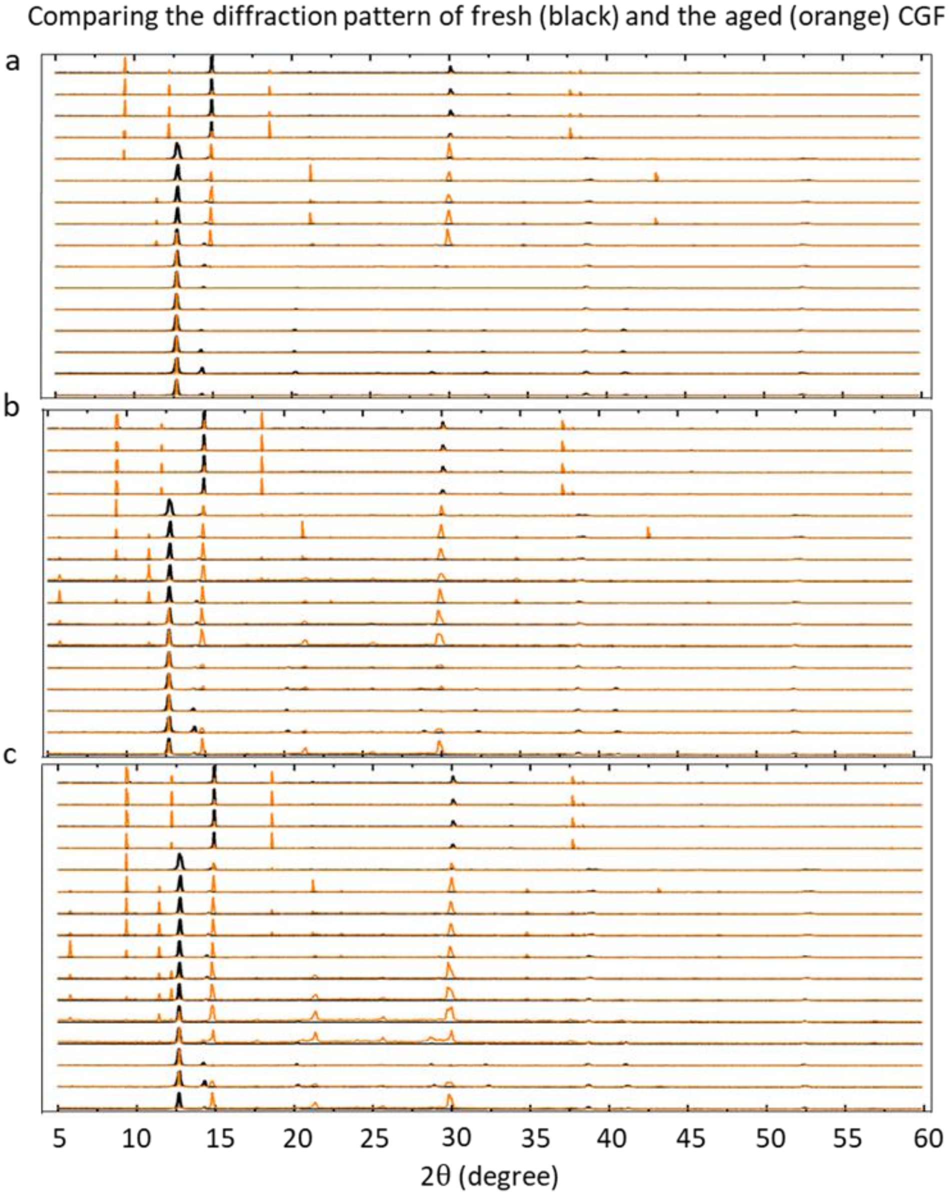

Supplementary figure 4- 5 Comparing the mXRD spectra of fresh (black) CGF vs. **a,** 10-days aged (orange), **b,** 20-days aged (orange), and **c,** 30-days aged (orange) CGF.

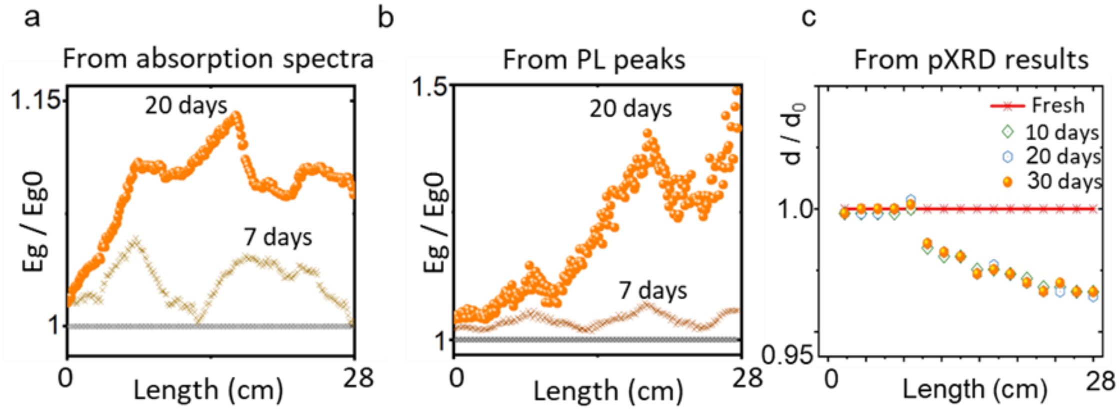

Supplementary figure 4- 6 Stability of CGF by normalizing **a,** computed bandgaps from measuring absorption spectra of aged films over the fresh one; **b,** computed bandgaps from measuring photoluminescence spectra of aged films over the fresh one; **c,** computed lattice parameters from measuring pXRD peaks over the fresh one.

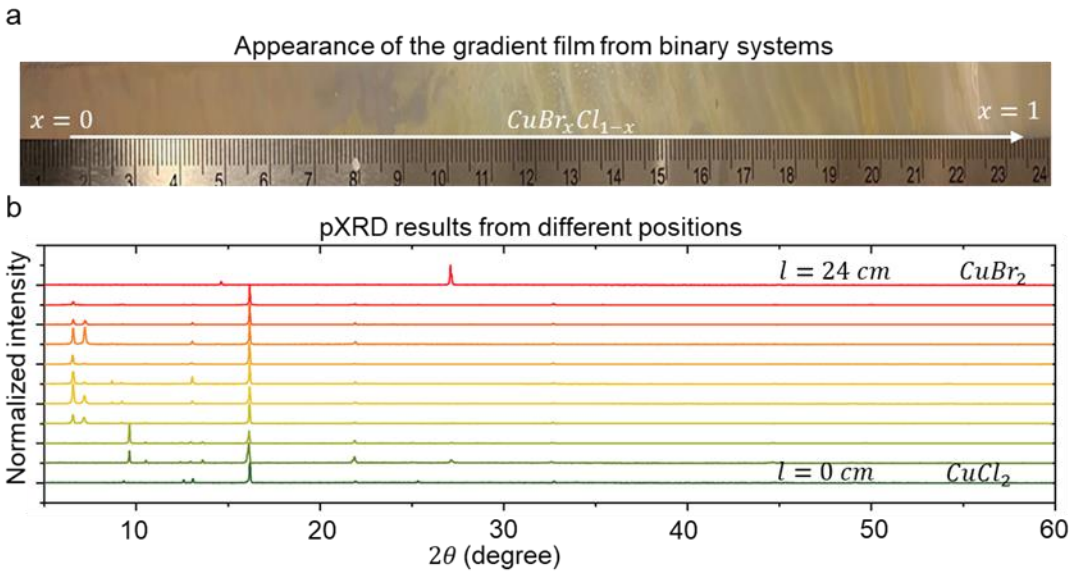

Supplementary figure 4- 7 $CuBr_xCl_{1-x}$ CGF and its corresponding mXRD spectra.

Appendic B:

Supplementary Note 1. Effective tolerance factor

Here we derive the effective tolerance factor for a superlattice possessing triple cations with three different lattice constants: r_A, r_B, and r_X are the radii of A, B, and X sites, respectively, of the ABX_3 composition. The lattice constant estimated in (100) and (200) planes, shown in Figure 5-1a, are $a_1 = 2(r_X+r_B)$ and $a_2 = \sqrt{2}(r_A+r_X)$, respectively. The tolerance factor is then

$$t = a_2 / a_1 \tag{1}$$

The lattice constant for the (100) plane can vary due to dissimilar ionic radii of A in triple-cation perovskite (a_2, $a_2^{'}$, and $a_2^{''}$).

Assuming a rectangular mapping area of $w = 5$ (cm) and $l = 26$ (cm), we normalize the positions in two dimensions (e.g., $x_i = [0; 26]$ and $y_j = [0; 5]$) to $(X_i Y_j)$ as follow:

$$X_i = \left|1 - \frac{x_i}{l}\right| \text{ and } Y_j = \frac{y_j}{w} \text{ , } (0 \le X_i, Y_j \le 1) \tag{2}$$

The combinatorial contribution of three cations are $a, b,$ and c:

$$a = f(X_i, Y_j),\ b = g(X_i, Y_j), \text{ and } c = h(X_i, Y_j) \tag{3}$$

and the total combinatorial contribution range of triple compositions is

$$\sigma = aY_j + b|1 - X_i| + cX_i; \qquad (\sigma = 1) \tag{4}$$

in which a, b, and c are the maximum combinatorial contribution ranges of each cation, respectively. For full ternary combinatorial composition, the maximum values of $a, b,$ and c are 1. For a quasi-ternary composition that considers only a limited range of contribution, the $a, b,$ and c vary based on the considered range of optimization. The first, second, and third terms in (4) are related to combinatory indices of Cs, MA, and FA, respectively. Then the optimization composition as a function of space is:

$$Cs_{a\left(\frac{Y_j}{\sigma}\right)} MA_{b\left(\frac{|1-X_i|}{\sigma}\right)} FA_{c\left(\frac{X_i}{\sigma}\right)} PbI_3 \tag{5}$$

<u>with an effective tolerance factor of:</u>

$$t_{eff} = \left[a.\left(\frac{Y_j}{\sigma}\right) a_2 + b.\left(\frac{|1-X_i|}{\sigma}\right) a_2^{'} + c.\left(\frac{X_i}{\sigma}\right) a_2^{''}\right] \Big/ \left[a_1.\left(\frac{aY_j + b.|1-X_i| + c.X_i}{\sigma}\right)\right] \tag{6}$$

Supplementary Note 2: Symmetric vs. asymmetric mapping

One of the critical steps in preparing a t-CGF is to map the position of synthesized compositions, i.e., identifying the unknown values (e.g., x, y, and z) in the $Cs_xMA_yFA_zPbI_3$ as a function of position (X and Y) in the film. The symmetric mapping approach considers a full combinatorial range of the unknown values in a composition with a linear trend in cartesian space. For example, in a binary combinatorial system, two unknown values in A_xB_y composition map x and y values in a linear manner (y = 1 – x) from 0 to 1 in two opposite gradient directions. On the other hand, an asymmetric mapping approach considers a quasi-combinatorial range in which the growth rates of unknown values are not equal in one space length. The asymmetric map enables the investigation of a large map area of one component to be dominant in the combinatorial contribution range. Supplementary Figure 5-1 shows asymmetric mapping ranges for the quasi-ternary composition of $Cs_xMA_yFA_zPbI_3$.

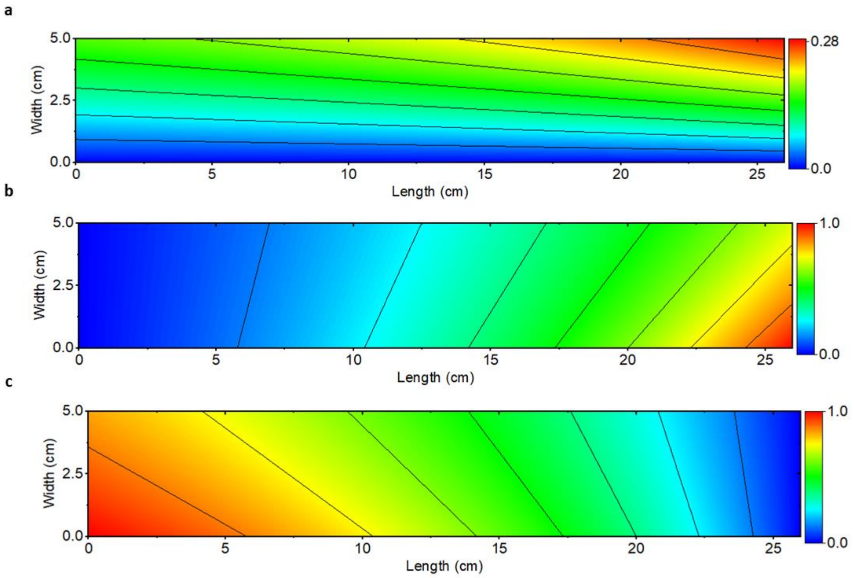

Supplementary figure 5- 1. Mapping quasi-triple composition of $Cs_xMA_yFA_zPbI_3$. **a,** $x = a\left(\frac{Y_j}{\sigma}\right)$ values in $Cs_xMA_yFA_zPbI_3$ for the maximum contribution range of Cs equal to 0.2 possessing a small area map. **b,** $y = b\left(\frac{|1-X_i|}{\sigma}\right)$ values in $Cs_xMA_yFA_zPbI_3$ for the maximum contribution range of MA equal to 0.5 possessing a moderate area map with a fast-decaying rate from left to right. **c,** $z = c\left(\frac{X_i}{\sigma}\right)$ values in $Cs_xMA_yFA_zPbI_3$ for the contribution range of FA equal to 1 possessing a large area map with a slow decaying rate.

Supplementary Note 3: Synthesizing t-CGFs with slot die coating

We used slot-die coating to fabricate compositionally gradient films. The slot-die coating was facilitated by two pumps that supply the precursors and/or solvents to the reservoir of the slot-die head. We used a PC mode controller to program the volume and speed of injecting inks and/or solvents. The gradient program enables the pumps to provide gradient pressure on syringes and thus changing the combinatorial ratio of ink to be printed on a substrate. Since the substrate is placed on a hot plate, any deposited composition is crystallized due to the quick removal of solvents. Here we used two profiles for synthesizing gradient thickness in the width and length of substrates.

To achieve a gradient thin film in width for $CsPbI_3$, we applied one pump profile of the slot-die coater (Supplementary Figure 5-2a) and tilted the slot-die head to fabricate a gradient thickness across the width of the substrate (Supplementary Figure 5-2b). This leads to a gradient thickness across the substrate.

To achieve a gradient film in length for $MAPbI_3$, we used two pump profiles (Supplementary Figure 5-2c). We filled the reservoir of the slot-die head with $MAPbI_3$ and halted it during the deposition and instead supplied solvent from another pump to dilute the ink in situ. $FAPbI_3$ was deposited in the same way but in an opposite gradient direction.

Generally, we measured the time needed to fill the reservoir from pump A to calculate the optimized speed of pump B for considerable dilution of the stored perovskite ink. We set a pre-annealing temperature of 70 ºC for the two first layers to keep the gradient map of thickness constant for the next steps, and the last layer is deposited at 140 ºC.

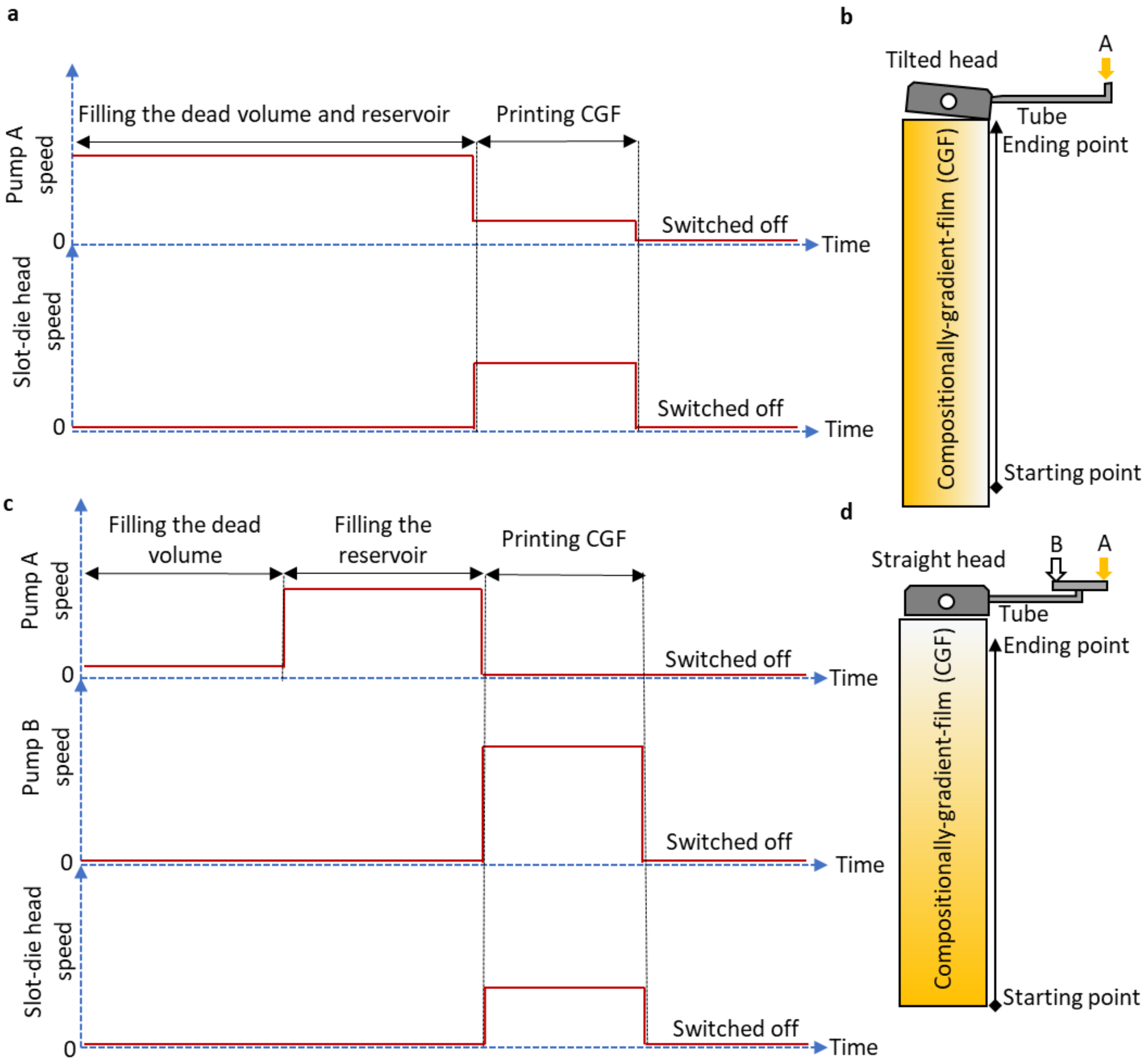

Supplementary figure 5- 2. Slot-die coating profiles and the schematics of two different setups. **a,** One-pump profile: Filling the reservoir of the head with $CsPbI_3$ while the speed of the head is zero, and supplying the head with the same ink and a proper speed of pumping while the head is moving **b,** The setup for achieving gradient in width: A tilted head setup supplied from one pump. **c,** Two-pump profile: Filling the reservoir of the head with a perovskite ink while the speed of the head is zero and supplying the head with a proper solvent and a calculated speed. **d,** The setup for achieving gradient thickness in length: A straight head setup supplied from two pumps to dilute the filled ink by solvent while the head is moving along the substrate.

Supplementary Note 4: High-throughput data-analysis

After slot-die coating of each layer, we conducted high-throughput screening using absorbance (A) at 520 locations to quantify the trend of combinatorial ratios. First, we normalized the measured absorption spectra and calculated the variance of $S(\lambda) = A_{r\text{-max}} - A_{r\text{-min}}$ for 10 lines of measurement as a function of wavelength. Then we plotted all $S(\lambda)$ for quantifying the sensitivity of spectra on the thickness of the deposited thin film.

The first set of data is collected from the first layer of depositing $CsPbI_3$ which exhibits a broader range of sensitivity.

We also plotted the local quantification map as shown in the second set of analyses shown in Figure 5-2e for validating the quality of t-CGF layers[74]. We picked the maximum $S(\lambda)$ to normalize all Absorbance values of that specific wavelength in 10 measured lines to the maximum corresponding value. We mapped the results in height to demonstrate the linearity of the gradient deposition direction. Similarly, we normalized the absorbance values (A) of the datasets to the average values across the width of deposition.

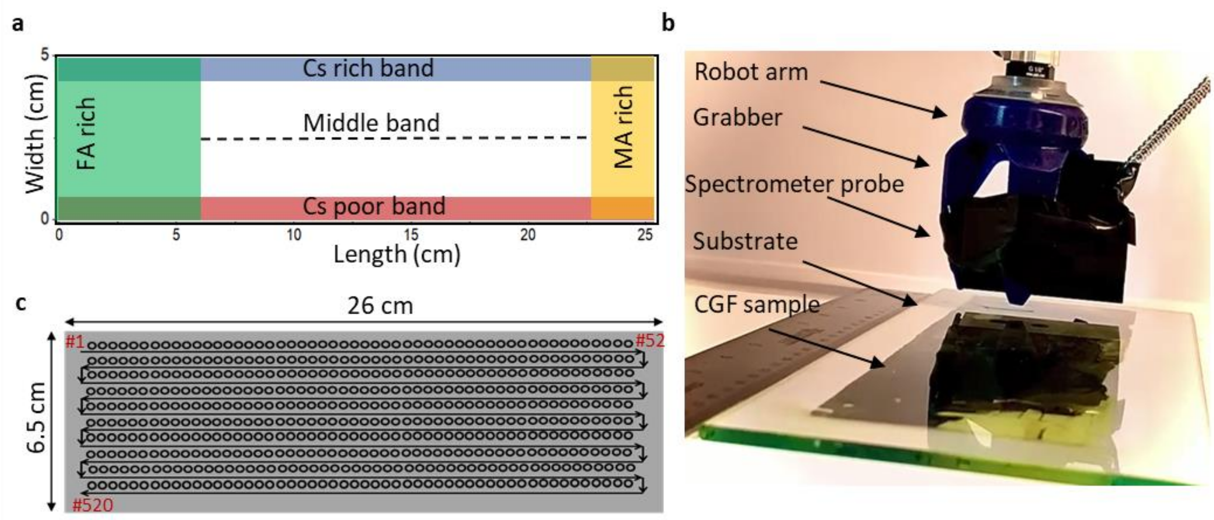

Supplementary figure 5- 3. High-throughput screening of the ternary t-CGF. **a,** High-throughput map of two opposite CGFs through the length with $FAPbI_3$, $MAPbI_3$, and one t-CGF across the width from the top; **b,** Details of robotized measurement via robot arm grabbing the probe of the spectrometer and positioning on top of the t-CGF sample; **c,** High-throughput measurement path for screening the ternary t-CGF via robot arm.

Supplementary Note 5: Validating the synthesized library

After synthesizing all compositionally gradient films in a t-CGF, we characterized them with different techniques for validating the designed chemical space.

First, we used NMR to explore the ratio of organic cations (e.g., MA and FA) through the length since their gradient ratio is designed to change in length. Supplementary Figure 5-4a shows the results of NMR spectra in four positions. The varying peaks at different ppm values of NMR measured results (supplementary figure 5-4a) are interpreted and Supplementary Figure 5-4a shows ratios of organic compounds with different values of FA over MA through the given real space. Supplementary Figure 5-4b compares the designed and measured data and shows good agreement between those.

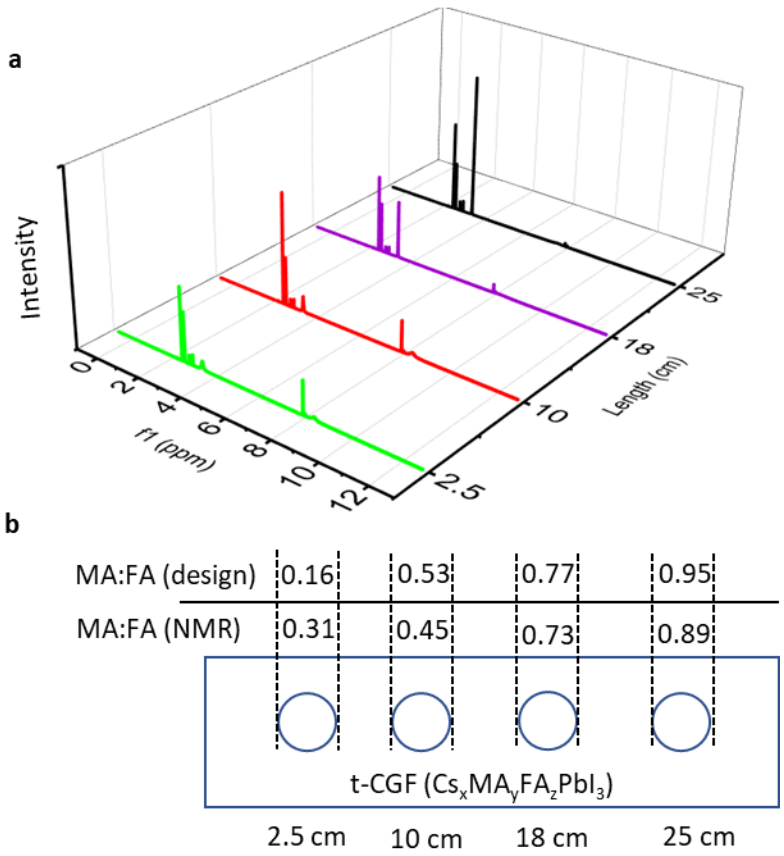

Supplementary figure 5- 4. Validating organic compound ratios along the t-CGF via NMR. **a,** Normalized raw NMR data; **b,** the comparison of designed/experiment ratios of MA over FA through the t-CGF in four spots.

We also used EDX to confirm the variation of cesium, lead, and iodine. We prepared samples from three regions across the width of the t-CGF. Supplementary Figure 5-5 shows the average values with the error bars for three compounds including Cs (left), Pb (middle), and I (right) at 1 (cm), 2.5 (cm), and 4 (cm). The average atomic numbers show the overall ingredient compound of the samples. The results from EDX validate the dominant variation of only the Cs compound across the width of the t-CGF and being constant for the two other compounds as we designed.

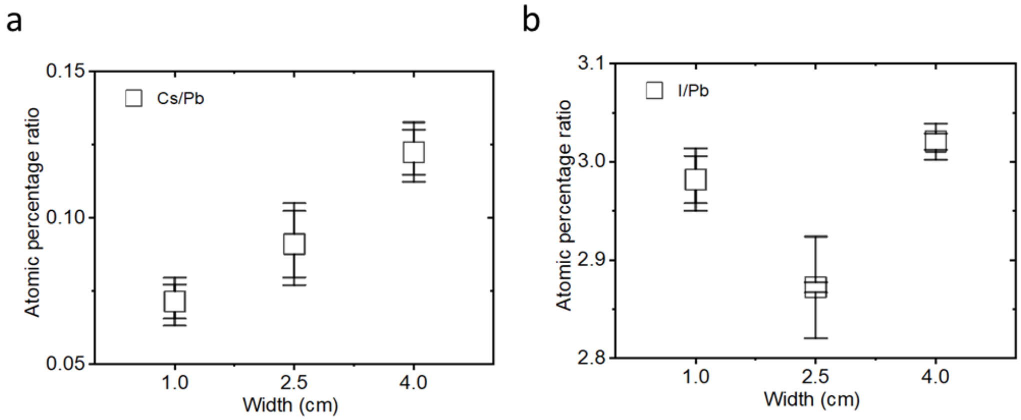

Supplementary figure 5- 5. Quantifying gradient deposition by measuring the content of atoms across the width of the t-CGF via EDX. **a,** Cesium (Cs) over lead (Pb). **b,** Iodine (I) over lead (Pb).

Lastly, we used pXRD to identify grain size and lattice parameters. We divided the prepared ternary library into two bands with 4 samples starting from the FA-rich region toward the MA-rich segment. We designated four color plots as blue, red, green, and orange for specifying Cs rich band, Cs poor band, FA rich region, and MA rich segment, respectively. Supplementary Figures 6a and 6b show the pXRD results for the Cs rich and Cs poor bands having PbI_2 peak around $2\theta = 12.6$ and peaks corresponding to perovskite of Miller planes of (100), (011), and (111) at around $2\theta = 14$, 19.81, and 24.29, respectively. We measured four samples in both Cs rich and poor bands at 1 (cm), 9 (cm), 17 (cm), and 25 (cm) along the fabricated ternary t-CGF. Supplementary Figure 5-5c shows the zoomed-in peaks of PbI_2 and only (100) perovskite peak to demonstrate details of the peak representing a transition in peak positioning and the variation of full-width at half-maximum of the measured pXRD results. The grain size can be also affected by fabrication factors such as annealing duration[189],[190],[191]. We used the Scherrer equation to compute the average grain sizes through the CGF[192],[189]. The analysis shows that the Cs rich band possesses a larger grain size than the Cs poor band region. Similarly, the grain size becomes bigger by reaching the MA-rich segment (Supplementary Figure 5-6).

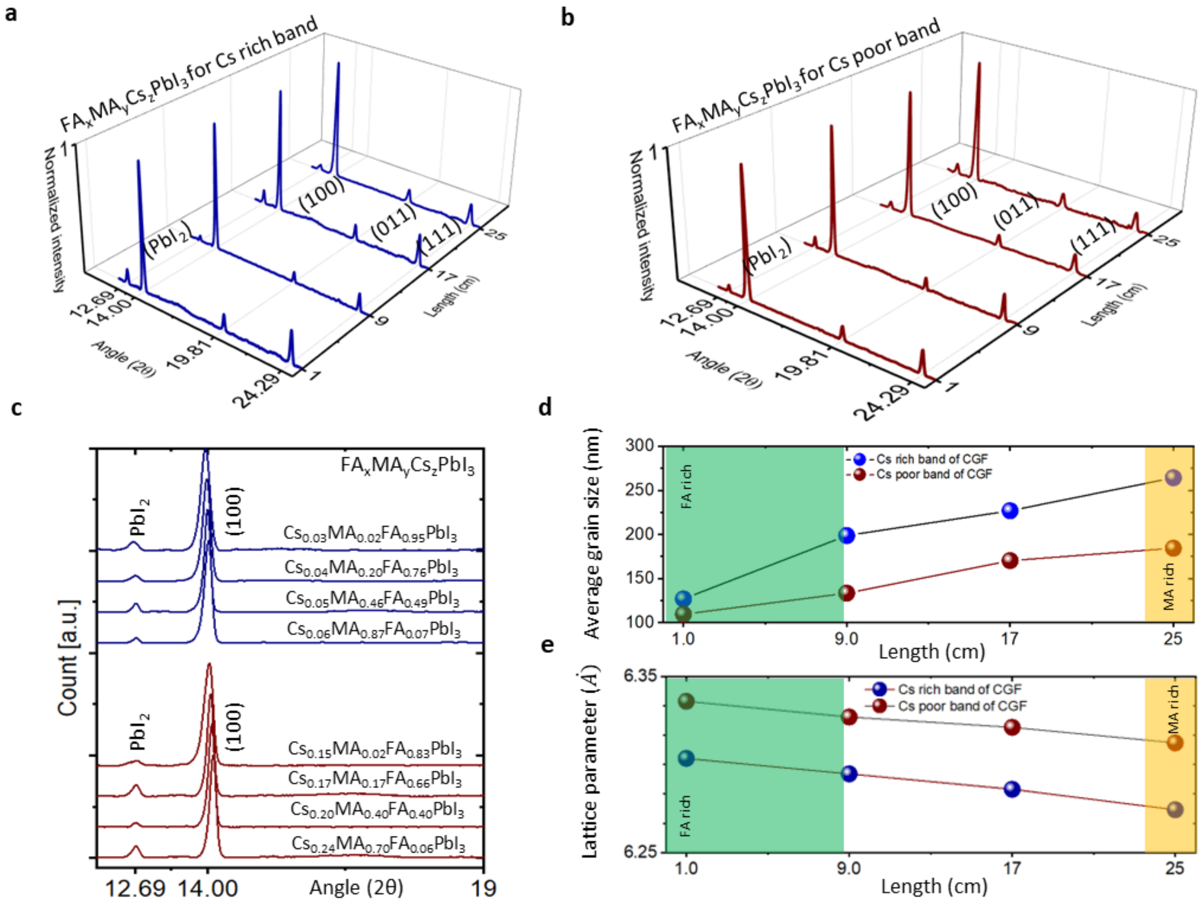

Supplementary figure 5- 6. Characterizing Cs-rich and Cs-poor bands via pXRD. **a,** Four positions from the Cs rich band of the fabricated t-CGF, **b,** Four positions from the Cs poor band of the fabricated t-CGF, **c,** Zoomed-in peaks for only (100) crystal planes of perovskite and the PbI_2 peaks to demonstrate the transition of the perovskite peak position and full-width at half-maximum. **d,** Average grain size transition through the t-CGF from FA rich segment toward the MA-rich segment for two bands. **e,** Lattice parameter transition through the t-CGF from FA rich segment toward the MA-rich segment for two bands.

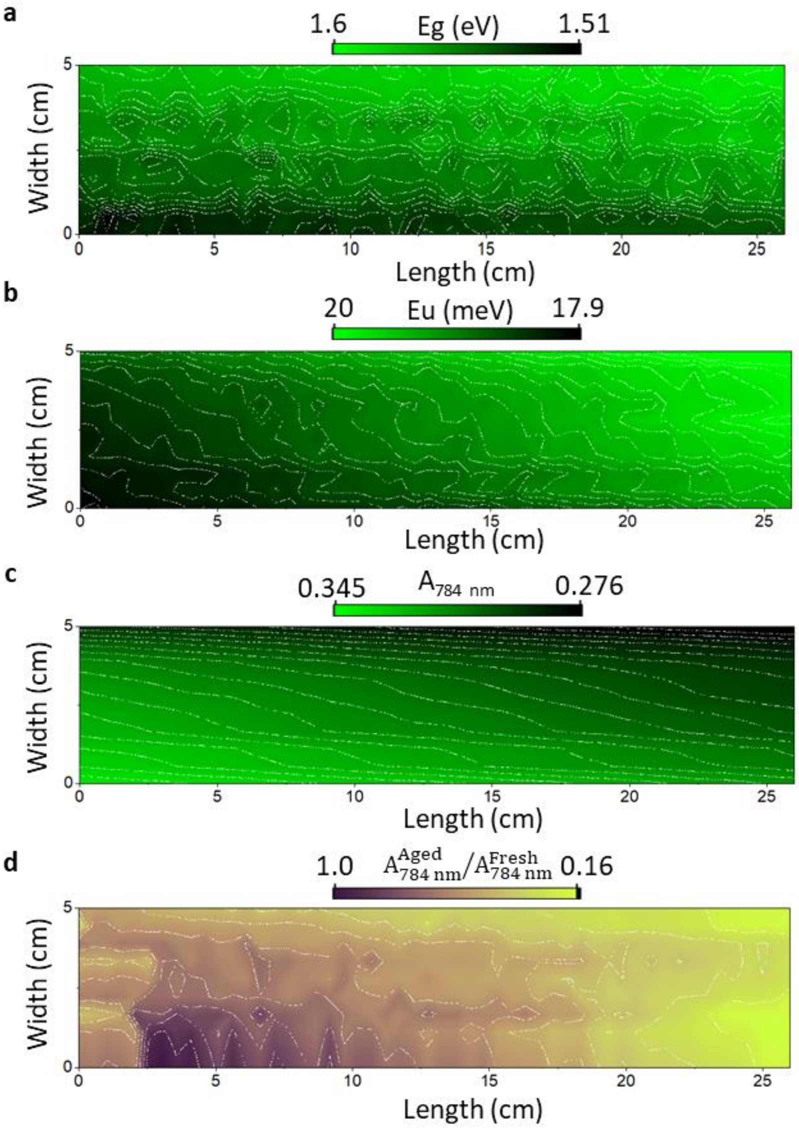

Supplementary figure 5- 7. High-throughput screening t-CGF with mapping the optoelectronic properties of 520 compositions of $Cs_xMA_yFA_zPbI_3$ on a real location. **a,** Bandgaps, **b,** Urbach energies, **c,** Absorbance values at 784 nm, **d,** The ratio of absorbance values of the aged to fresh at the wavelength of 784 nm for 520 locations (compositions).

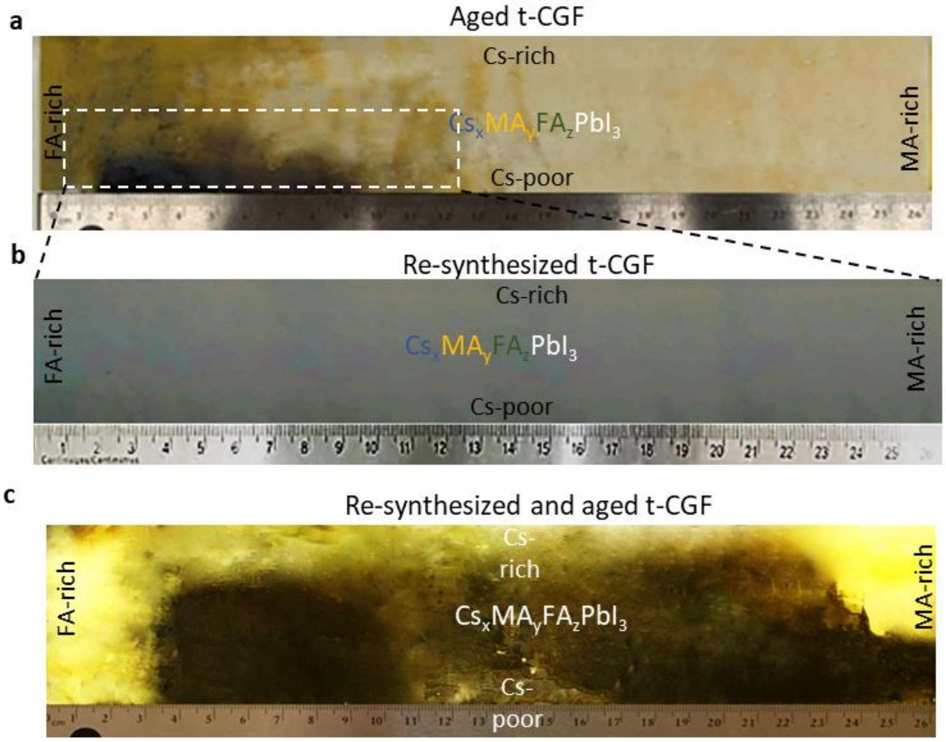

Supplementary figure 5- 8. Re-optimizing t-CGF in three steps. **a,** Aged t-CGF of the large map is of $Cs_xMA_yFA_zPbI_3$ with stable region **b,** Re-synthesizing a fresh t-CGF of the previously shown map; **c,** Aged t-CGF under 99% relative humidity for 20 days.

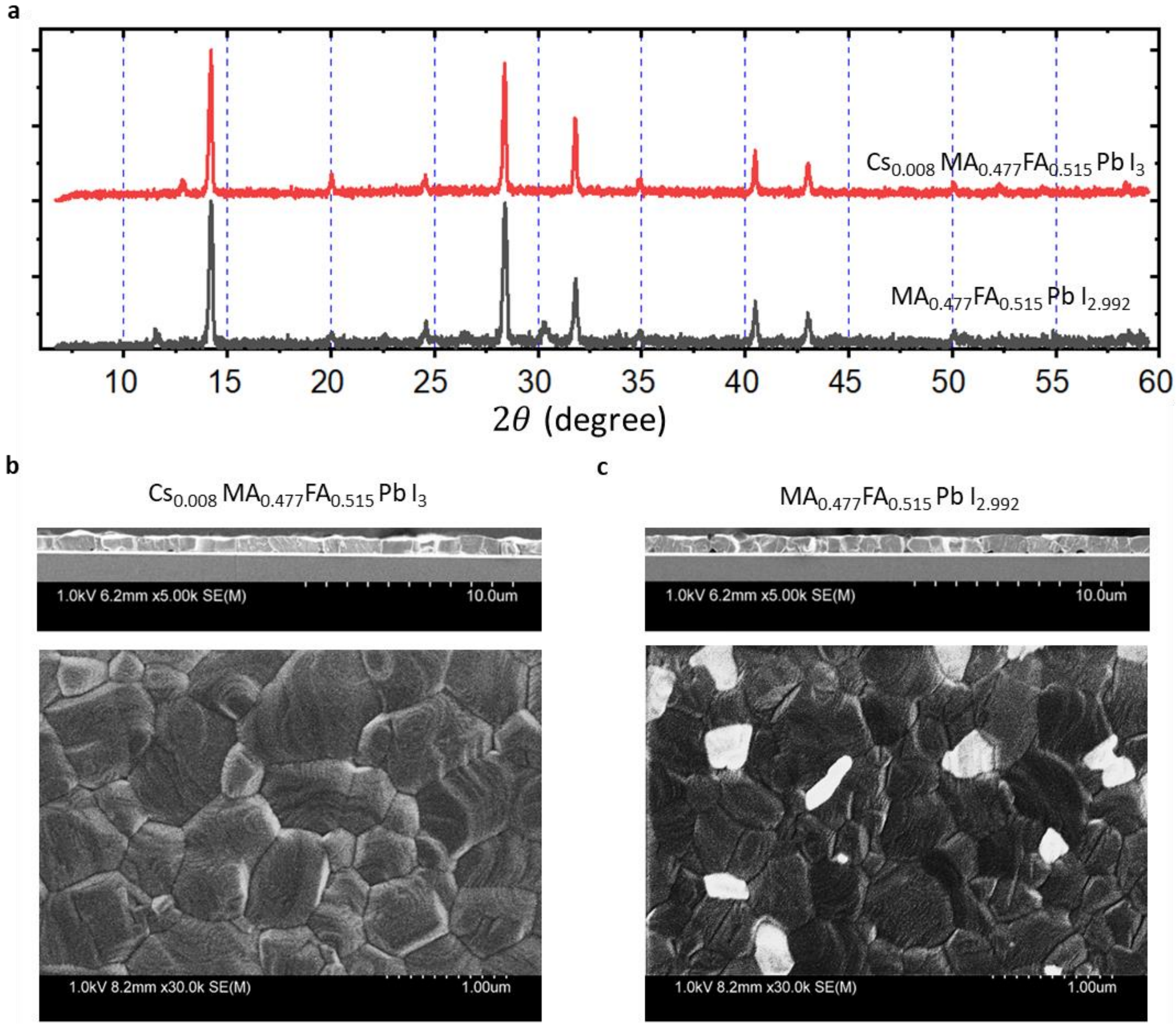

Supplementary figure 5- 9. Characterizing two compositions to analyze ternary cations on stabilization of perovskite. **a,** pXRD; **b,** SEM results for ternary perovskite showing cross-sectional view (up) and top view (bottom) **c,** SEM image of binary cation perovskite showing cross-sectional view (up) and top view (bottom).

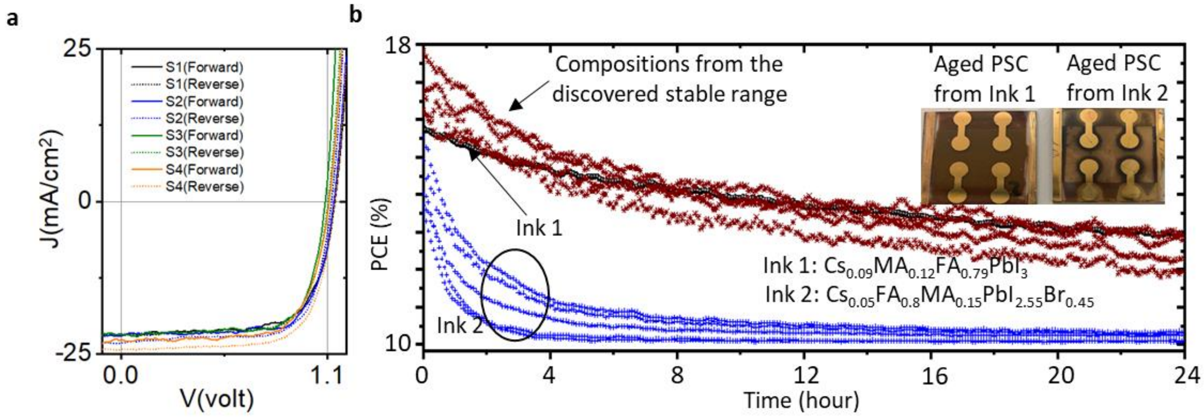

Supplementary figure 5- 10. Comparing the operational stability of two PSCs from the inks including the single-halide perovskites from the discovered ranges including ink 1: $Cs_{0.09}MA_{0.12}FA_{0.79}PbI_3$ vs. mixed-halide perovskites (ink 2: $Cs_{0.05}MA_{0.15}FA_{0.80}PbI_{2.55}Br_{0.45}$). **a,** Champion PSCs fabricated from the specified stable region in which the sample 4 (S4) has J_{SC}=-24.7 (mA/cm2), V_{OC}=1.14 volt, FF(%)=79.6, and PCE(%)=22.39 in reverse biased. **b,** The maximum power point measurement under no encapsulation and no nitrogen blowing at 45^{O} C for single-halide including ink 1 (black), the other compositions are from the discovered range reported in this article (red stars), and the mixed halide perovskite (ink 2 with blue stars); Inset: the appearances of two solar cell devices with the given compositions that are exposed to the ambient air after ~ 3 months.

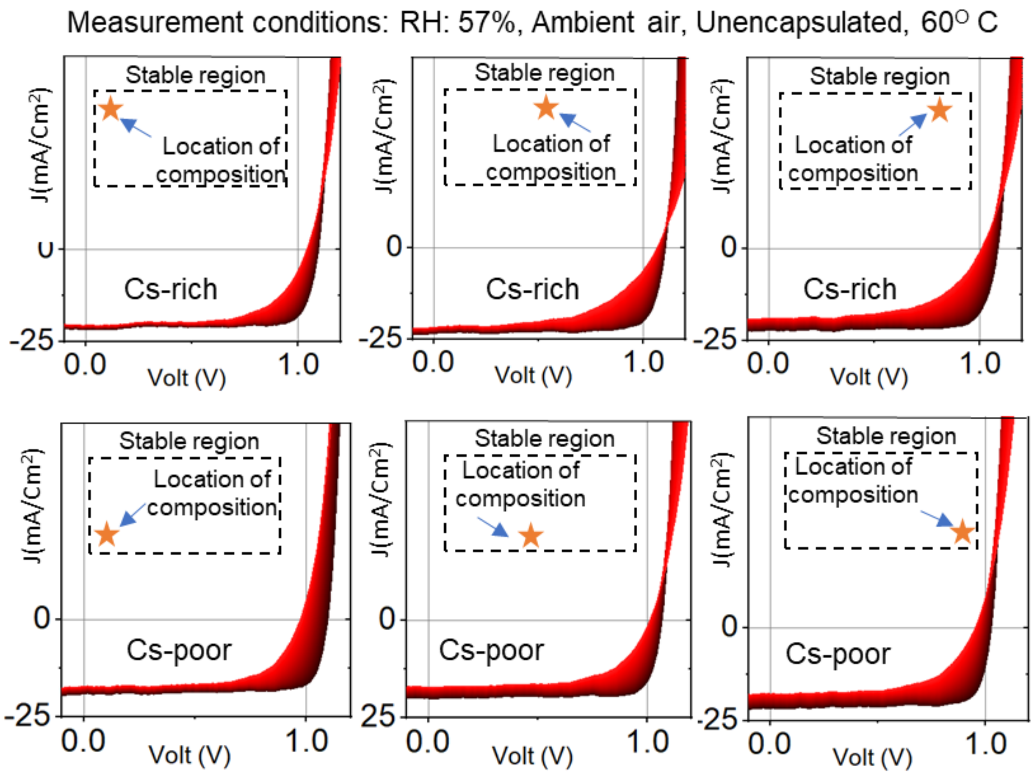

Supplementary figure 5- 11. Categorizing degradation mechanism of mixed triple cation $Cs_xMA_yFA_zPbI_3$ from the discovered region by tracking the evolution of current-voltage characteristics of perovskite solar cells in ambient air at ~57% RH at 60 °C without encapsulation. The compositions of PSCs are divided into the Cs-rich region (up), and the Cs-poor region for different MA/FA ratios (down).

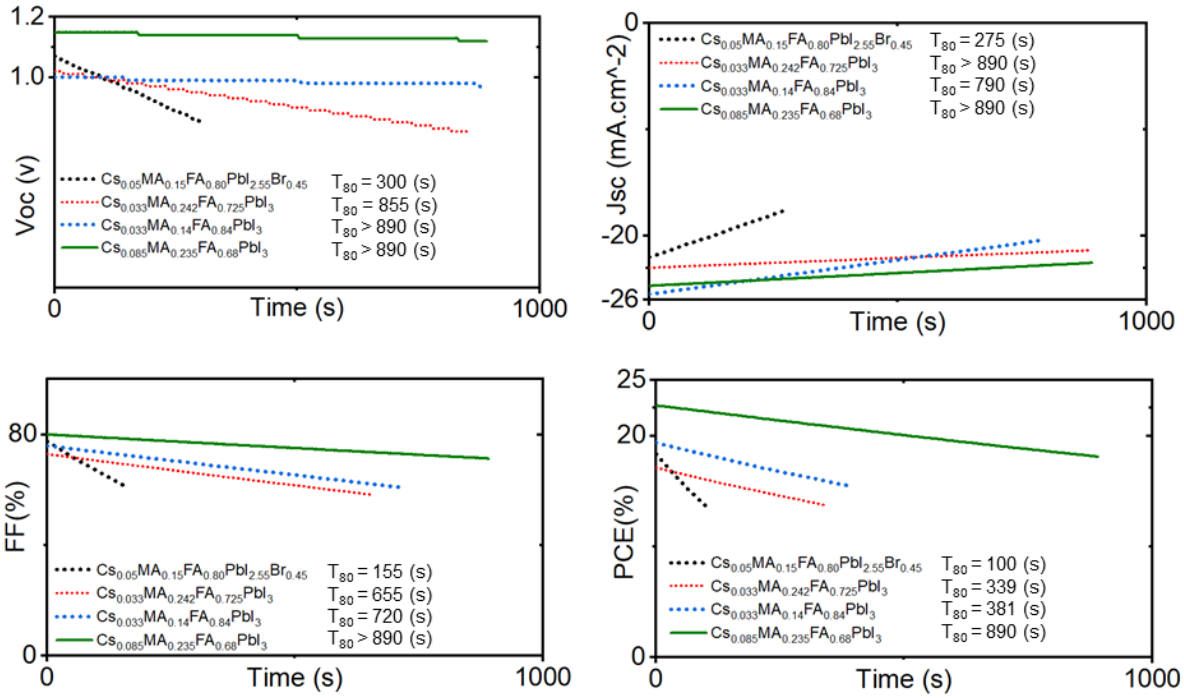

Supplementary figure 5- 12. Categorizing degradation mechanism of fixed-halide from the discovered region vs. mixed-halide perovskites under high stress (e.g., elevated temperature up to 60^{O} C, RH 57%, without sealing). The mixed-halide perovskite is reported to have at least 500 hours of stability, but exhibits only 100 (s) under the given conditions; this represents a factor of $1.8*10^4$ in accelerating the degradation.

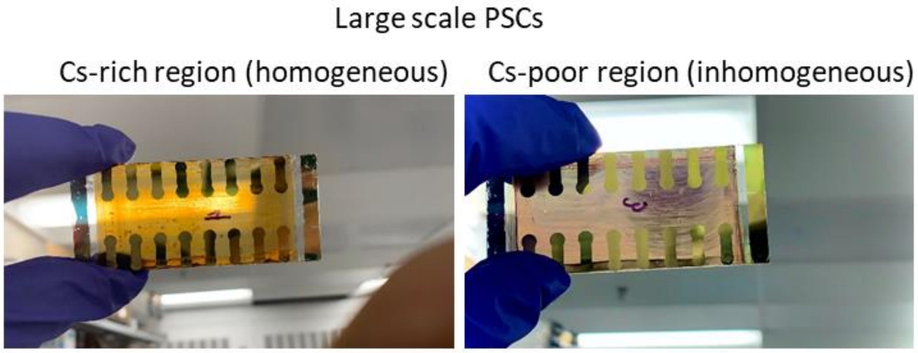
Large scale PSCs

Cs-rich region (homogeneous)

Cs-poor region (inhomogeneous)

Supplementary figure 5- 13. Comparing homogeneity of the compositions for scaling-up purposes. The fabricated large-scale PSCs with Cs-rich (left) and Cs-poor (right).

Appendix C: Publications

First-authored papers:

- Shahram Moradi, Soumya Kundu, Makhsud I. Saidaminov. "High-throughput exploration of halide perovskite compositionally-graded films and degradation mechanism". Communications Materials 3 (2022): 1-5
- Shahram Moradi, Soumya Kundu, Makhsud I. Saidaminov. "High-Throughput Synthesis of Thin Films for the Discovery of Energy Materials: A Perspective". ACS Materials Au 2 (2022): 516-524
- Shahram Moradi, Mahdi Zavvari, Yashar Zehforoosh, Armin Arashmehr, Jens Bornemann. "Eliminating excess phase accumulation in a continuous perturbed heterogeneous planar photonic crystal." Photonics and Nanostructures-Fundamentals and Applications 48 (2022): 100985.
- (Submitted) Shahram Moradi, Soumya Kundu, Muhammad Awais, Yuki Haruta, Hai-Dang Nguyen, Dongyang Zhang, Makhsud I. Saidaminov, "High-Throughput Exploration of Triple Cation Perovskites via Ternary Compositionally-Graded Films". Submitted.

Co-authored papers:

Soumya Kundu, Dongyang Zhang, Abdelrahman M Askar, Erin G Moloney, Michael M Adachi, Ayesha Nadeem, **Shahram Moradi**, Vishal Yeddu, Ahmed L Abdelhady, Oleksandr Voznyy, Makhsud I Saidaminov, "Bismuth Stabilizes the α-Phase of Formamidinium Lead Iodide Perovskite Single Crystals." ACS Materials Letters 4 (2022): 707-712.

Erin G. Moloney, Deepak Thrithamarassery Gangadharan, Vishal Yeddu, Dongyang Zhang, **Shahram Moradi**, Abdelragman M. Askar, Michael M. Adachi, David C. Leitch, and Makhsud I. Saidaminov. "Inhibition of Amine-Water Proton Exchange Stabilizes Perovskite Ink for Scalable Solar Cell Fabrication" 34.10 (2022): 4394-4402

Yanhong Wang, Jingzhi Wu, **Shahram Moradi**, Reuven Gordon, "Generating and detecting high-frequency liquid-based sound resonances with nanoplasmonics." Nano Letters 19.10 (2019): 7050-7053.

Bibliography

[1] X. Zhao, T. Liu, Q. C. Burlingame, T. Liu, R. Holley, G. Cheng, N. Yao, F. Gao, Y.-L. Loo, *Science.* **2022**, *377*, 307.

[2] M. V. Khenkin, A. K. M., I. Visoly-Fisher, Y. Galagan, F. Di Giacomo, B. R. Patil, G. Sherafatipour, V. Turkovic, H.-G. Rubahn, M. Madsen, T. Merckx, G. Uytterhoeven, J. P. A. Bastos, T. Aernouts, F. Brunetti, M. Lira-Cantu, E. A. Katz, *Energy Environ. Sci.* **2018**, *11*, 739.

[3] M. Saliba, M. Stolterfoht, C. M. Wolff, D. Neher, A. Abate, *Joule* **2018**, *2*, 1019.

[4] M. O. Reese, S. A. Gevorgyan, M. Jørgensen, E. Bundgaard, S. R. Kurtz, D. S. Ginley, D. C. Olson, M. T. Lloyd, P. Morvillo, E. A. Katz, A. Elschner, O. Haillant, T. R. Currier, V. Shrotriya, M. Hermenau, M. Riede, K. R. Kirov, G. Trimmel, T. Rath, O. Inganäs, F. Zhang, M. Andersson, K. Tvingstedt, M. Lira-Cantu, D. Laird, C. McGuiness, S. (Jimmy) Gowrisanker, M. Pannone, M. Xiao, J. Hauch, R. Steim, D. M. DeLongchamp, R. Rösch, H. Hoppe, N. Espinosa, A. Urbina, G. Yaman-Uzunoglu, J.-B. Bonekamp, A. J. J. M. van Breemen, C. Girotto, E. Voroshazi, F. C. Krebs, *Sol. Energy Mater. Sol. Cells* **2011**, *95*, 1253.

[5] Y. Cheng, L. Ding, *Energy Environ. Sci.* **2021**, *14*, 3233.

[6] M. V. Khenkin, E. A. Katz, A. Abate, G. Bardizza, J. J. Berry, C. Brabec, F. Brunetti, V. Bulović, Q. Burlingame, A. Di Carlo, R. Cheacharoen, Y.-B. Cheng, A. Colsmann, S. Cros, K. Domanski, M. Dusza, C. J. Fell, S. R. Forrest, Y. Galagan, D. Di Girolamo, M. Grätzel, A. Hagfeldt, E. von Hauff, H. Hoppe, J. Kettle, H. Köbler, M. S. Leite, S. Liu, Y.-L. Loo, J. M. Luther, C.-Q. Ma, M. Madsen, M. Manceau, M. Matheron, M. McGehee, R. Meitzner, M. K. Nazeeruddin, A. F. Nogueira, Ç. Odabaşı, A. Osherov, N.-G. Park, M. O. Reese, F. De Rossi, M. Saliba, U. S. Schubert, H. J. Snaith, S. D. Stranks, W. Tress, P. A. Troshin, V. Turkovic, S. Veenstra, I. Visoly-Fisher, A. Walsh, T. Watson, H. Xie, R. Yıldırım, S. M. Zakeeruddin, K. Zhu, M. Lira-Cantu, *Nat. Energy* **2020**, *5*, 35.

[7] "Best Research-Cell Efficiency Chart | Photovoltaic Research | NREL," can be found under https://www.nrel.gov/pv/cell-efficiency.html.

[8] S. De Wolf, J. Holovsky, S.-J. Moon, P. Löper, B. Niesen, M. Ledinsky, F.-J. Haug, J.-H. Yum, C. Ballif, *J. Phys. Chem. Lett.* **2014**, *5*, 1035.

[9] M. Saliba, T. Matsui, J.-Y. Seo, K. Domanski, J.-P. Correa-Baena, M. K. Nazeeruddin, S. M. Zakeeruddin, W. Tress, A. Abate, A. Hagfeldt, M. Grätzel, *Energy Environ. Sci.* **2016**, *9*, 1989.

[10] S. De Wolf, J. Holovsky, S.-J. Moon, P. Löper, B. Niesen, M. Ledinsky, F.-J. Haug, J.-H. Yum, C. Ballif, *J. Phys. Chem. Lett.* **2014**, *5*, 1035.

[11] X. Zheng, A. Y. Alsalloum, Y. Hou, E. H. Sargent, O. M. Bakr, *Accounts Mater. Res.* **2020**, *1*, 63.

[12] I. Chung, J.-H. Song, J. Im, J. Androulakis, C. D. Malliakas, H. Li, A. J. Freeman, J. T. Kenney, M. G. Kanatzidis, *J. Am. Chem. Soc.* **2012**, *134*, 8579.

[13] D. Shi, V. Adinolfi, R. Comin, M. Yuan, E. Alarousu, A. Buin, Y. Chen, S. Hoogland, A. Rothenberger, K. Katsiev, Y. Losovyj, X. Zhang, P. A. Dowben, O. F. Mohammed, E. H. Sargent, O. M. Bakr, *Science (80-.).* **2015**, *347*, 519.

[14] Q. Dong, Y. Fang, Y. Shao, P. Mulligan, J. Qiu, L. Cao, J. Huang, *Science (80-.).* **2015**, *347*, 967.

[15] X. Rodríguez-Martínez, E. Pascual-San-José, M. Campoy-Quiles, *Energy Environ. Sci.* **2021**, *14*, 3301.

[16] S. Lu, Q. Zhou, L. Ma, Y. Guo, J. Wang, *Small Methods* **2019**, *3*, 1900360.

[17] K. Choudhary, M. Bercx, J. Jiang, R. Pachter, D. Lamoen, F. Tavazza, *Chem. Mater.* **2019**, *31*, 5900.

[18] Z. Lu, *Mater. Reports Energy* **2021**, *1*, 100047.

[19] J. Li, K. Lim, H. Yang, Z. Ren, S. Raghavan, P. Y. Chen, T. Buonassisi, X. Wang, *Matter* **2020**, *3*, 393.

[20] T. Löffler, H. Meyer, A. Savan, P. Wilde, A. Garzón Manjón, Y.-T. Chen, E. Ventosa, C. Scheu, A. Ludwig, W. Schuhmann, T. Löffler, P. Wilde, Y. Chen, W. Schuhmann, H. Meyer, A. Savan, A. Ludwig, A. Garzón Manjón, C. Scheu, E. Ventosa, *Adv. Energy Mater.* **2018**, *8*, 1802269.

[21] A. Akinc, D. M. Lynn, D. G. Anderson, R. Langer, *J. Am. Chem. Soc.* **2003**, *125*, 5316.

[22] R. Xu, C. Nemes, K. M. Jenkins, R. A. Rourick, D. B. Kassel, C. Z. C. Liu, *J. Am. Soc. Mass Spectrom.* **2002**, *13*, 155.

[23] "Data Automation for High-Throughput Screening with Dotmatics, Tecan, and PerkinElmer Envision," can be found under https://www.tetrascience.com/blogs/data-automation-for-high-throughput-screening-hts-with-tetrascience.

[24] M.-F. Ng, J. Zhao, Q. Yan, G. J. Conduit, Z. W. Seh, *Nat. Mach. Intell.* **2020**, *2*, 161.

[25] H. Zhu, *Annu. Rev. Pharmacol. Toxicol.* **2020**, *60*, 573.

[26] S. Liang, *Comb. Chem. High Throughput Screen.* **2021**, *24*, 891.

[27] S. Sun, A. Tiihonen, F. Oviedo, Z. Liu, J. Thapa, Y. Zhao, N. T. P. Hartono, A. Goyal, T. Heumueller, C. Batali, A. Encinas, J. J. Yoo, R. Li, Z. Ren, I. M. Peters, C. J. Brabec, M. G. Bawendi, V. Stevanovic, J. Fisher, T. Buonassisi, *Matter* **2021**, *4*, 1305.

[28] R. Upadhya, S. Kosuri, M. Tamasi, T. A. Meyer, S. Atta, M. A. Webb, A. J. Gormley, *Adv. Drug Deliv. Rev.* **2021**, *171*, 1.

[29] S. Paricharak, O. Méndez-Lucio, A. Chavan Ravindranath, A. Bender, A. P. IJzerman, G. J. P. van Westen, *Brief. Bioinform.* **2016**, *19*, 105.

[30] X. D. Xiang, X. Sun, G. Briceño, Y. Lou, K. A. Wang, H. Chang, W. G. Wallace-Freedman, S. W. Chen, P. G. Schultz, *Science.* **1995**, *268*, 1738.

[31] J. Scheidtmann, P. A. Weiß, W. F. Maier, *Appl. Catal. A Gen.* **2001**, *222*, 79.

[32] X.-D. Xiang, X. Sun, G. Briceño, Y. Lou, K.-A. Wang, H. Chang, W. G. Wallace-Freedman, S.-W. Chen, P. G. Schultz, *Science.* **1995**, *268*, 1738.

[33] R. B. Merrifield, *J. Am. Chem. Soc.* **1963**, *85*, 2149.

[34] T. H. Piotrowiak, X. Wang, L. Banko, S. Kumari, S. Sarker, A. Mehta, A. Ludwig, *ACS Comb. Sci.* **2020**, *22*, 804.

[35] X. You, H. Wu, Y. Su, J. Yuan, R. Zhang, Q. Yu, M. Wu, Z. Jiang, X. Cao, *J. Mater. Chem. A* **2018**, *6*, 13191.

[36] D. Kim, H. C. Shim, T. G. Yun, S. Hyun, S. M. Han, *Extrem. Mech. Lett.* **2016**, *9*, 439.

[37] K. Kennedy, T. Stefansky, G. Davy, V. F. Zackay, E. R. Parker, *J. Appl. Phys.* **1965**, *36*, 3808.

[38] R. M. Eglen, D. H. Randle, *Assay Drug Dev. Technol.* **2015**, *13*, 262.

[39] C. W. Coley, N. S. Eyke, K. F. Jensen, *Angew. Chemie Int. Ed.* **2020**, *59*, 22858.

[40] R. M. Eglen, D. H. Randle, *Assay Drug Dev. Technol.* **2015**, *13*, 262.

[41] F. Wu, L. Zhuo, F. Wang, W. Huang, G. Hao, G. Yang, *iScience* **2020**, *23*, 101179.

[42] N. J. Jeon, J. H. Noh, W. S. Yang, Y. C. Kim, S. Ryu, J. Seo, S. Il Seok, *Nature* **2015**, *517*, 476.

[43] A. Ludwig, *npj Comput. Mater.* **2019**, *5*, 70.

[44] T. A. A. Batchelor, T. Löffler, B. Xiao, O. A. Krysiak, V. Strotkötter, J. K. Pedersen, C. M. Clausen, A. Savan, Y. Li, W. Schuhmann, J. Rossmeisl, A. Ludwig, *Angew. Chem. Int. Ed. Engl.* **2021**, *60*, 6932.

[45] D. Ulkoski, M. J. Munson, M. E. Jacobson, C. R. Palmer, C. S. Carson, A. Sabirsh, J. T. Wilson, V. R. Krishnamurthy, *ACS Appl. Bio Mater.* **2021**, *4*, 1640.

[46] A. Sánchez-Díaz, X. Rodríguez-Martínez, L. Córcoles-Guija, G. Mora-Martín, M. Campoy-Quiles, *Adv. Electron. Mater.* **2018**, *4*, 1700477.

[47] D. Tymecka, A. Misicka, in *Methods Mol. Biol.*, Methods Mol Biol. **2020**, 1, 11.

[48] J. Kirman, A. Johnston, D. A. Kuntz, M. Askerka, Y. Gao, P. Todorović, D. Ma, G. G. Privé, E. H. Sargent, *Matter* **2020**, *2*, 938.

[49] L. Lindenburg, F. Hollfelder, *Angew. Chemie Int. Ed.* **2021**, *60*, 9015.

[50] R. Ramnarayanan, B. C. Chan, M. A. Salvitti, T. E. Mallouk, F. M. Falih, J. Davis, D. B. Galloway, S. R. Bare, R. R. Willis, *J. Comb. Chem.* **2006**, *8*, 199.

[51] M. O'Huallachain, F.-A. Bava, M. Shen, C. Dallett, S. Paladugu, N. Samusik, S. Yu, R. Hussein, G. R. Hillman, S. Higgins, M. Lou, A. Trejo, L. Qin, Y. C. Tai, S. M. Kinoshita, A. Jager, D. Lashkari, Y. Goltsev, S. Ozturk, G. P. Nolan, *Commun. Biol.* **2020**, *3*, 213.

[52] M. O'Huallachain, F.-A. Bava, M. Shen, C. Dallett, S. Paladugu, N. Samusik, S. Yu, R. Hussein, G. R. Hillman, S. Higgins, M. Lou, A. Trejo, L. Qin, Y. C. Tai, S. M. Kinoshita, A. Jager, D. Lashkari, Y. Goltsev, S. Ozturk, G. P. Nolan, *Commun. Biol.* **2020**, *3*, 213.

[53] Y. Shen, M. Abolhasani, Y. Chen, L. Xie, L. Yang, C. W. Coley, M. G. Bawendi, K. F. Jensen, *Angew. Chemie* **2017**, *129*, 16551.

[54] J. Atencia, D. J. Beebe, *Nature* **2005**, *437*, 648.

[55] D. Liu, S. Cito, Y. Zhang, C.-F. Wang, T. M. Sikanen, H. A. Santos, *Adv. Mater.* **2015**, *27*, 2298.

[56] J. Puigmartí-Luis, *Chem. Soc. Rev.* **2014**, *43*, 2253.

[57] I. Lignos, S. Stavrakis, G. Nedelcu, L. Protesescu, A. J. DeMello, M. V. Kovalenko, *Nano Lett.* **2016**, *16*, 1869.

[58] B. Xin, Y. Pak, M. Shi, S. Mitra, X. Zheng, O. M. Bakr, I. S. Roqan, *Cell Reports Phys. Sci.* **2021**, *2*, 100304.

[59] W. Deng, J. Jie, X. Xu, Y. Xiao, B. Lu, X. Zhang, X. Zhang, *Adv. Mater.* **2020**, *32*, 1908340.

[60] A. Forigua, R. L. Kirsch, S. M. Willerth, K. S. Elvira, *J. Control. Release* **2021**, *333*, 258.

[61] E. B. Stephenson, K. S. Elvira, *Chem. Commun.* **2021**, *57*, 6534.

[62] Y. Zhao, J. Zhang, Z. Xu, S. Sun, S. Langner, N. T. P. Hartono, T. Heumueller, Y. Hou, J. Elia, N. Li, G. J. Matt, X. Du, W. Meng, A. Osvet, K. Zhang, T. Stubhan, Y. Feng, J. Hauch, E. H. Sargent, T. Buonassisi, C. J. Brabec, *Nat. Commun.* **2021**, *12*, 2191.

[63] K. Bozovičar, T. Bratkovič, *Int. J. Mol. Sci.* **2019**, *21*, 215.

[64] P. C. Chen, X. Liu, J. L. Hedrick, Z. Xie, S. Wang, Q. Y. Lin, M. C. Hersam, V. P. Dravid, C. A. Mirkin, *Science.* **2016**, *352*, 1565.

[65] H.-N. Barad, M. Alarcón-Correa, G. Salinas, E. Oren, F. Peter, A. Kuhn, P. Fischer, *Mater. Today* **2021**, *50*, 89.

[66] G. Liu, D. J. Eichelsdoerfer, B. Rasin, Y. Zhou, K. A. Brown, X. Liao, C. A. Mirkin, *Proc. Natl. Acad. Sci.* **2013**, *110*, 887.

[67] P.-C. Chen, G. Liu, Y. Zhou, K. A. Brown, N. Chernyak, J. L. Hedrick, S. He, Z. Xie, Q.-Y. Lin, V. P. Dravid, S. A. O'Neill-Slawecki, C. A. Mirkin, *J. Am. Chem. Soc.* **2015**, *137*, 9167.

[68] W.-J. Li, M. Tu, R. Cao, R. A. Fischer, *J. Mater. Chem. A.* **2016**, *4*, 12356.

[69] N. Kumari Jangid, S. Jadoun, N. Kaur, *Eur. Polym. J.* **2020**, *125*, 109485.

[70] S. Guerin, B. E. Hayden, *Chem. Commun. (Camb).* **2019**, *55*, 10047.

[71] R. A. Potyrailo, V. M. Mirsky, *Chem. Rev.* **2008**, *108*, 770.

[72] F. Dinic, K. Singh, T. Dong, M. Rezazadeh, Z. Wang, A. Khosrozadeh, T. Yuan, O. Voznyy, *Adv. Funct. Mater.* **2021**, *31*, 2104195.

[73] E. Reinhardt, A. M. Salaheldin, M. Distaso, D. Segets, W. Peukert, *ACS Comb. Sci.* **2020**, *22*, 6.

[74] S. Moradi, S. Kundu, M. Rezazadeh, V. Yeddu, O. Voznyy, M. I. Saidaminov, *Commun. Mater.* **2022**, *3*, 13.

[75] O. Almora, D. Baran, G. C. Bazan, C. Berger, C. I. Cabrera, K. R. Catchpole, S. Erten-Ela, F. Guo, J. Hauch, A. W. Y. Ho-Baillie, T. J. Jacobsson, R. A. J. Janssen, T. Kirchartz, N. Kopidakis, Y. Li, M. A. Loi, R. R. Lunt, X. Mathew, M. D. McGehee, J. Min, D. B. Mitzi, M. K. Nazeeruddin, J. Nelson, A. F. Nogueira, U. W. Paetzold, N. Park, B. P. Rand, U. Rau, H. J. Snaith, E. Unger, L. Vaillant-Roca, H. Yip, C. J. Brabec, *Adv. Energy Mater.* **2021**, *11*, 2102526.

[76] J. Alstrup, M. Jørgensen, A. J. Medford, F. C. Krebs, *ACS Appl. Mater. Interfaces* **2010**, *2*, 2819.

[77] X. Du, L. Lüer, T. Heumueller, J. Wagner, C. Berger, T. Osterrieder, J. Wortmann, S. Langner, U. Vongsaysy, M. Bertrand, N. Li, T. Stubhan, J. Hauch, C. J. Brabec, *Joule.* **2021**, *5*, 495.

[78] H. Näsström, O. Shargaieva, P. Becker, F. Mathies, I. Zizak, V. R. F. Schröder, E. J. W. List-Kratochvil, T. Unold, E. Unger, *J. Mater. Chem. A.* **2022**, *10*, 4906.

[79] K. Kawashima, Y. Okamoto, O. Annayev, N. Toyokura, R. Takahashi, M. Lippmaa, K. Itaka, Y. Suzuki, N. Matsuki, H. Koinuma, *Sci. Technol. Adv. Mater.* **2017**, *18*, 307.

[80] R. Meyer, K. Sliozberg, C. Khare, W. Schuhmann, A. Ludwig, *ChemSusChem.* **2015**, *8*, 1279.

[81] C. Chen, Y. Zhao, S. Lu, K. Li, Y. Li, B. Yang, W. Chen, L. Wang, D. Li, H. Deng, F. Yi, J. Tang, *Adv. Energy Mater.* **2017**, *7*, 1700866.

[82] C. M. Caskey, R. M. Richards, D. S. Ginley, A. Zakutayev, *Mater. Horiz.* **2014**, *1*, 424.

[83] P. Becker, J. A. Márquez, J. Just, A. Al-Ashouri, C. Hages, H. Hempel, M. Jošt, S. Albrecht, R. Frahm, T. Unold, *Adv. Energy Mater.* **2019**, *9*, 1900555.

[84] N. Thejo Kalyani, S. J. Dhoble, *Renew. Sustain. Energy Rev.* **2012**, *16*, 2696.

[85] J. Y. Lee, S. Y. Kim, H. J. Yoon, *Adv. Opt. Mater.* **2022**, *10*, 2101361.

[86] P. Du, J. Li, L. Wang, J. Liu, S. Li, N. Liu, Y. Li, M. Zhang, L. Gao, Y. Ma, J. Tang, *ACS Appl. Mater. Interfaces* **2019**, *11*, 47083.

[87] Z. Li, Z. Chen, Y. Yang, Q. Xue, H.-L. Yip, Y. Cao, *Nat. Commun.* **2019**, *10*, 1027.

[88] J. Li, P. Du, S. Li, J. Liu, M. Zhu, Z. Tan, M. Hu, J. Luo, D. Guo, L. Ma, Z. Nie, Y. Ma, L. Gao, G. Niu, J. Tang, *Adv. Funct. Mater.* **2019**, *29*, 1903607.

[89] L. Cheng, R. S. Assary, X. Qu, A. Jain, S. P. Ong, N. N. Rajput, K. Persson, L. A. Curtiss, *J. Phys. Chem. Lett.* **2015**, *6*, 283.

[90] C. Zhang, S.-H. Park, A. Seral-Ascaso, S. Barwich, N. McEvoy, C. S. Boland, J. N. Coleman, Y. Gogotsi, V. Nicolosi, *Nat. Commun.* **2019**, *10*, 849.

[91] A. Vahidmohammadi, A. Hadjikhani, S. Shahbazmohamadi, M. Beidaghi, *ACS Nano.* **2017**, *11*, 11135.

[92] D. Y. Oh, Y. E. Choi, D. H. Kim, Y.-G. Lee, B.-S. Kim, J. Park, H. Sohn, Y. S. Jung, *J. Mater. Chem. A.* **2016**, *4*, 10329.

[93] D. Song, X. Chen, Z. Lin, Z. Tang, W. Ma, Q. Zhang, Y. Li, X. Zhang, *ACS Nano.* **2021**, *15*, 16469.

[94] J. Heiska, M. Nisula, M. Karppinen, *J. Mater. Chem. A* **2019**, *7*, 18735.

[95] T. Adhikari, A. Hebert, M. Adamič, J. Yao, K. Potts, E. McCalla, *ACS Comb. Sci.* **2020**, *22*, 311.

[96] M. R. Roberts, G. Vitins, J. R. Owen, *J. Power Sources* **2008**, *179*, 754.

[97] M. Qin, Z. Lin, Z. Wei, B. Zhu, J. Yuan, I. Takeuchi, K. Jin, *Chinese Phys. B* **2018**, *27*, 127402.

[98] S. W. Fackler, V. Alexandrakis, D. König, A. G. Kusne, T. Gao, M. J. Kramer, D. Stasak, K. Lopez, B. Zayac, A. Mehta, A. Ludwig, I. Takeuchi, *Sci. Technol. Adv. Mater.* **2017**, *18*, 231.

[99] J. J. Hanak, *J. Mater. Sci.* **1970**, *5*, 964.

[100] M. Saadat, A. E. George, K. C. Hewitt, *Phys. C Supercond. its Appl.* **2010**, *470*, S59.

[101] B. J. Taylor, T. H. Emery, A. M. Leese de Escobar, I. Jeon, M. B. Maple, *IEEE Trans. Appl. Supercond.* **2017**, *27*, 1.

[102] B. J. Taylor, C. A. McElroy, I. K. Lum, A. M. L. De Escobar, M. C. De Andrade, T. J. Wong, E. Y. Cho, M. B. Maple, *Phys. Rev. B - Condens. Matter Mater. Phys.* **2015**, *91*, 144511.

[103] T. Ikeda, S. Iwanaga, H. Wu, N. J. Marolf, S. Chen, G. J. Snyder, *J. Mater. Chem.* **2012**, *22*, 24335.

[104] Y. G. Yan, J. Martin, W. Wong-Ng, M. Green, X. F. Tang, *Rev. Sci. Instrum.* **2013**, *84*, 115110.

[105] M. Otani, K. Itaka, W. Wong-Ng, P. K. Schenck, H. Koinuma, *Appl. Surf. Sci.* **2007**, *254*, 765.

[106] P. Ziolkowski, M. Wambach, A. Ludwig, E. Mueller, *ACS Comb. Sci.* **2018**, *20*, 1.

[107] J. García-Cañadas, N. J. E. Adkins, S. McCain, B. Hauptstein, A. Brew, D. J. Jarvis, G. Min, *ACS Comb. Sci.* **2016**, *18*, 314.

[108] K. Xiao, R. Lin, Q. Han, Y. Hou, Z. Qin, H. T. Nguyen, J. Wen, M. Wei, V. Yeddu, M. I. Saidaminov, Y. Gao, X. Luo, Y. Wang, H. Gao, C. Zhang, J. Xu, J. Zhu, E. H. Sargent, H. Tan, *Nat. Energy.* **2020**, *5*, 870.

[109] G. Prashun, S. Vladan, S. T. Eric, *Nat. Rev. Mater.***2017**, *2*, 1.

[110] Y.-M. You, W.-Q. Liao, D. Zhao, H.-Y. Ye, Y. Zhang, Q. Zhou, X. Niu, J. Wang, P.-F. Li, D.-W. Fu, Z. Wang, S. Gao, K. Yang, J.-M. Liu, J. Li, Y. Yan, R.-G. Xiong, *Science.* **2017**, *357*, 306.

[111] X. Liu, L. Dai, *Nat. Rev. Mater.* **2016**, *1*, 1.

[112] Y. Yuan, K. Amine, J. Lu, R. Shahbazian-Yassar, *Nat. Commun.* **2017**, *8*, 1.

[113] B. Keimer, S. A. Kivelson, M. R. Norman, S. Uchida, J. Zaanen, *Nat.* **2015**, *518*, 179.

[114] N. A. Spaldin, R. Ramesh, *Nat. Mater.* **2019**, *18*, 203.

[115] S. Ekins, A. C. Puhl, K. M. Zorn, T. R. Lane, D. P. Russo, J. J. Klein, A. J. Hickey, A. M. Clark, *Nat. Mater.* **2019**, *18*, 435.

[116] X. Luo, R. J. Xie, *J. Rare Earths* **2020**, *38*, 464.

[117] A. F. de Almeida, R. Moreira, T. Rodrigues, *Nat. Rev. Chem.* **2019**, *3*, 589.

[118] G. B. KAUFFMAN, I. MAYO, *Chem. Educ.* **1997**, *2*, 1.

[119] M. Cui, C. Yang, B. Li, Q. Dong, M. Wu, S. Hwang, H. Xie, X. Wang, G. Wang, L. Hu, M. Cui, C. Yang, Q. Dong, M. Wu, H. Xie, X. Wang, L. Hu, B. Li, G. Wang, S. Hwang, *Adv. Energy Mater.* **2021**, *11*, 2002887.

[120] K. Higgins, S. M. Valleti, M. Ziatdinov, S. V. Kalinin, M. Ahmadi, *ACS Energy Lett.* **2020**, *5*, 3426.

[121] J. G. Manion, A. H. Proppe, G. E. J. Hicks, E. H. Sargent, D. S. Seferos, *ACS Appl. Mater. Interfaces* **2020**, *12*, 26026.

[122] W. Yang, W. Wang, Y. Wang, R. Sun, J. Guo, H. Li, M. Shi, J. Guo, Y. Wu, T. Wang, G. Lu, C. J. Brabec, Y. Li, J. Min, *Joule* **2021**, *5*, 1209.

[123] J. Alstrup, M. Jørgensen, A. J. Medford, F. C. Krebs, *ACS Appl. Mater. Interfaces* **2010**, *2*, 2819.

[124] S. Sun, N. T. P. Hartono, Z. D. Ren, F. Oviedo, A. M. Buscemi, M. Layurova, D. X. Chen, T. Ogunfunmi, J. Thapa, S. Ramasamy, C. Settens, B. L. DeCost, A. G. Kusne, Z. Liu, S. I. P. Tian, I. M. Peters, J. P. Correa-Baena, T. Buonassisi, *Joule* **2019**, *3*, 1437.

[125] J. J. Yoo, G. Seo, M. R. Chua, T. G. Park, Y. Lu, F. Rotermund, Y. K. Kim, C. S. Moon, N. J. Jeon, J. P. Correa-Baena, V. Bulović, S. S. Shin, M. G. Bawendi, J. Seo, *Nat. 2021 5907847* **2021**, *590*, 587.

[126] X. Jiang, H. Li, Q. Zhou, Q. Wei, M. Wei, L. Jiang, Z. Wang, Z. Peng, F. Wang, Z. Zang, K. Xu, Y. Hou, S. Teale, W. Zhou, R. Si, X. Gao, E. H. Sargent, Z. Ning, *J. Am. Chem. Soc.* **2021**, *143*, 10970.

[127] J. Dagar, M. Fenske, A. Al-Ashouri, C. Schultz, B. Li, H. Köbler, R. Munir, G. Parmasivam, J. Li, I. Levine, A. Merdasa, L. Kegelmann, H. Näsström, J. A. Marquez, T. Unold, D. M. Többens, R. Schlatmann, B. Stegemann, A. Abate, S. Albrecht, E. Unger, *ACS Appl. Mater. Interfaces* **2021**, *13*, 13022.

[128] S. V. Kalinin, B. G. Sumpter, R. K. Archibald, *Nat. Mater.* **2015**, *14*, 973.

[129] K. Alberi, M. B. Nardelli, A. Zakutayev, L. Mitas, S. Curtarolo, A. Jain, M. Fornari, N. Marzari, I. Takeuchi, M. L. Green, M. Kanatzidis, M. F. Toney, S. Butenko, B. Meredig, S. Lany, U. Kattner, A. Davydov, E. S. Toberer, V. Stevanovic, A. Walsh, N. G. Park, A. Aspuru-Guzik, D. P. Tabor, J. Nelson, J. Murphy, A. Setlur, J. Gregoire, H. Li, R. Xiao, A. Ludwig, L. W. Martin, A. M. Rappe, S. H. Wei, J. Perkins, *J. Phys. D. Appl. Phys.* **2018**, *52*, 013001.

[130] D. Di Girolamo, J. Pascual, M. H. Aldamasy, Z. Iqbal, G. Li, E. Radicchi, M. Li, S.-H. Turren-Cruz, G. Nasti, A. Dallmann, F. De Angelis, A. Abate, *ACS Energy Lett.* **2021**, *6*, 959.

[131] F. Ren, L. Ward, T. Williams, K. J. Laws, C. Wolverton, J. Hattrick-Simpers, A. Mehta, *Sci. Adv.* **2018**, *4*, 1566.

[132] J. P. Correa-Baena, K. Hippalgaonkar, J. van Duren, S. Jaffer, V. R. Chandrasekhar, V. Stevanovic, C. Wadia, S. Guha, T. Buonassisi, *Joule* **2018**, *2*, 1410.

[133] K. A. Brown, S. Brittman, D. Jariwala, U. Celano, **2021**, *19*, 30.

[134] Y. Zhao, J. Zhang, Z. Xu, S. Sun, S. Langner, N. T. P. Hartono, T. Heumueller, Y. Hou, J. Elia, N. Li, G. J. Matt, X. Du, W. Meng, A. Osvet, K. Zhang, T. Stubhan, Y. Feng, J. Hauch, E. H. Sargent, T. Buonassisi, C. J. Brabec, *Nat. Commun.* **2021**, *12*, 2191.

[135] A. Ludwig, *npj Comput. Mater.* **2019**, *5*, 1.

[136] Z. Yang, W. Zhang, S. Wu, H. Zhu, Z. Liu, Z. Liu, Z. Jiang, R. Chen, J. Zhou, Q. Lu, Z. Xiao, L. Shi, H. Chen, L. K. Ono, S. Zhang, Y. Zhang, Y. Qi, L. Han, W. Chen, *Sci. Adv.* **2021**, *7*, 3749.

[137] K. J. Choi, J. Y. Lee, J. Park, Y. S. Seo, *Org. Electron.* **2015**, *26*, 66.

[138] C. Y. Lee, C. L. Chang, Y. N. Wang, L. M. Fu, *Int. J. Mol. Sci.* **2011**, *12*, 3263.

[139] Z. Xiao, L. Zhao, N. L. Tran, Y. L. Lin, S. H. Silver, R. A. Kerner, N. Yao, A. Kahn, G. D. Scholes, B. P. Rand, *Nano Lett.* **2017**, *17*, 6863.

[140] S. Kundu, T. L. Kelly, *EcoMat* **2020**, *2*, e12025.

[141] P. S. Mathew, J. T. DuBose, J. Cho, P. V. Kamat, *ACS Energy Lett.* **2021**, *6*, 2499.

[142] M. C. Brennan, A. Ruth, P. V. Kamat, M. Kuno, *Trends Chem.* **2020**, *2*, 282.

[143] J. H. Noh, S. H. Im, J. H. Heo, T. N. Mandal, S. Il Seok, *Nano Lett.* **2013**, *13*, 1764.

[144] S. K. Sharma, C. Phadnis, T. K. Das, A. Kumar, B. Kavaipatti, A. Chowdhury, A. Yella, *Chem. Mater.* **2019**, *31*, 3111.

[145] Z. Ahmad, A. Mishra, *J. Mater. Sci. Mater. Electron.* **2020**, *31*, 4672.

[146] A. M. A. Leguy, Y. Hu, M. Campoy-Quiles, M. I. Alonso, O. J. Weber, P. Azarhoosh, M. Van Schilfgaarde, M. T. Weller, T. Bein, J. Nelson, P. Docampo, P. R. F. Barnes, *Chem. Mater.* **2015**,

27, 3397.

[147] R. Ruess, F. Benfer, F. Böcher, M. Stumpp, D. Schlettwein, *ChemPhysChem* **2016**, *17*, 1505.

[148] A. M. A. Leguy, Y. Hu, M. Campoy-Quiles, M. I. Alonso, O. J. Weber, P. Azarhoosh, M. Van Schilfgaarde, M. T. Weller, T. Bein, J. Nelson, P. Docampo, P. R. F. Barnes, *Chem. Mater.* **2015**, *27*, 3397.

[149] A. Harillo-Baños, Q. Fan, S. Riera-Galindo, E. Wang, O. Inganäs, M. Campoy-Quiles, *ChemSusChem* **2022**, *15*, 202101888.

[150] S. Moradi, S. Kundu, M. I. Saidaminov, *ACS Mater. Au* **2022**, 5, 516.

[151] Y. Zhao, T. Heumueller, J. Zhang, J. Luo, O. Kasian, S. Langner, C. Kupfer, B. Liu, Y. Zhong, J. Elia, A. Osvet, J. Wu, C. Liu, Z. Wan, C. Jia, N. Li, J. Hauch, C. J. Brabec, *Nat. Energy* **2021**, *7*, 144.

[152] Y. An, C. A. R. Perini, J. Hidalgo, A.-F. Castro-Méndez, J. N. Vagott, R. Li, W. A. Saidi, S. Wang, X. Li, J.-P. Correa-Baena, *Energy Environ. Sci.* **2021**, *14*, 6638.

[153] D. Ulkoski, M. J. Munson, M. E. Jacobson, C. R. Palmer, C. S. Carson, A. Sabirsh, J. T. Wilson, V. R. Krishnamurthy, *ACS Appl. Bio Mater.* **2021**, *4*, 1640.

[154] Y. Zhao, J. Zhang, Z. Xu, S. Sun, S. Langner, N. T. P. Hartono, T. Heumueller, Y. Hou, J. Elia, N. Li, G. J. Matt, X. Du, W. Meng, A. Osvet, K. Zhang, T. Stubhan, Y. Feng, J. Hauch, E. H. Sargent, T. Buonassisi, C. J. Brabec, *Nat. Commun.* **2021**, *12*, 1.

[155] S. Jiang, J. Song, Y. Zhang, M. Nie, J. Kim, A. L. Marcano, K. Kadlec, W. A. Mills, X. Yan, H. Liu, R. Tong, H. Wang, I. F. Kimbrough, H. Sontheimer, W. Zhou, X. Jia, *ACS Appl. Mater. Interfaces* **2021**, *13*, 9156.

[156] Z. Wang, B. Xie, Q. Fang, F. Liu, J. Li, L. Tan, Z. Huang, L. Zhao, L. Jiang, *MRS Commun.* **2021**, *11*, 411.

[157] A. Nandy, C. Duan, M. G. Taylor, F. Liu, A. H. Steeves, H. J. Kulik, *Chem. Rev.* **2021**, *121*, 9927.

[158] T. Bo, Y. Wang, Y. Liang, X. Liu, J. Ren, H. Weng, M. Liu, S. Meng, *J. Phys. Chem. Lett.* **2021**, *12*, 6667.

[159] J. L. Hitt, Y. C. Li, S. Tao, Z. Yan, Y. Gao, S. J. L. Billinge, T. E. Mallouk, *Nat. Commun.* **2021**, *12*, 1114.

[160] G. L. W. Hart, T. Mueller, C. Toher, S. Curtarolo, *Nat. Rev. Mater.* **2021**, *6*, 730.

[161] Y. Sheng, T. Deng, P. Qiu, X. Shi, J. Xi, Y. Han, J. Yang, *Chem. Mater.* **2021**, *33*, 6918.

[162] A. J. Gormley, M. A. Webb, *Nat. Rev. Mater.* **2021**, *6*, 642.

[163] Q. Wang, L. Velasco, B. Breitung, V. Presser, *Adv. Energy Mater.* **2021**, 2102355.

[164] S. Langner, F. Häse, J. D. Perea, T. Stubhan, J. Hauch, L. M. Roch, T. Heumueller, A. Aspuru-Guzik, C. J. Brabec, *Adv. Mater.* **2020**, *32*, 1907801.

[165] A. Harillo-Baños, X. Rodríguez-Martínez, M. Campoy-Quiles, *Adv. Energy Mater.* **2020**, *10*, 1902417.

[166] B. P. MacLeod, F. G. L. Parlane, T. D. Morrissey, F. Häse, L. M. Roch, K. E. Dettelbach, R. Moreira, L. P. E. Yunker, M. B. Rooney, J. R. Deeth, V. Lai, G. J. Ng, H. Situ, R. H. Zhang, M. S. Elliott, T. H. Haley, D. J. Dvorak, A. Aspuru-Guzik, J. E. Hein, C. P. Berlinguette, *Sci. Adv.* **2020**, *6*, 8867.

[167] S. Sun, N. T. P. Hartono, Z. D. Ren, F. Oviedo, A. M. Buscemi, M. Layurova, D. X. Chen, T. Ogunfunmi, J. Thapa, S. Ramasamy, C. Settens, B. L. DeCost, A. G. Kusne, Z. Liu, S. I. P. Tian, I. M. Peters, J.-P. Correa-Baena, T. Buonassisi, *Joule* **2019**, *3*, 1437.

[168] A. Ludwig, *npj Comput. Mater.* **2019**, *5*, 70.

[169] S. Langner, F. Häse, J. D. Perea, T. Stubhan, J. Hauch, L. M. Roch, T. Heumueller, A. Aspuru-Guzik, C. J. Brabec, *Adv. Mater.* **2020**, *32*, 1907801.

[170] J. Burschka, N. Pellet, S.-J. Moon, R. Humphry-Baker, P. Gao, M. K. Nazeeruddin, M. Grätzel, *Nature* **2013**, *499*, 316.

[171] M. M. Lee, J. Teuscher, T. Miyasaka, T. N. Murakami, H. J. Snaith, *Science.* **2012**, *338*, 643.

[172] H.-S. Kim, C.-R. Lee, J.-H. Im, K.-B. Lee, T. Moehl, A. Marchioro, S.-J. Moon, R. Humphry-Baker, J.-H. Yum, J. E. Moser, M. Grätzel, N.-G. Park, *Sci. Rep.* **2012**, *2*, 591.

[173] J.-H. Im, C.-R. Lee, J.-W. Lee, S.-W. Park, N.-G. Park, *Nanoscale* **2011**, *3*, 4088.

[174] A. Kojima, K. Teshima, Y. Shirai, T. Miyasaka, *J. Am. Chem. Soc.* **2009**, *131*, 6050.

[175] A. Sandström, H. F. Dam, F. C. Krebs, L. Edman, *Nat. Commun.* **2012**, *3*, 1002.

[176] N. J. Jeon, J. H. Noh, W. S. Yang, Y. C. Kim, S. Ryu, J. Seo, S. Il Seok, *Nat.* **2015**, *517*, 476.

[177] M. I. Saidaminov, A. L. Abdelhady, B. Murali, E. Alarousu, V. M. Burlakov, W. Peng, I. Dursun, L. Wang, Y. He, G. Maculan, A. Goriely, T. Wu, O. F. Mohammed, O. M. Bakr, *Nat. Commun.* **2015**, *6*, 7586.

[178] M. Awais, D. Thrithamarassery Gangadharan, F. Tan, M. I. Saidaminov, *Chem. Mater.* **2022**, 34, 8112

[179] S. S. Mali, J. V. Patil, J. A. Steele, S. R. Rondiya, N. Y. Dzade, C. K. Hong, *ACS Energy Lett.* **2021**, *6*, 778.

[180] K. Xiao, R. Lin, Q. Han, Y. Hou, Z. Qin, H. T. Nguyen, J. Wen, M. Wei, V. Yeddu, M. I. Saidaminov, Y. Gao, X. Luo, Y. Wang, H. Gao, C. Zhang, J. Xu, J. Zhu, E. H. Sargent, H. Tan, *Nat. Energy* **2020**, *5*, 870.

[181] K. Higgins, S. M. Valleti, M. Ziatdinov, S. V. Kalinin, M. Ahmadi, *ACS Energy Lett.* **2020**, *5*, 3426.

[182] W. Yang, W. Wang, Y. Wang, R. Sun, J. Guo, H. Li, M. Shi, J. Guo, Y. Wu, T. Wang, G. Lu, C. J. Brabec, Y. Li, J. Min, *Joule* **2021**, *5*, 1209.

[183] J. Dagar, M. Fenske, A. Al-Ashouri, C. Schultz, B. Li, H. Köbler, R. Munir, G. Parmasivam, J. Li, I. Levine, A. Merdasa, L. Kegelmann, H. Näsström, J. A. Marquez, T. Unold, D. M. Többens, R. Schlatmann, B. Stegemann, A. Abate, S. Albrecht, E. Unger, *ACS Appl. Mater. Interfaces* **2021**, *13*, 13022.

[184] J. G. Manion, A. H. Proppe, G. E. J. Hicks, E. H. Sargent, D. S. Seferos, *ACS Appl. Mater. Interfaces* **2020**, *12*, 26026.

[185] K. Suchan, J. Just, P. Beblo, C. Rehermann, A. Merdasa, R. Mainz, I. G. Scheblykin, E. Unger, *Adv. Funct. Mater.* **2022**, 2206047.

[186] M. H. Futscher, J. M. Lee, T. Wang, A. Fakharuddin, L. Schmidt-Mende, B. Ehrler, *Quantification of Ion Migration in CH 3 NH 3 PbI 3 Perovskite Solar Cells by Transient Capacitance Measurements*, **2018**, 6, 1497

[187] M. T. SEBASTIAN, in *Dielectr. Mater. Wirel. Commun.*, Elsevier, **2008**, 161–203.

[188] E. Ugur, M. Ledinský, T. G. Allen, J. Holovský, A. Vlk, S. De Wolf, *J. Phys. Chem. Lett.* **2022**, *13*, 7702.

[189] J. Sanchez-Diaz, J. Torres, J. de la Torre, D. Esparza, J. M. Rivas, *Bull. Mater. Sci.* **2021**, *44*, 83.

[190] B. Lee, T. Hwang, S. Lee, B. Shin, B. Park, *Sci. Rep.* **2019**, *9*, 4803.

[191] H. T. Pham, Y. Yin, G. Andersson, K. J. Weber, T. Duong, J. Wong-Leung, *Nano Energy* **2021**, *87*, 106226.

[192] C.-H. Chiang, C.-G. Wu, *ChemSusChem* **2016**, *9*, 2666.